UNIVERSITÀ DEGLI STUDI DI TRIESTE

XXXIII CICLO DEL DOTTORATO DI RICERCA IN

SCIENZE DELLA TERRA, FLUIDODINAMICA E MATEMATICA. INTERAZIONI E METODICHE

Internal waves and turbulent mixing in closed stratified basins

Settore scientifico-disciplinare: ICAR/01

DOTTORANDA
Sara Marković

COORDINATORE
Prof. Stefano Maset

SUPERVISORE DI TESI
Prof. Vincenzo Armenio

ANNO ACCADEMICO 2019/2020

Contents

Abstract

We present results of numerical simulations of a stratified reservoir with a three-layer stratification, subject to an oscillating surface shear stress. The simulations are carried out at a laboratory scale, using Large eddy simulation. We solve the three dimensional Navier-Stokes equations under the Boussinesq approximation using a second-order accurate finite volume solver. The model was validated by reproducing experimental results for the reservoir response to surface shear stress and resonant frequencies of internal waves.

In the first part of our research, we investigate the effect of sloped end-walls on mixing and internal wave adjustment to forcing within the basin, for three different periods of forcing. We find interesting combinations of wave modes and mixing under variation of the forcing frequencies and of the inclination of the end-walls. When the frequency of the forcing is close to the fundamental mode wave frequency, a resonant internal seiche occurs and the response is characterized by the first vertical mode. For forcing periods twice and three times the fundamental period the dominant response is in terms of the second vertical mode. Adjustment to forcing via second vertical mode is accompanied by the cancellation of the fundamental wave and energy transfer towards the high-frequency waves. The study shows that the slope of the end-walls dramatically affects the location of mixing, which has feedback on the wave field promoting higher vertical modes.

The second part of our research is devoted to the investigation of the influence of Earth's rotation on the wave field. In this case, the ratio of forcing to inertial period plays the important role in discerning whether Kelvin or Poincare type waves will be excited which has direct consequences on the wave modal structure and the turbulent quantities. Superinertial forcing frequency excites Poincare waves that are observed to increase the amount of turbulent dissipation rate in the system. In the two cases, where the forcing period was half and twice the fundamental one, we observed that superinertial forcing frequency pushed the dominant internal wave response from first to second vertical mode. The study shows that the increase of the importance of the rotation rate over forcing increases the turbulent dissipation rate in the interior while decreasing it in the near-surface and near-boundary regions.

	Parameter	**Symbol (unit)**
Geometry	Domain height	H (m)
	Pycnocline length	L (m)
	Upper layer thickness	h_1 (m)
	Lower layer thickness	h_2 (m)
	Transitional layer thickness	Δh (m)
	End-wall angle	α ($^\circ$)
Forcing	Kinematic surface shear stress	τ (m^2/s^2)
	Surface friction velocity	u_* (m/s)
	Oscillatory period	T_w (s)
Environment	Upper layer density	ρ_1 (kg/m^3)
	Lower layer density	ρ_2 (kg/m^3)
	Density difference	$\Delta\rho = \rho_2 - \rho_1$ (kg/m^3)
	Reference density	$\rho_0 = 0.5(\rho_1 + \rho_2)$ (kg/m^3)
	Reduced gravity	$g' = g\Delta\rho/\rho_0$ (m/s^2)
	Buoyancy frequency	N (s^{-1})
	Vertical shear	S (s^{-1})
Internal waves	Linear long-wave speed	$c_0 = \sqrt{g' h_1 h_2 / H}$ (m/s)
	Fundamental wave period	$T_1 = 2L/c_0$ (s)
	Maximum interface displacement	η_0 (m)
	Nonlinear coefficient	$\alpha_{NL} = 3/2 c_0 (h_2 - h_1)/(h_1 h_2)$
	Steepening time scale	$T_s = L/(\alpha\eta_0)$ (s)
Fluid properties	Kinematic viscosity	ν (m^2/s)
	Diffusivity of scalar	κ (m^2/s)
Turbulence properties	Dissipation rate	ϵ (m^2/s^3)
	Turbulent diffusivity of density	K_ρ (m^2/s)
Nondimensional	Wedderburn number	$W = \frac{g' h_1^2}{u_*^2 L}$
	Forcing to fundamental period ratio	$r_T = T_w/T_1$
	Turbulence intensity parameter	$Re_b = \epsilon/(\nu N^2)$
	Richardson number	$Ri = N^2/S^2$
Rotational properties	Angular velocity	Ω (rad/s)
	Coriolis parameter	f(rad/s)
	Inertial period	$T_i = 2\pi/f$ (s)
	Rossby radius	$R = c_0/f$ (m)
	Burger number	$S = R/(0.5L)$

Table 1: Dimensional and nondimensional parameters.

Chapter 1

Introduction

A lake is a large volume of water that is surrounded by land and not connected to the ocean except by rivers or streams. When undisturbed, water in a lake is calm or slow-moving.

During the year, the waterbody goes through different stages of stratification. In autumn, as air temperatures drops, the surface water cools, becomes denser and sinks to the bottom. This continues until the whole waterbody has the temperature of maximum density ($4°C$), after that, cooling of surface water does not lead to sinking, instead, it stays on the top of the dense layer. As air cools further, winter stratification forms as surface water cools and eventually forms the ice on top of the $4°C$ water. In spring, warming of the surface water and wind action cause surface water to sink and mix with the deep water in a process called spring turnover. As warming of the lake surface continues, the temperature difference between surface and deep water increases. During the summer season, stable stratification develops that can be approximated with a three-layer model: An upper, well-mixed layer (epilimnion) with warm water; a transitional middle layer (metalimnion) with a high temperature gradient; a bottom layer (hypolimnion) with cold and low-momentum water, isolated from the more energetic upper layer by the stable stratification in the metalimnion. The surface with the highest temperature gradient inside the metalimnion identifies the thermocline.

Lakes are home to various life forms. The primary producers are life forms that take the energy from the sun or chemical processes, and they are crucial to the survival of micro and macro consumers that feed on other life forms. The near-shore area of the lake (also called a littoral zone) is home to phytoplankton, aquatic vascular plants and films of attached algae, while in the offshore area (pelagic zone) only phytoplankton. The margin between the littoral and pelagic zone is the point where the amount of solar irradiance that reaches the bottom of the lake falls under 1%, where plants and algae cannot grow due to darkness. (Lewis, 2009, Likens, 2010).

During summer stratification, hypolimnion water is isolated from the oxygen and nutrient exchange with the upper layers. Such stratification can lead to consumption of all available oxygen by organisms in the hypolimnion, which can have serious consequences due to the build-up of reduced substances and toxic compounds such as hydrogen sulfide (Vincent, 2009).

For these reasons, it is important to understand the processes that take place in the summer stratified lakes. This is a difficult task given due to the complex dynamics that take place in such systems. Main energy exchange occurs at the lake surface in form of heat, as warming and cooling, and momentum, due to the action of the wind on the lake surface. During the summer stratification, the effects of surface warming and cooling are mostly confined in the well-mixed epilimnion. The effects of wind are

substantially more complex. A part of the stress applied by the wind on the water surface is transferred to the surface boundary layer, while part energizes surface waves (Wüest and Lorke, 2003). The strongly stratified system suppresses the turbulence, thus the input of momentum leads to the excitation of internal waves. These waves transfer energy to the small scales by the interaction of internal waves with the lake bottom, as well as by wave breaking at the sloped walls.

The excitation of the internal waves occurs through the process called wind-setup, both processes are addressed in more details in sections 1.1 and 1.2, while the interaction of the waves with the sloping walls is addressed in section 1.3. The effects of the wave field on the internal waves are discussed in 1.4. In section 1.5 we define our focus and discuss the state of the art.

1.1 Wind setup

When the thicknesses of the epilimnion and hypolimnion are much larger than that of the metalimnion, the system can be approximated as composed of two layers with different densities which meet at the thermocline. In a closed basin, the main hydrodynamic forcing is wind stress. The response of a two-layer system to the wind shear stress is controlled by the Wedderburn number W (Thompson and Imberger, 1980, Imberger and Hamblin, 1982) that is defined as the ratio between the baroclinic restoring force and the wind driving force:

$$W = \frac{g' h_1^2}{u_*^2 L} \tag{1.1}$$

where $g' = g\Delta\rho/\rho_0$ is the reduced gravity based on the density difference across the thermocline, h_1 is the thickness of the upper layer, L is the length of the lake and $u_*^2 = \tau$ is the square of the friction velocity resulting from the kinematic wind shear stress over the water surface τ.

The action of the wind shear stress leads to the displacement of the thermocline. For steady wind, an analytical solution for the steady displacement is obtained, given by the balance between the baroclinic gravitational pressure force due to the tilted thermocline and the force due to the wind stress (Boegman, 2009). When this solution is put into W, $W^{-1} \approx \eta_0/h_1$ where η_0 is the steady-state vertical displacement of the thermocline at the end-walls. This solution allows the simplified interpretation of W^{-1} as a portion of h_1 that is occupied by the displacement of the thermocline at the upwind end-wall.

1.2 Internal waves

When the wind quits blowing and the surface stress condition is relaxed, a wave field forms and degenerates in time. As initially observed by Mortimer (1953) for various lakes, the internal wave field is dominated by basin-scale linear waves or internal seiches. The internal seiche is the solution of the linear wave equation (Gill, 1982):

$$\frac{\partial^2 \eta}{\partial t^2} = c_0^2 \frac{\partial^\eta}{\partial x^2} \tag{1.2}$$

where $\eta(x,t)$ is the interface displacement, $c_0 = \sqrt{\frac{g' h_1 h_2}{H}}$ is the linear long-wave speed, h_2 is the bottom layer depth and H is the reservoir depth. For the initial condition with inclined interface, this linear

equation also allows the development of higher odd modes of linear waves with the sinusoidal solutions and period of the internal seiches:

$$T_i^{(n)} = \frac{2L}{nc_0} \tag{1.3}$$

where n denotes the horizontal mode.

If the amplitude of the internal seiches is large enough, nonlinear effects become significant, causing the occurrence of nonlinear even horizontal modes. Steepening of the nonlinearities is associated with a steepening timescale $T_s = L/(\alpha_{NL}\eta_0)$ where η_0 is the maximum displacement of an interface and $\alpha_{NL} = 3/2c_0(h_2 - h_1)/(h_1 h_2)$ is a nonlinear coefficient and leads to dispersion and generation of high-frequency solitary-like waves. Horn et al. (2001) and Boegman et al. (2005b) carried out throughout theoretical and experimental analysis of the degeneration of the internal wave field.

The first five horizontal modes are shown in figure 1.1. It is clear that the center of the basin is a nodal location for odd modes and antinodal for even modes. We will use these features in our work to discern among the different horizontal modes.

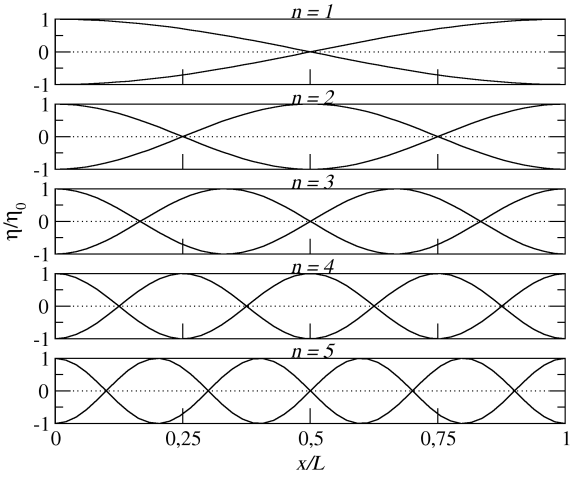

Figure 1.1: Sketch of the first five horizontal modes of seiche waves.

In lakes where the thicknesses of metalimnion and epilimnion are comparable, which is often the case for the small and mid-sized lakes we are interested in, the two-layer approximation is no longer valid and a response in terms of high-order vertical modes is possible. For example, the second vertical mode can be described as a variation of the thickness of the metalimnion, where the upper and lower edge of the metalimnion do not oscillate in phase.

The second vertical mode was mathematically described by using a three-layer stratification (see among others Csanady (1982), Monismith (1985), Münnich et al. (1992)), and more accurately using the continuous stratification model to calculate both the second (Münnich et al., 1992) and the higher-order vertical modes (LaZerte, 1980) by solving ordinary differential equation:

$$\frac{\partial^2 w}{\partial z^2} = -\lambda^2 N^2 w \tag{1.4}$$

where w is vertical velocity component, $N^2 = -g/\rho_0 \partial\rho/\partial z$ is buoyancy frequency squared, and λ^2 is the eigenvalue. The expected velocity profiles for the first four vertical modes calculated with the procedure of Early et al. (2020) are shown in figure 1.2. Observations show that the occurrence of these modes strongly depends on the thickness of metalimnion (Roget et al., 1997, Vidal et al., 2007, MacIntyre et al., 2009), duration of forcing (Wiegand and Chamberlain, 1987, Münnich et al., 1992, Vidal et al., 2007, Valerio et al., 2012) and bathymetry (Münnich, 1996).

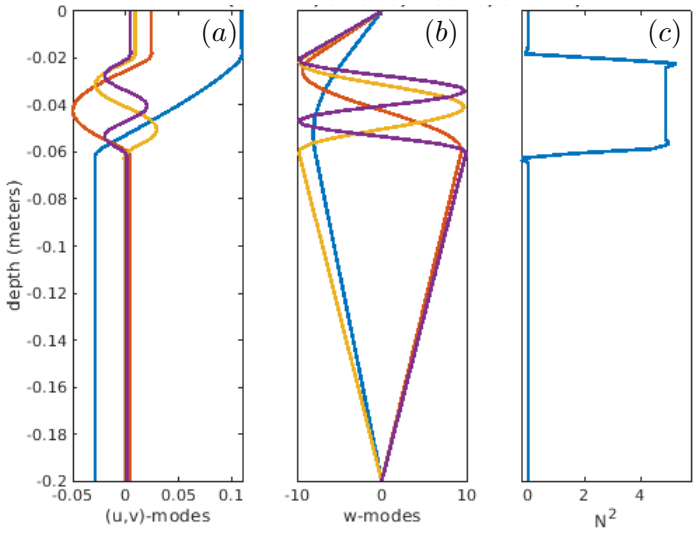

Figure 1.2: Panels (a, b) contain vertical profiles of velocity components for the first four vertical modes: (a) horizontal u, v and (b) vertical w velocity component. Panel (c) shows the corresponding vertical profile of the buoyancy frequency squared N^2. The profiles are calculated for a stratification that matches the initial condition in our simulations (a piecewise linear density profile) with the procedure of Early et al. (2020). Color code in (a, b) refers to vertical modal structure as: ■ first mode; ■ second mode; ■ third mode; ■ fourth mode.

There are many studies regarding internal waves, most of them used simplified models in terms of the idealized basin (i.e. Monismith (1987)), two-layer models for stratification (i.e. Horn et al. (1986)), constant mean density profile (density field is decomposed as $\rho(x, z, t) \rightarrow \overline{\rho}(z) + \rho'(x, z, t)$) (i.e. Fricker and Nepf (2000)).

Most situations are characterized by wind stress oscillating according to a diurnal cycle, typically due to atmospheric circulations such as anabatic/katabatic winds and lake breeze. Oscillatory forcing was experimentally investigated by Boegman and Ivey (2007, 2012) with an oscillating tank and Rozas et al. (2014) by applying a moving belt, both using an experimental setup with a two-layer stratification, therefore allowing only for the development of the first vertical mode. Boegman and Ivey (2007, 2012) found that the response to the forcing is controlled by the ratio between the forcing period T_w and the fundamental oscillatory period which we denote as $T_1 = T_i^{(1)}$, calculated according to (1.3). We will denote this ratio as $r_T = T_w/T_1$. For $r_T < 0.5$ internal seiches with higher mode occur, for $0.5 < r_T < 1.5$ a resonant fundamental internal seiche V1H1 develops, and for $r_T > 1.5$ a non-resonant forced V1H1 internal seiche is present where V1H1 denotes a combination of first vertical mode and first horizontal mode.

1.3 Mixing at sloped walls

In general cases, the end-walls (beaches) of a lake are not vertical. Mixing in the near-shore region can originate from the interaction of boundaries and seiching currents or the breaking of high-frequency waves. Sato et al. (2014) found that overall diffusivity is an order of magnitude higher than the one measured in the interior and argued that the difference arises from mixing at the basin walls.

Internal seiches induce upslope/downslope flow along the inclined walls and cause a periodic occur-

rence of convective mixing. During an upwelling event, currents transport heavier deep water over lighter surface water, causing an unstable stratification and consequent mixing. This process is described by Lorke et al. (2005) as shear-induced convection.

Breaking of the high-frequency (solitary-like) wa ves on the slopes has been extensively investigated via laboratory experiments (Helfrich, 1992, Michallet and Ivey, 1999, Boegman et al., 2005a, Boegman and Ivey, 2009) and numerical simulations (Vlasenko and Hutter, 2002, Arthur and Fringer, 2014, 2016, Aghsaee et al., 2010). In the experiments of Michallet and Ivey (1999) it was found that mixing efficiency is low for small and large slopes; consistent with these findings are the results of Boegman et al. (2005a) who analyzed mixing efficiency with respect to Iribarren number, that is the ratio of the beach slope to the wave slope, and found that mixing efficiency is highest for intermediate values of this parameter, that correspond to medium slopes. Wave breaking at the sloped walls can be described by the rotor model (Thorpe, 1998); breaking leads to diapycnal mixing, mainly in the lower layer, producing water of intermediate density that forms an intrusion and flows along isopycnals toward the body of the lake (Wain et al., 2013).

Boundary mixing induced by the high-frequency internal waves was observed by Lorke (2007), while Goudsmit et al. (2002), MacIntyre et al. (2009) and Wain and Rehmann (2010) found boundary mixing caused by low-frequency waves - seiches.

1.4 The effect of Earth's rotation

When the size of the lake is comparable with the Rossby radius, $R = c_0/f$, where $f = 2\Omega \sin\theta$ is the Coriolis parameter, Ω is angular velocity and θ is latitude, rotation of the Earth affects the large-scale waves and allows the development of Kelvin and Poincaré waves Csanady (1967). To determine whether rotational effects are important for the internal wave field, the Burger number is defined as $S = R/l$ (Pedlosky et al., 1987), the ratio of Rossby radius and l is the characteristic length scale, that is typically taken to be half-length of the basin. For $S \to 0$ rotational effects are important and for $S \to \infty$ rotational effects are negligible. There is no abrupt transition point where rotation becomes important but the rotational effects are generally taken into account for $S \leq 2$.

The rotational gravity waves are solutions of the linear inviscid equations of motion for homogeneous system. The momentum and mass conservation equations are:

$$\frac{\partial u}{\partial t} - fv = -g\frac{\partial \eta}{\partial x} \tag{1.5}$$

$$\frac{\partial v}{\partial t} + fu = -g\frac{\partial \eta}{\partial y} \tag{1.6}$$

$$\frac{\partial \eta}{\partial t} + \frac{\partial}{\partial x}(H_e u) + \frac{\partial}{\partial y}(H_e v) = 0 \tag{1.7}$$

where u, v are x, y (horizontal) velocity components respectively and $H_e = \Delta\rho/\rho_0 \; h_1 h_2/H$ is the equivalent depth (using the water depth H instead corresponds to the surface/barotropic problem). The solution for the sinusoidal waves in an unbounded domain gives Poincaré waves. These waves have a particular energy partition (Gill, 1982) described as:

$$\frac{PE}{KE} = \frac{\omega^2 - f^2}{\omega^2 + f^2} \tag{1.8}$$

where PE and KE are potential and kinetic energy and $\omega = 2\pi/T$ is the angular wave frequency and T is the wave period. In bounded domains, energy partition depends on the domain shape. Antenucci and Imberger (2001) analytically found this partition for circular and elliptical basins, as a function of Burger number S. Poincaré waves usually have anticyclonic rotation and their angular frequency ω is superinertial ($\omega > f$). This is general result, where in Northern hemisphere anticyclonic rotation is clockwise, while cyclonic is counterclockwise.

With the introduction of boundaries into the system, the analytical solution allows the formation of Kelvin waves, which propagate parallel to the boundaries. The amplitude of these waves has a maximum at the boundary and an exponential decrease $\exp(-y/R)$, where y is the distance from the boundary and R is Rossby radius (Gill, 1982). For lakes with $L >> R$ these waves are confined in the coastal region, while for the lakes $L < R$ they are present throughout the interior. They have cyclonic rotation and angular frequency $\omega < f$. Based on linear inviscid theory, Kelvin waves are limited to $S \leq 1/\sqrt{2}$ (Lamb, 1932, Stocker and Imberger, 2003, Wake et al., 2004).

Given that development of the described waves strongly depends on the basin shape, analytical and semi-analytical solutions are found only for a small number of idealized shapes such as rectangular (Rao, 1966, 1977), circular (Csanady, 1967) and elliptical Antenucci and Imberger (2001) basins. There are numerous observations of these waves in lakes (i.e. Schwab (1977), Antenucci et al. (2000), Antenucci and Imberger (2003), Gómez-Giraldo et al. (2006), Choi et al. (2012), Valipour et al. (2015)) as well as numerical investigations for the wave field (i.e. Rao et al. (1976), Stocker and Imberger (2003), de la Fuente et al. (2008), Ulloa et al. (2015)) and laboratory investigations (i.e. Wake et al. (2004, 2005), Rozas et al. (2014), Ulloa et al. (2014), Rojas et al. (2018)).

With respect to energy transfer to the higher frequency waves, rotation induces a specific behavior. According to de la Fuente et al. (2008) and de la Fuente et al. (2010), fundamental (basin-scale) Kelvin waves transfers most of their energy to their superharmonics in form of higher horizontal modes, and steepen producing solitary-like waves; while higher modes of fundamental Poincaré wave periodically transfer their energy back to the parent wave instead of degenerating into solitary-like waves; further, nonlinear triad interactions between Kelvin and Poincaré waves can excite new basin-scale waves.

The rotational effects promote the formation of solitary-like waves by increasing their number (Ulloa et al., 2014), while at the same time inhibit the existence of a permanent solitary-like solution. While the scale of the single solitary-like wave is too small to be affected by the rotational effects, groups of solitary waves are sensitive to them. Helfrich (2007) showed that under the influence of rotation, solitary waves initially transfer energy to the longer inertia-gravity waves, which steepen and form a secondary solitary-like wave. According to Grimshaw et al. (1998), the rotational effects either decrease the amount of solitary waves or prevent their formation. Gerkema and Zimmerman (1995) found a critical ratio (f/ω) above which rotation balances nonlinearity and prevents the wave degeneration by the solitary-like waves.

1.5 State of the art

We are interested in turbulent mixing and internal wave dynamics induced by the periodic wind action in a stratified basin, archetypal of lakes or reservoirs. The response of a water basin to the wind action on its surface largely depends on its stratification.

The wave response to periodic forcing of a stratified basin was investigated experimentally and theoretically by La Rocca et al. (2005), Wake et al. (2007), Boegman and Ivey (2007, 2012), Rozas et al. (2014).

More recently, the influence of periodic forcing on a lake was investigated by Ulloa et al. (2019, 2020) who employed Large Eddy Simulation (LES) to study the hydrodynamics of a full scale lake. In Ulloa et al. (2019) a case study investigation was conducted for the summer conditions in Lake Alpnach. A periodic diurnal forcing yielded a near-resonant V2H1 wave response, along with other nonresonant vertical modes. Besides the wave analysis, they investigated turbulence and mixing and identified episodic mixing at the sloped walls as a significant factor in overall mixing. In Ulloa et al. (2020) different resonant wave responses (quasilinear V1H1, V2H1 and nonlinear V2H1) to periodic forcing were obtained by variation of the level of stratification in a three-layer stratified basin with sloping walls. The main focus of their investigation was the analysis of the transport processes under the fully developed resonant wave regimes. Similarly, we use LES to analyze the wave responses of a basin to periodic wind stress, mainly focusing on the influence of variations of forcing and bathymetry at a laboratory scale. The laboratory scale setup requires less computational time and allows us to conduct larger number of simulations, which gives us a better understanding on how variation of different parameters influences the basin response to periodic forcing. The idea behind variation of the forcing period while fundamental period is constant is to describe the differences in response to diurnal forcing of basins with different size (different fundamental period). The rectangular domain, that we initially use, allows us the direct comparison with analytical solution and experimental data that typically consider the idealized, rectangular, domains. The variation of the sloping end-walls gives information on the importance of bathymetry and how it has feedback on the basin response to forcing. The general setup of our simulations is similar to that of Ulloa et al. (2020) in that we apply periodic stress on the three layers stratified domain with sloped walls; however the focus of our research is substantially different, since we inspect the initial development of the wave response. This is an important issue, since in real systems often the breeze regime is not such to allow a steady arrangement of the internal wave system, which, rather, often moves through successive transitional states. We provide new insights into the development of the initial wave response, describing both wave field and transitions from one dominant wave response to another. We also note how variations of different parameters influences this transient development.

A thorough investigation of the periodically forced internal waves in the rotational two-layer stratified system was conducted by Rozas et al. (2014). In their research, they analyzed field data, simulated the behavior of a two-layer system and conducted experiments with periodic forcing of the stratified rectangular tank by using a moving belt. They found that resonant fundamental Kelvin waves radiate most of their energy (90%) to other wave modes and that non-linear interactions are important for the characterization of such wave fields. In particular, non-linear interactions among Kelvin and Poincaré waves lead to the excitation of new modes. Such triad interactions and coupling among internal Kelvin and Poincaré waves were also described by de la Fuente et al. (2008), Ulloa et al. (2014). Rozas et al. (2014) experimentally confirmed the behavior predicted by theory where the wave response of the system is strongly controlled by the forcing frequency. We further extend the research of internal waves in rotating basins by setting a three layer stratification, thus allowing the development of the waves with higher vertical modes. We inspect how variation of forcing period and rate of rotation influences the internal wave response and turbulence.

Thesis overview: The goal of this thesis is to extend the knowledge of how lake-like three-layer stratified systems adapt to periodic forcing under different conditions. Particularly, we use stratification that allows the formation of the higher vertical modes and we investigate the transient development of the wave response and changes in the wave field such as the transition from the first to the second vertical

mode wave response. We inspect the mixing mechanisms in such systems and the feedback they have on internal waves.

In chapter 2 we consider variations of forcing period with respect to the fundamental period and variations of the angles of the sloping walls in a nonrotating frame of reference. Our findings show that in cases when the period of forcing is far from the fundamental one, the shape of the domain plays an important role in modifying the wave response through mixing and changing the background density field.

In chapter 3 we consider wave responses to periodic forcing in a rotating frame of reference and we consider variations of forcing period and rotation rate (expressed through Burger number). Our findings show that in this case additional parameter, which is the ratio of forcing and inertial period, dictates the excitation of the specific waves types (Kelvin and Poincaré waves) which have direct consequences on the amount of turbulence and mixing in such systems.

Chapter 2

Stratified basin response to the periodic forcing

In this chapter, we are interested in lakes that are not affected by the Earth's rotation. The Coriolis force is negligible for mid-latitude small and mid-sized lakes (up to ≈ 5 km). For a typical geometry and stratification profile of this class of lakes, only large ones (≈ 5 km) may have a the fundamental period that matches the diurnal forcing period ($r_T = 1$); smaller lakes generally have a fundamental period that is several times smaller than a day. That is why we will focus on $r_T \geq 1$.

The chapter is organized in the following way. In section 2.1 we describe the numerical model which is validated in the Section 2.2, by reproducing experiments relevant for the purposes of our research. Section 2.3 contains results of regridding tests for the case study. In section 2.4 the response of the system with vertical end-walls is considered. In section 2.5 we analyze the influence of the variations of the angles of the end-walls. In section 2.6 we give concluding remarks.

The part of the research described in this chapter is contained in a paper under revision Marković and Armenio (2021).

2.1 Mathematical model

The flow we investigate in the present paper is characterized by the co-existence of internal waves and turbulence. We will see that mechanical turbulence is generated in the near-surface layer, in the corner flow (at the intersection of forced surface and end-walls) due to downward jet and processes that take place at the sloped walls. Also, wave breaking at the slope walls produces turbulence which propagates to the interior; reproduction of these mechanisms needs eddy resolving simulations, either Direct Numerical Simulation (DNS) or Large Eddy Simulation (LES). The former would need a resolution of the near-wall and free-surface thin viscous layer, the latter requiring a huge and unjustified resolution in a flow region not central for the scopes of the present research. For this reason, our strategy was to use a LES in conjunction with a wall-layer modelization of the wind stress at the free surface, which accurately reproduces the mechanism of generation of mechanical turbulence at the free surface. On the other hand, since the flow may stand in a transitional regime, due to the above-mentioned interaction between turbulence and internal waves and to the periodic forcing, we use a dynamic Lagrangian model, which is well known in the literature to be able to reproduce accurately flows characterized by transitional and intermittent turbulence. Specifically, the model automatically switches off in regions of relaminarization

and switches on in presence of turbulence, to reproduce significant subgrid scale (SGS) events, whenever they occur. We solve the set of filtered three-dimensional Navier-Stokes equations under the Boussinesq approximation for the density field:

$$\frac{\partial \overline{u}_j}{\partial x_j} = 0 \tag{2.1}$$

$$\frac{\partial \overline{u}_i}{\partial t} + \frac{\partial}{\partial x_j}(\overline{u}_i \overline{u}_j) = -\frac{\partial \overline{p}}{\partial x_i} + g_i \frac{\rho}{\rho_0} + \frac{\partial}{\partial x_j}\left[\nu_{eff}\left(\frac{\partial \overline{u}_i}{\partial x_j} + \frac{\partial \overline{u}_j}{\partial x_i}\right)\right] \tag{2.2}$$

$$\frac{\partial \overline{\rho}}{\partial t} + \frac{\partial}{\partial x_j}(\overline{\rho u}_j) = \frac{\partial}{\partial x_k}\left(\kappa_{eff}\frac{\partial \overline{\rho}}{\partial x_k}\right) \tag{2.3}$$

In eqs. (2.1),(2.2),(2.3), the overbar denotes a filtering operation, u_i is the velocity component along the x_i direction (hereafter we use x_1, x_2, x_3 and x, y, z respectively for along wind, transverse and vertical upward directions), p is pressure divided by the bulk density ρ_0, $\mathbf{g} \equiv (0, 0, -g)$ is the gravity acceleration vector, $\nu_{eff} = \nu + \nu_{SGS}$ is the sum of the kinematic viscosity ν and the SGS turbulent viscosity ν_{SGS}, ρ is the fluid density, and $\kappa_{eff} = \nu/Pr + \nu_{SGS}/Pr_{SGS}$ is the sum of molecular and SGS thermal diffusivity, Pr and Pr_{SGS} being the molecular and SGS Prandtl number, respectively.

The subgrid scale tensor which comes out from filtering the Navier-Stokes equations, $\tau_{ij} = \overline{u_i u_j} - \overline{u}_i \overline{u}_j$, is here parametrized using the eddy viscosity assumption:

$$\tau_{ij} - \frac{\delta_{ij}}{3}\tau_{kk} = -2\nu_{SGS}\overline{S}_{ij} \tag{2.4}$$

where $\overline{S}_{ij} = \frac{1}{2}(\frac{\partial \overline{u}_i}{\partial x_j} + \frac{\partial \overline{u}_j}{\partial x_i})$ is the filtered strain rate tensor. The SGS viscosity is related to the strain rate tensor (Smagorinsky, 1963) as:

$$\nu_{SGS} = c_S^2 \Delta^2 |\overline{S}_{ij}| \tag{2.5}$$

where $\Delta = (\Delta_x \Delta_y \Delta_z)^{1/3}$ is the filter width computed using the local cell width and c_S^2 is the Smagorinsky constant for SGS momentum fluxes. Here the constant is determined dynamically using the Lagrangian dynamic SGS model of Meneveau et al. (1996) as implemented by Cintolesi et al. (2015). For SGS thermal diffusivity, we use the Reynolds analogy $\kappa_{SGS} = \nu_{SGS}/Pr_{SGS}$, with $Pr_{SGS} = 1$. The Schmidt number is set to $Sc = \nu/\kappa = 500$ as discussed in Lienhard and Atta (1990), Liu (1995) while $\nu = 10^{-6}\mathrm{m}^2/\mathrm{s}$.

As initial condition, we consider a fluid at rest with a piecewise linear density stratification:

$$\rho(\vec{x}, t=0) = \begin{cases} \rho_1 & \text{if } z \geq h_{m1} \\ \frac{\rho_2 - \rho_1}{h_{m2} - h_{m1}}(h_{m2} - z) + \rho_2 & \text{if } h_{m2} < z < h_{m1} \\ \rho_2 & \text{if } z \leq h_{m2} \end{cases} \tag{2.6}$$

where ρ_1, ρ_2 are densities of the upper and lower layer and $h_{m1} = h_2 - 0.5\Delta h$, $h_{m2} = h_2 + 0.5\Delta h$ are the heights of the edges of the middle layer. The positions and thicknesses of layers are sketched in figure 2.1.

Since large movement of the free surface are not expected in the cases under investigation (Boegman, 2009) the free surface is approximated as a rigid lid and the periodic wind stress with period T_w is represented through sinusoidal kinematic shear stress implemented as:

$$\tau = (\nu + \nu_w)\frac{\partial u}{\partial z} = u_*^2 \sin(\frac{2\pi t}{T_w}),\ \frac{\partial v}{\partial z} = 0,\ w = 0 \tag{2.7}$$

where ν_w is calculated with wall function that generates near-wall profile of ν_w based on modeled kinetic energy (Robertson et al., 2015, Liu, 2016).

We use $u \equiv u_1, v \equiv u_2, w \equiv u_3$. Horizontal stress components are energized with the addition of random fluctuations with zero average. In x and y directions, fluctuations were 20% and 1% respectively of the mean value of τ. We use no slip conditions along the solid walls.

The boundary condition for the density field is zero gradient for surface, bottom, and end-walls (no-flux conditions). We consider a two-dimensional problem, meaning that the problem is, in a Reynolds averaging sense, two-dimensional. Hence, we use a three-dimensional domain with periodic conditions along the cross-stream x_2 or y direction. This is appropriate because we investigate the development of the two-dimensional internal wave response. In this sense, the periodic conditions can be considered as removal of the influences of the side walls on the internal wave field.

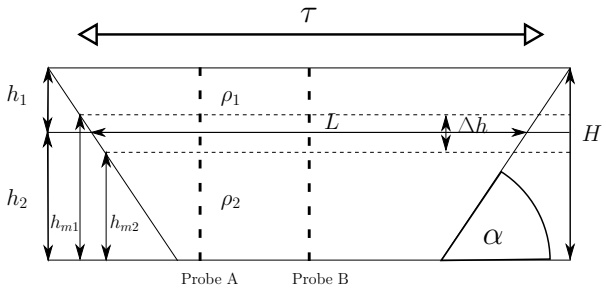

Figure 2.1: Sketch of the simulation setup with the main parameters and locations of the probes.

The Courant number is defined as $Co = c_0 \Delta t / \Delta x$ with c_0 the internal wave speed, Δt the time step and Δx the cell length. To resolve properly the wave field, $C_0 \sim 0.2$ is obtained using $\Delta t = 0.01$s. For larger time steps (i.e. $\Delta t = 0.02$) non-physical high-frequency waves develop at the interface.

The Navier-Stokes equations are integrated in time using the PISO algorithm (Issa et al., 1986). For the time scheme we used the Crank-Nicolson scheme (Crank and Nicolson, 1947), for spatial derivatives we use central differences, and for the divergence operator we use the Van Leer scheme (Van Leer, 1974). The system of equations is solved using the solver `buoyantBoussinesqPimpleFoam` implemented in the OpenFOAM library (Jasak, 1996, Weller et al., 1998, Chen et al., 2014). The solver has been extensively validated in a number of cases, including variable density flows (see among the others Cintolesi et al. (2015)).

In order to calculate turbulent statistics we will decompose the filtered field in a Reynolds-averaging sense as $\overline{\theta}(t) = \langle\theta\rangle + \theta''(t)$, where θ represents a generic field quantity, $\langle\theta\rangle$ represent the mean value and $\theta''(t)$ represents the resolved part of the fluctuating field. Note that the total fluctuating field is the sum of resolved fluctuations plus subgrid-scale ones $\theta'(t) = \theta''(t) + \theta_{SGS}$. The quantity ($\theta_{SGS}$) is unknown in a deterministic sense, but one can write, specifically for the turbulence dissipation rate $\epsilon = \epsilon_{RES} + \epsilon_{SGS}$. The resolved part comes from post-processing the LES resolved field, the SGS part comes from the subgrid scale model. In the rest of the paper we omit the overbar for the filtered quantities. We anticipate that, since the grid resolution of our numerical experiments is large, in our simulations most of the turbulent spectrum is resolved directly during the simulation and the residual SGS stresses are low. We find that after the initialization of the wave response, the ratio $\nu_{SGS}/\nu \sim 2$ at the intersection of the stratified middle layer and end-walls, which is typical of 'quasi-DNS', according to the definition of Spalart (1997).

2.2 Reproduction of experiments

In order to test the ability of our numerical model to properly predict the behavior of the stratified basin forced by surface shear stress, we reproduce two significant laboratory experiments, one by Monismith (1986), the other by Boegman et al. (2005b): we use the former to test the ability of the model to reproduce response to the surface shear stress; the latter is used to test the performance of the model to reproduce the internal wave field. In the tests we use no-slip conditions at the solid walls of the tank, to mimic experimental conditions. The sizes of the domains correspond to the tank size used in each experiment.

2.2.1 Response to surface shear stress

Monismith (1986) performed experiments by applying a moving belt at the bottom of a rectangular tank filled with stratified water. When the belt starts running, it drags a thin layer of fluid which carries momentum in the core of the flow. As it approaches the end-walls of the tank, a narrow jet of fluid hits the wall and turns vertically, causing mixing at the interface. This is an undesired effect of the experimental setup since it does not have a counterpart in the real scale situation. To suppress the vigorous flow that appears at the intersection of the running belt and end-wall of the tank, a sponge was installed next to the end-wall in the experimental setup (for details see the original paper Monismith (1986)). Stratification was set using salt to obtain density variations. The belt was moved with constant velocity for a predetermined amount of time. In the experiments, the Author used salt concentration as a stratifying agent, and density has a roughly linear distribution over a finite thickness Δh.

The experimental setup herein reproduced is summarized in Table 2.1. Here, we discuss the simulation relative to experiment 8 of Monismith (1986). As a boundary condition for the moving belt, we use constant kinematic stress $\tau = u_*^2$. Numerical simulations were set up using $(n_x \times n_y \times n_z) = (525 \times 30 \times 60)$ grid points, where grid resolution expressed in wall units as $\Delta x_i^+ = \Delta x_i u_* / \nu$ is $(\Delta x^+, \Delta y^+, \Delta z^+) = (59.6, 89.4, 30)$.

Exp.	h_2(m)	H(m)	B(m)	g'(m/s^2)	U_B(m/s)	u_*^2(m^2/s^2)	Ri	L/h_2	W	T_0(s)	T_1(s)
8	0.1	0.2	0.3	0.11	0.203	8e-5	138	35	3.9	874	94.39

Table 2.1: Setup of experiment 8 for two-layer stratification of Monismith (1986). h_2 is the thickness of the lower (near belt) layer, U_B is the belt velocity, T_0 is the duration of the belt running and T_1 is period of the fundamental internal seiche mode.

The sidewall diffuse layer is set according to Farrow and Stevens (2003), by adding a linear drag term $\lambda \mathbf{u}$ to the momentum equation, where $\lambda \neq 0$ only near the downwind wall. The magnitude of λ is increased linearly from zero at the beginning of the end flow region $x = x_\lambda$ to $\lambda_{max} = 2.9$ s^{-1} at the end-wall $x = L$.

$$\lambda(x) = \begin{cases} 0, & 0 < x < x_\lambda \\ \lambda_{max}(x - x_\lambda)/(L - x_\lambda), & x_\lambda < x < L \end{cases} \tag{2.8}$$

Modulation function $f(x)$ is:

$$f(x) = \begin{cases} 1, & x < x_\lambda \\ (x - L)/(x_\lambda - L), & x_\lambda < x \leq L \end{cases} \tag{2.9}$$

The kinematic stress is a piecewise linear function of x to avoid undesirable corner flows. In the diffuse layer, it linearly goes from u_*^2 to 0 at the end-walls.

Numerical simulation reproduced well the characteristics of the flow, specifically the initial barotropic flow as well as the development of the jet-like flow at the interface for $t > 0.25T_1$. Differently from the physical diffuser used in the experiment, the numerical one causes the attenuation of the jet-like flow that forms at the interface. In the experiments this flow was observed to plunge and to be incorporated into the mixed layer within 20 to 30 cm from the wall (see Monismith (1986) for details); in the numerical simulation, this flow plunges faster and the jet-like behavior disappears after only a few centimeters. The main effect of concentrated return flow was to sharpen the interface at the downwind end and to diffuse it at the upwind end (Monismith, 1986); these effects are weaker in our simulation, which is illustrated in figure 2.2. Figure 2.3$(a-h)$ shows good agreement among contours of the density field, with the difference in sharpening and diffusing near the end-walls that can be directly related to the attenuation of the return jet-like flow.

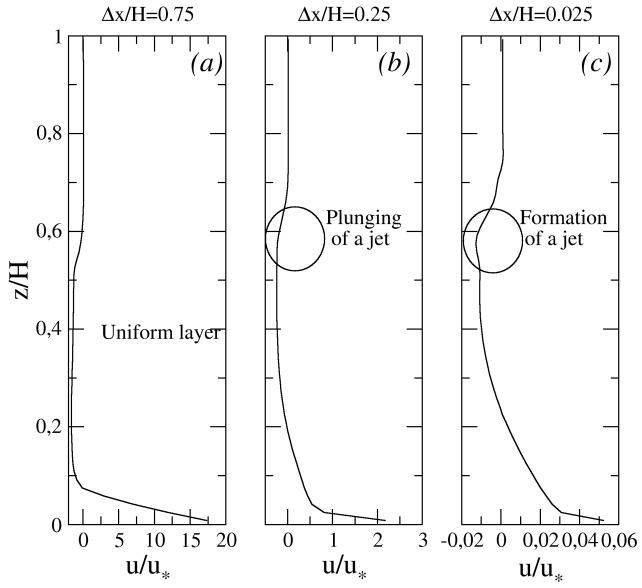

Figure 2.2: Vertical profile of non-dimensional streamwise velocity at different distances from the end-wall Δx. From the left to the right increasing distance from the end-wall. Compare panel (c) with figure 5(b) of Monismith (1986).

Attenuation of a jet-like flow in the diffuse layer also has an impact on mixed layer density, which is defined as the average density of fluid that is located no more than 1 cm from the belt (Monismith, 1986). A horizontal density gradient in a mixed layer occurs as a response to the application of the stress. Due to a smaller amount of diffusion at the upwind end, it took more time for interface spreading to reach the bottom and create a horizontal density gradient along with it. Variation of the magnitude of λ or the shape of the diffuse layer influences the flow development substantially. Decreasing λ under the value herein used resulted in partial mixing of the interface due to the corner jet flow.

The net effect of applied stress consists in a net change of the density profile that is indicative of time-averaged vertical buoyancy flux. In figure 2.3(i, k) we can see that the numerical profiles of vertical density are very similar to the experimental ones. The main difference can be observed in 2.3(j, l) as somewhat less net change in density at the interface and more in the bottom layer, which can be a consequence of attenuation of a jet-like flow.

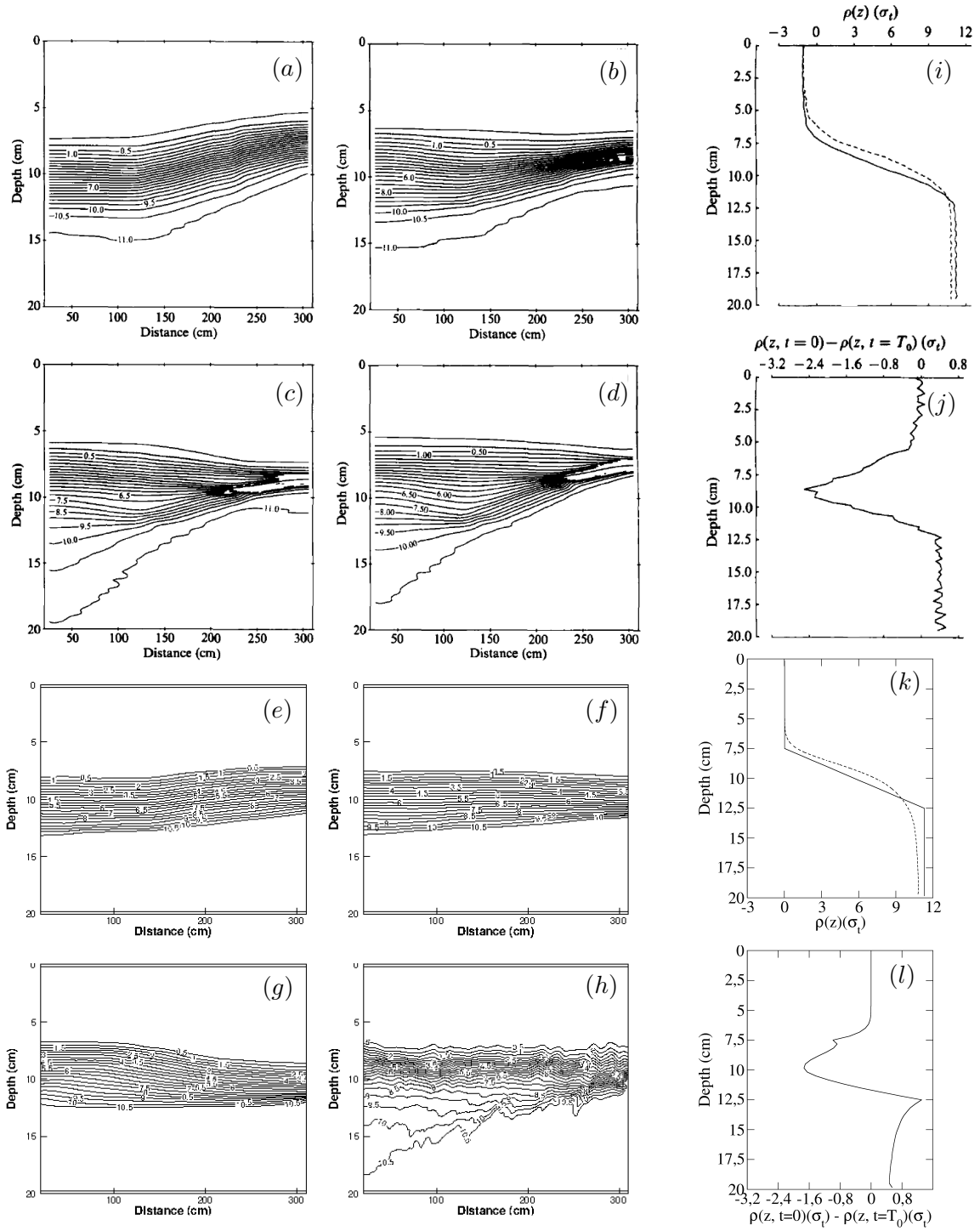

Figure 2.3: Figures $(a-h)$ show distribution of isopycnals at times: (a, e), $0.32T_1$; (b, f), $0.64T_1$; (c, g), $0.96T_1$; (d, h), $8T_1$. Superposition of initial (solid) and final (dashed) density profiles is shown in (i, k) and net density difference due to mixing in (j, l). Figures $(a-d)$ and (i, j) are from the Monismith (1986) and $(e-h)$ and (k, l) from our simulation. The density is expressed in units $\sigma_t = \rho - 1000$ kg/m^3. Quantities are dimensional for comparison purposes.

We can conclude that our model reproduces reasonably well the initial seiche response to the wind action, both in terms of inclined isopycnals, and in terms of the amount of mixing (indirectly estimated through the density profile). Differences may be mainly attributed to the intrinsic differences always

present between a laboratory experiment and a numerical one. Among the others, the already discussed corner flow issue, the small difference in the initial profile (nearly discontinuous transition versus smooth transition), differences in impulsively started motion in experiments and numerical simulation, or the fact that the belt used in the experiment might have generated vibrations which can alter the shear stress and produce vertical velocity fluctuations hardly reproducible in a numerical experiment.

2.2.2 Internal waves

Boegman et al. (2005b) conducted experiments in a rectangular tank filled with a two-layer stratified fluid, characterized by the presence of a thin interface layer with a thickness of about 1 to 2 cm (for details see the original paper). Internal waves were initiated by tilting the tank with respect to the horizontal plane (to create inclined pycnocline somewhat mimicking the wind-induced setup) and subsequent rapid release to the horizontal position (that may be interpreted as relaxation of the wind conditions). They performed different experiments in a rectangular tank with dimensions $(6\times0.3\times0.29)\mathrm{m}^3$, and we consider experiment 5 as reference for our simulation, summarized in Table 2.2. The computational grid is composed of $(n_x \times n_y \times n_z) = (600 \times 20 \times 58)$ grid points. The no-slip conditions are used on all walls of the tank.

Run	h_1/H	θ (°)	$W^{-1} = \eta_0/h_1$	T_s(s)	T_1(s)
5	0.30	0.28	0.15	434	109.78

Table 2.2: Settings of Boegman et al. (2005b) experiment herein used as reference. h_1/H is the ratio of upper layer height to total height, θ is the initial tilt angle and η_0 is the initial maximum interface displacement at the end-walls.

Our simulation differs from the experiment in that we start from an initial ideal condition that is a hydrostatic field in a horizontal tank with the interface inclined using the value of W^{-1} as in the experiment. As density profile, we use a two-layer distribution with a finite thickness of the interface resembling that of exp. 5 of Boegman et al. (2005b), with density decreasing linearly with height. The density field was sampled along the vertical lines matching the wave gauges B and C used in the experiments, therefore we refer to the sampling positions likewise. Line B is placed near the middle of the channel, a nodal position for linear basin-scale internal waves so that the wave signal comes from nonlinear internal waves. Spot C is placed approximately at 3/4 length of the channel, where the basin-scale linear-wave (first horizontal model H1 internal seiche) signal dominates.

The interface displacement time records obtained in the experiment and in the numerical simulation (not shown) are similar to each other, in spite of the intrinsic differences between the two setups. The comparisons between the two records are quite good, showing the presence of a fundamental mode and a decrease of the amplitude with time due to viscous effects. At wave gauge B, where the presence of non-linear waves can be detected, the analytical solution for interface displacement gives zero amplitude. The comparison between our numerical results and experimental ones appears satisfactory. As expected, non-linear wave amplitudes in both simulation and experiment increase as $t \to T_s$ and decrease afterward.

To quantify better the information contained in the time signals, we perform the spectral analysis (Discrete Fourier Transformation) of the interface displacement time series and compare the results with those of the experiments and of the analytical solution. Figure 2.4(a, b) shows the time spectra of the signals at wave gauge C. The most energetic resonant mode of internal seiche H1 corresponds to the analytical solution and has a similar shape as in experiments.

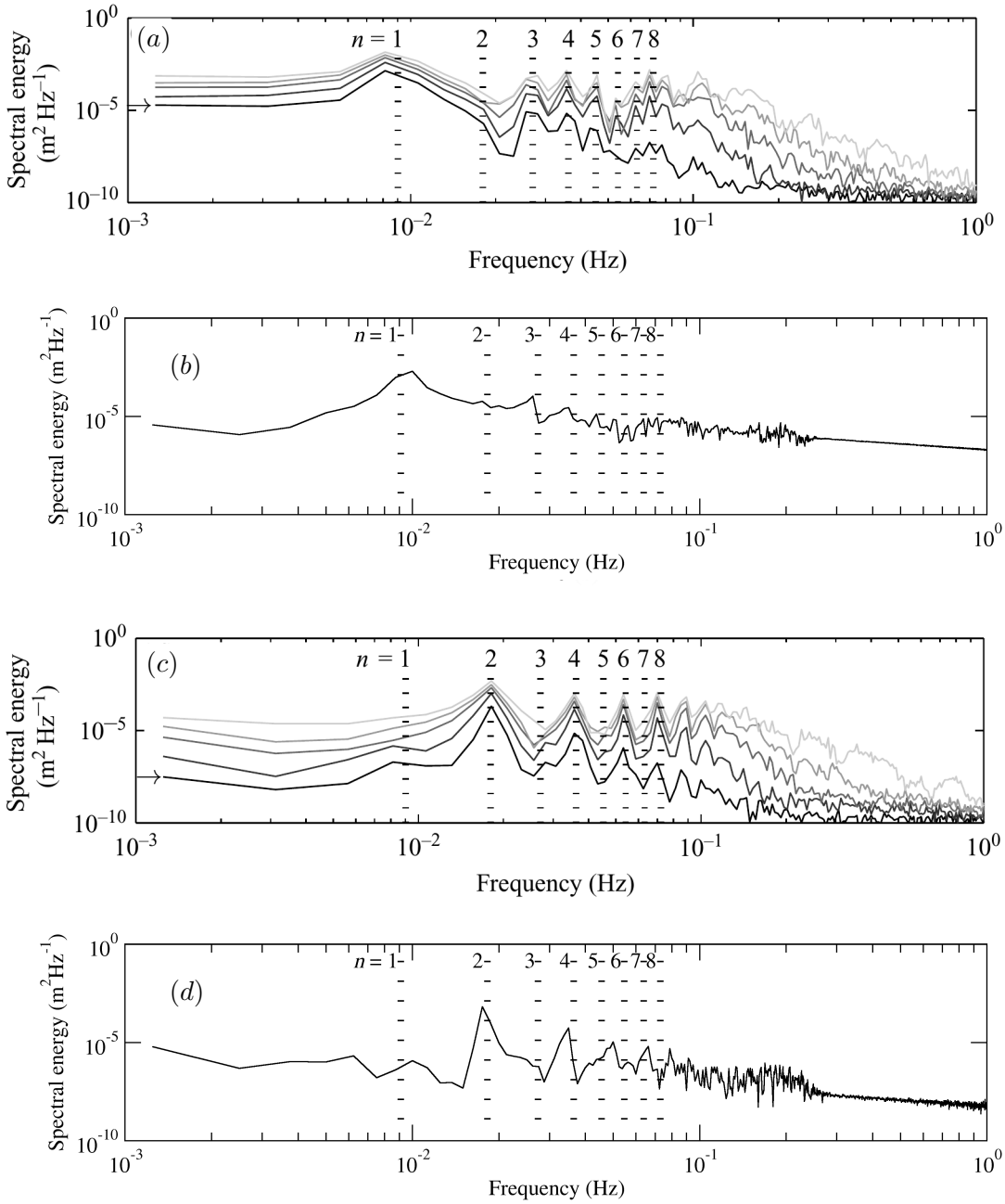

Figure 2.4: Spectra of interface displacement: (a, b) sampled at the wave gauge C; (c, d) sampled at the wave gauge B. Figures (a, c) are from the experiments of Boegman et al. (2005b) (lowest line marked with arrow represents exp. 5), while (b, d) are from numerical simulation. The dashes denote frequencies of the first 8 modes.

Higher modes are reproduced by our simulation, with a small shift in the frequency with respect to both experiments and analytical solutions. Although differences are expected between our simulation results and the analytical solution, differences with the experimental data are less intuitive. They may arise from the different setup (specifically initial condition) or even to some amount of artificial dissipation in the numerical model, although regridding tests (not shown) have proved that a numerically convergent solution has been obtained. We also note that frequency shifts in the spectra are sensitive to the changes

of the length of the time series, therefore they may be related to wave degeneration with time. For the spectra herein shown, we have chosen to use the same length series as the one used in the original paper, that is 800 s. The high-frequency modes are well present in our signal showing the capability of the numerical model to reproduce the higher frequency energy content.

Figure 2.4(c, d) show the spectral analysis at the wave gauge B, where non-linear effects are dominant. We point out that the initial conditions directly excite the linear (odd) modes only; the steepening of the linear modes due to nonlinear effects excites nonlinear (even) modes. Our simulation reproduced well these nonlinear effects and the consequent even modes. With respect to experimental results, we obtain similar energy distribution among even modes with the same shift in frequencies as previously observed.

Although there is a small shift in frequencies of higher modes between theory, experiment, and numerical simulation, our model seems to reproduce well both linear and nonlinear aspects of the wave field. Differences may likely arise from the different laboratory setup with respect to the numerical one. In particular, rapid rotation of the tank upon releasing of the initial conditions in physical experiments introduces Coriolis, Euler and centrifugal force, not present in our experiments. We can conclude that our numerical model reproduces the internal wave field in a satisfactory way.

To summarize, comparison with data from laboratory experiments shows that our numerical model appears suited for the laboratory-scale analysis of a stratified basin forced by wind stress.

$(n_x \times n_x \times n_z)$	n_{tot}	Δx^+	Δy^+	Δz^+
$(300 \times 25 \times 80)$	600,000	37.2	44.6	13.9
$(330 \times 28 \times 88)$	813,120	33.8	39.8	12.7
$(270 \times 22 \times 72)$	427,680	41.3	50.7	15.5
$(450 \times 25 \times 120)$	1,350,000	24.7	44.5	9.3

Table 2.3: Resolution of the grids used for testing.

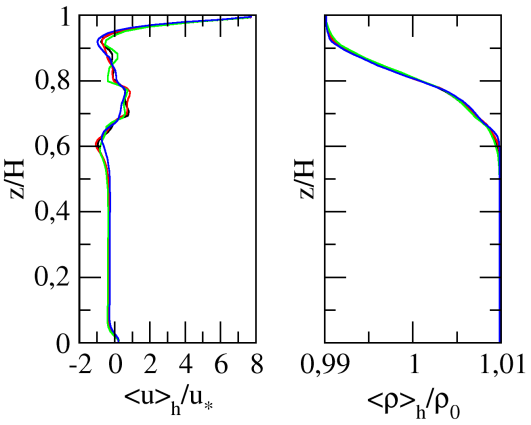

Figure 2.5: Vertical profiles of horizontally averaged and non-dimensionalized streamwise velocity component and density obtained using different grids. Color code: ■, basic grid; ■, 10% finer grid; ■, 10% coarser grid; ■, 50% finer grid.

2.3 Grid validation

For each simulation set we test different grids to verify accuracy of the results. In figure 2.5 we show horizontally averaged quantities obtained with four different grids for the case of oscillating surface shear stress ($r_T = 1$) with sloped walls $\alpha = 30°$ at the time $1.5T_w$.

We express the grid resolution in wall units ($\Delta x_i^+ = \Delta x_i u_* / \nu$). Table 2.3 reports the grid used in our tests with resolution expressed in wall units. The basic grid is the one used in our simulations $(n_x \times n_x \times n_z) = (300 \times 25 \times 80)$; we test sensitivity of results to grid resolution in terms of refinement and coarsening of 10% in each direction corresponding to grids $(n_x \times n_x \times n_z) = (330 \times 28 \times 88)$ and $(n_x \times n_x \times n_z) = (270 \times 22 \times 72)$, respectively; and larger grid variations with 50% finer grid in x and z directions $(n_x \times n_x \times n_z) = (450 \times 25 \times 120)$.

Based on the comparison of the vertical profiles we conclude that we have reached grid convergence, apart from the minor changes which do not contribute to the physics we are studying and that, on the other hand, would increase the computational cost also in view of the large number of simulations carried out in the paper.

2.4 Analysis of the rectangular basin response to the oscillating surface shear stress

We perform laboratory-scale numerical experiments of a stably stratified basin subject to periodic surface stress, mimicking the effect of a daily-cycle breeze over the surface of a stratified lake.

Here, we first discuss the case of vertical end-walls ($\alpha = 90°$) and discuss the response of the basin with respect to the oscillatory modes. The importance of using idealized basins, such as rectangular, stands in the fact that results of simulations can be compared to analytical solutions and experimental data, that typically consider the idealized rectangular domain. Besides, rectangular setup yields results that are easier to interpret, as they are free from complex processes that take place at the sloping walls.

The dimensions of the domain are, respectively, length $L = 2\,\mathrm{m}$, depth $H = 0.2\,\mathrm{m}$ and cross-stream extension of the computational domain $B = H$. Conditions of the simulation are summarized in Table 2.4. The density difference herein used is typical for laboratory-scale experiments while the vertical stratification profile, namely the thickness of the three layers, is typical for medium and small lakes; we will label them accordingly as epilimnion, hypolimnion, metalimnion. The density distribution herein used, characterized by the thickness of metalimnion comparable to those of the other layers, is well known to favor the development of internal waves with higher vertical modes. The steepening timescale T_s presented in the table is calculated as a reference value using the approximation $\eta_0 \approx h_1/W$. A sinusoidal kinematic shear stress applied to the surface is set in such a way to give ratios $r_T \approx 1, 2, 3$. Initial condition for density and boundary condition for stress are sketched on figure 2.1. Each simulation has the duration of $6T_w$.

h_1(cm)	h_2(cm)	Δh(cm)	ρ_1(kg/m^3)	ρ_2(kg/m^3)	u_*^2(m^2/s^2)	W	T_1(s)	T_s(s)	T_w(s)
4	16	4	1000	1020	3.11×10^{-5}	5	50.73	112.74	50,100,150

Table 2.4: Main parameters of the numerical experiment.

The computational grid is discretized as $(n_x \times n_y \times n_z) = (300 \times 25 \times 80)$, such that middle layer contains $(300 \times 25 \times 16)$ cells. The grid resolution as wall units per cell size is $(\Delta x^+, \Delta y^+, \Delta z^+) = (37.2, 44.6, 13.9)$.

For each case, we tracked the time series to conducted spectral analysis. The sampling resolution in time for the time series is $\Delta t = 0.01$s. At each time step, we sampled the density profile over the 80 vertical grid points and then interpolated the height for the values of density to be tracked. Time series of isopycnal heights are sampled at $0.25L$ (probe A) and $0.5L$ (probe B) (see figure 2.1). Probe B is on a nodal location for linear waves that form as odd horizontal modes, therefore it is informative of the presence of nonlinear waves.

We define the interface as $\rho_0 = 0.5(\rho_1 + \rho_2)$ and we compute spectral energy of interface height time series. For two isopycnals, respectively above and under the interface ($\rho_0 - 0.25\Delta\rho$ and $\rho_0 + 0.25\Delta\rho$), we compute cross power spectral density to indicate phase lag among them. The absence of phase lag

indicates that isopycnals maintain at the same distance in the vertical direction, which corresponds to the behavior of the first vertical mode, while the existence of the phase lag indicates the existence of higher vertical modes.

To examine the vertical modal structure of the dominant wave response, we show vertical profiles of velocity components and buoyancy frequency squared for each case. The displayed quantities are sampled during the last forcing period when the flow is fully developed. The quantities are averaged over 25 cells in the homogeneous spanwise direction and shown at the time instant, where time is denoted as a phase of the forcing period φ, where $\varphi = 0$ corresponds to the beginning of the 6th forcing period $t = 5T_w$

When a surface forcing is applied on the rectangular basin at the laboratory scales, the fast near-surface layer rapidly produces down-well as it reaches the end-wall and penetrates through the stratified region. This was observed in experimental setups of Monismith (1986), Stevens and Imberger (1996), who prevented this jet-like flow from destroying the stratification by using a sponge at the end-walls. To reduce the effects of the formation of the geometry-related return jet (see Appendix for details), we apply a stronger stratification and weaker amplitude of forcing, which results in a higher Wedderburn number (equation (1.1)). This parameter cyclically changes in time, with a minimum ($W = 5$) at the peak of forcing while it is higher during the rest of the forcing period. The Wedderburn number used in our numerical experiment is representative of situations in real-scale basins exposed to weak to moderate wind forcing. Based on Horn's diagram (Horn et al., 2001) and the parameters used for our setup $W^{-1} = 0.2$ and $h_1/H = 0.2$ we expect the degeneration of large-scale waves due to damped linear waves and solitary waves.

2.4.1 Forcing period $r_T = 1$

In the present case, the fundamental V1H1 seiche is directly forced and we obtain a resonant response. In the time series of interface height h_i (figure 2.6(a, b)) we observe at position A (non-nodal for linear waves), that a wave response with the fundamental period develops, which corresponds to the occurrence of a basin-scale linear wave. As forcing continues, the fundamental response is subject to resonant amplification, and we observe an increase in the wave amplitude. The formation of nonlinear modes is highlighted at position B, which is nodal for linear waves. There, a dominant wave response has a periodicity of half fundamental period which corresponds to the second horizontal mode. We observe that the growth of the amplitude of nonlinear waves is roughly ruled by the steepening time scale T_s; for $t > T_s$ the amplitude of nonlinear waves is nearly constant and solitary-like waves develop. These waves can be observed as pulse-like waves that degenerate the large-scale waves marked with a circle in figure 2.6(a). While we do not inspect the instantaneous fields for each high-frequency wave that appears in the time series, we note that the Richardson number Ri (shown in Section 4) is generally super-critical except in the near-surface layer, thus we can exclude the shear instabilities as an origin of these waves. The degeneration of the wave field by nonlinear solitary-like waves is well expected based on Horn's diagram, and they are the only high-frequency waves that we observe in instantaneous fields. The solitary-like waves propagate with almost permanent form, therefore they can be observed at all locations. Their decay in time is due to viscous and wall effects (Koop and Butler, 1981, Tang et al., 1990) or they deform and disintegrate (Grimshaw et al., 2010). Given that our time series contain many superimposed waves, we cannot directly observe these changes.

The presence of higher horizontal modes is also evident in the energy spectrum of the interface height time series (figure 2.6(c, d)). We denote forcing frequency f_w and its super harmonics $f_{wm} = mf_w$,

$m = 1, 2, ...$ The fundamental frequency of the basin-scale linear wave is f_1 and higher modes are calculated using eqn. (1.3) as $f_n = 1/T_i^{(n)}$. Most energy is confined in the first mode, although appreciable energy is transferred by non-linear interactions to the second horizontal mode. The excitation of higher horizontal modes up to mode 10 is observable in the spectra.

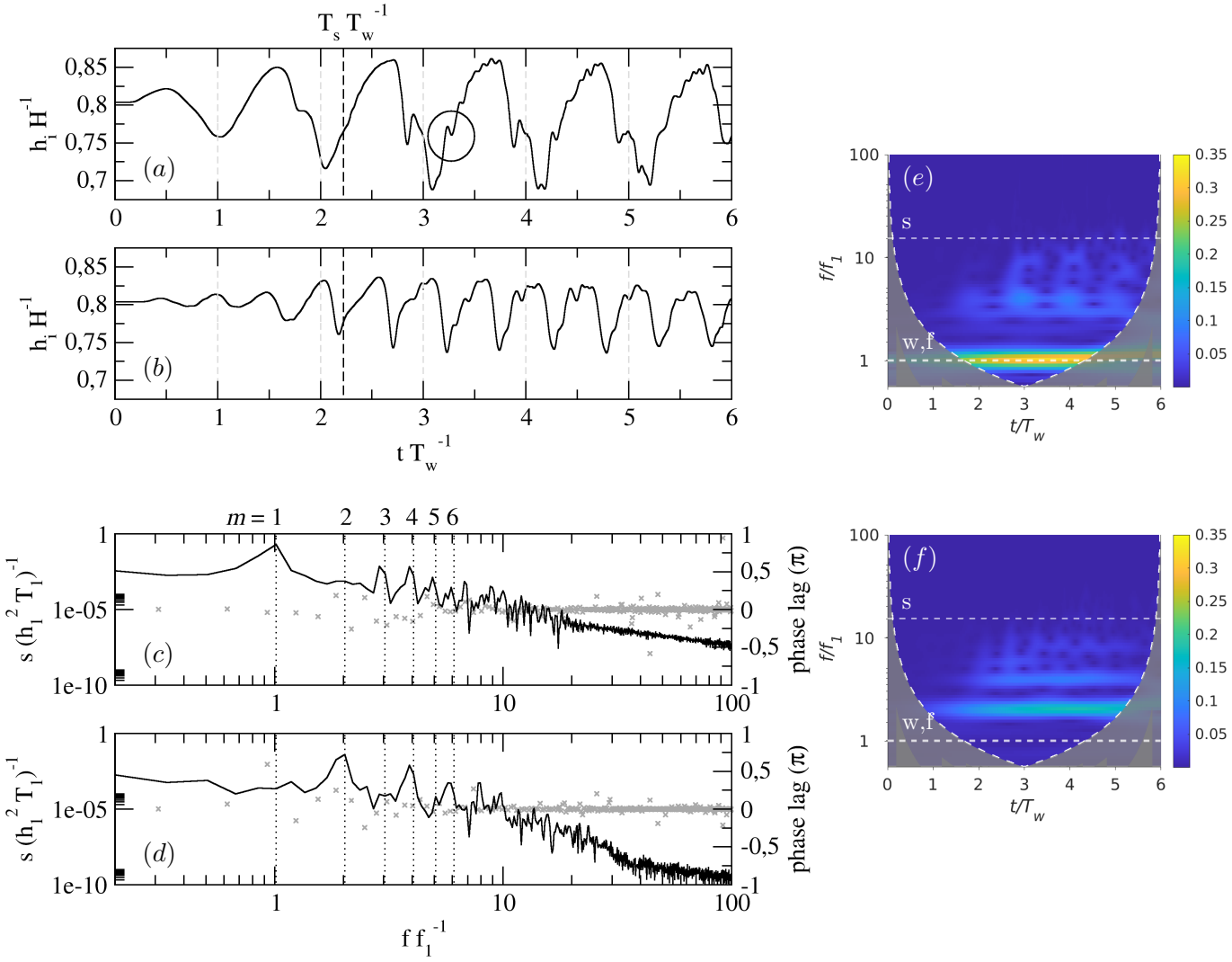

Figure 2.6: Panels (a, b) show the time series of non-dimensional interface height h_i/H for resonant forcing ($r_T = 1$) plotted versus the number of forcing period at probes A and B, respectively. The signature of the solitary waves is marked with a circle and the dashed gray vertical lines denote the nondimensional time period T_1/T_w and multiple values, while dashed black vertical line denotes the nondimensional steepening time-scale T_s/T_w. Panels (c, d) show nondimensional spectral energy of interface height (lines) and phase lag among isopycnals (x's) at probes A and B, respectively. Vertical dotted lines represent nondimensional forcing frequency and its m-th superharmonics. Theoretical frequencies of modes of internal seiche can be read as integers from x-axis given that $f_n = nf_1$. Panels (e, f) show wavelet spectra of interface height sampled at probes A and B, respectively, where colors represent absolute values of the CWT. Dashed white horizontal lines denoted with letters indicate: w, forcing frequency f_w; f, fundamental frequency f_1; s, approximate frequency of solitary-like waves $\approx f_s$.

To get information on the vertical structure of the modes identified by energy spikes, we calculate the phase lag (coherence phase interpreted as a phase lag) between the heights of the isopycnals $\rho_0 \pm 0.25\Delta\rho$. The phase lag is generally very small across all frequencies, indicating that isopycnals maintain vertical distance so that the system response corresponds to the first vertical mode. Significant phase lag is found only in the middle of the basin (position B) near the fundamental frequency, corresponding to the periodic spreading and contraction of isopycnals at this location.

To better understand the development of the wave field in time we use the wavelet analysis of the interface height time series (figure 2.6(e, f)) in terms of continuous wavelet transform (CWT). The cone of influence is plotted within the white dashed lines; it represents the border between the data with the accurate time-frequency representation and data in the shaded region where the accuracy of data is potentially influenced by edge effects. Initially, the fundamental mode is energized. After the first forcing cycle, the resonant response begins, which is characterized by the increase of energy in the fundamental mode (figure 2.6(e)). With time, energy is gradually transferred towards waves with higher frequencies and solitary-like waves (approximately denoted by the dashed line 's') can be observed in the wavelet of time series from probe B (figure 2.6(f)). After the $3rd$ oscillatory cycle, a quasi-steady state is reached without further changes in energy distribution.

The dominant vertical modes of the internal waves can be identified by looking at the vertical profiles of the velocity components. The vertical profile of streamwise velocity allows identification of the dominant mode; the vertical profile of vertical velocity, which is more sensitive to particular waves passing through the chosen location, helps identification of other higher vertical modes.

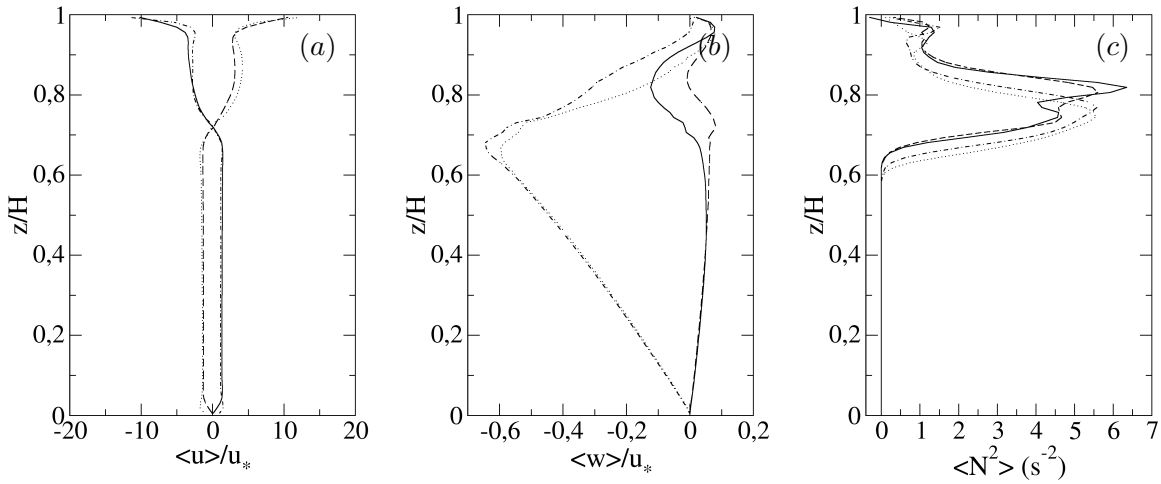

Figure 2.7: Vertical profiles at probe B of: (a), $\langle u\rangle/u_*$; (b), $\langle w\rangle/u_*$; (c), $\rangle N^2\langle$: ——, $\varphi = 0$; ·····, $\varphi = 0.5\pi$; – – – –, $\varphi = \pi$; – · –, $\varphi = 1.5\pi$.

In figure 2.7 we show the vertical profiles of the spanwise averaged velocity components at the probe B at several phases during the oscillatory cycle. We observe the presence of a three-layer structure: the near-surface layer, where stratification is weak, that is characterized by high velocity gradient and velocity which decreases rapidly up to the beginning of the strongly stratified region; a stratified middle layer, where the velocity decreases with a lower shear; the third layer in the lower unstratified region,

where velocity is nearly uniform and changes sign, due to the inversion of the mean current. Overall, the behavior is that of a two-layer response showing the presence of an upper layer moving along the wind direction and a lower layer moving in the opposite direction. This scenario corresponds to the first vertical mode V1, as described by Monismith (1985) for the system exposed to surface forcing. Two local maxima of $\langle N^2 \rangle = -g/\rho_0 \langle \partial\rho/\partial z \rangle$ form at $\varphi = 0$ and π and they collapse to a single one at $\varphi = 0.5\pi$ and 1.5π indicating that these variations of density profile are not permanent.

During the resonant two-layer response, the maximum streamwise velocity of the metalimnion is $\approx 5u_*$, and it reduces to $\approx 2u_*$ in the hypolimnion. Surface velocity locally reaches values of $20u_*$. The near-surface region follows the forcing oscillatory behavior with phase lag between streamwise velocity u and forcing τ about $\Delta\varphi \approx 0.2\pi$.

As observed by Lorke et al. (2002), under the influence of a seiching, the bottom boundary layer dynamics are governed by the oscillatory nature of the system. In our case, the bottom boundary layer is periodically driven by the internal seiches, as a system response to wind forcing, hence we use simple Stokes boundary layer (SBL) analysis for the oscillatory bottom boundary layer.

The Reynolds number, based on the Stokes viscous penetration length $\delta_S = \sqrt{2\nu/(2\pi f_w)}$, is $Re_\delta = U_0\delta_S/\nu$. As free stream velocity, we use the maximum velocity of the bottom layer and obtain $Re_\delta = 44.5$ that is strictly in the laminar regime (see for details Salon et al. (2007) and literature therein cited). Consistently, we do not observe any indicators of turbulent disturbances. In other words, the bottom boundary layer generated by the internal seiches, in the present case is weak and not able to produce substantial turbulence in the hypolimnion. The SBL behavior matches the one observed by Lorke et al. (2002) when analyzing field data, although in our study, a scale effect on Reynolds number is present. We note that Ulloa et al. (2019) found a large value of the turbulent intensity parameter in a region near the center of the basin in their real-scale simulation.

2.4.2 Forcing period $r_T = 2$

Variation of the forcing period dramatically changes the response of the basin. The time series of the interface height for the forcing period $r_T = 2$ is plotted in figure 2.8(a, b). After the initial fundamental wave response, characterized by a linear wave with the fundamental period (marked with the gray dashed vertical lines), the oscillation adjusts to the forcing period together with the appearance of high-frequency waves. Based on the analysis of Boegman et al. (2003) about high-frequency waves, these waves are excited by the nonlinear effects and we denote them as solitary-like. They cannot be associated with shear instability because they occur in a region where the Richardson number $Ri = \langle N^2 \rangle / \langle S^2 \rangle$ is well above the critical value. The nonlinear effects that excite solitary-like waves, in this case, are related to the destruction of the fundamental wave. Their presence just at probe A together with an inspection of the instantaneous field suggests that they are created locally, between probe A and the left end-wall, and they travel towards the left end-wall, where they lose a substantial part of their energy. According to Cooker et al. (1997) upon collision of a large-amplitude solitary wave with a vertical wall, it loses energy (to a dispersive wave train) and height, which explains why we do not observe these high amplitude, high-frequency waves later in the time series. Instead, high-frequency waves with lower amplitudes appear and remain present throughout the simulation. Given that the Richardson number is very high in the region of metalimnion, all of these high-frequency waves are solitary-like. At the nodal location B, the initial response corresponds to nonlinear mode V1H2, with frequency f_2, which has the same vertical structure as fundamental wave (V1H1) and horizontal structure in terms of second horizontal mode. However, as

the system adjusts to the forcing period, due to energy transfer, so the nonlinear waves do, as period of the dominant nonlinear wave adjusts to f_{w2}. In this case, we do not observe resonant amplification.

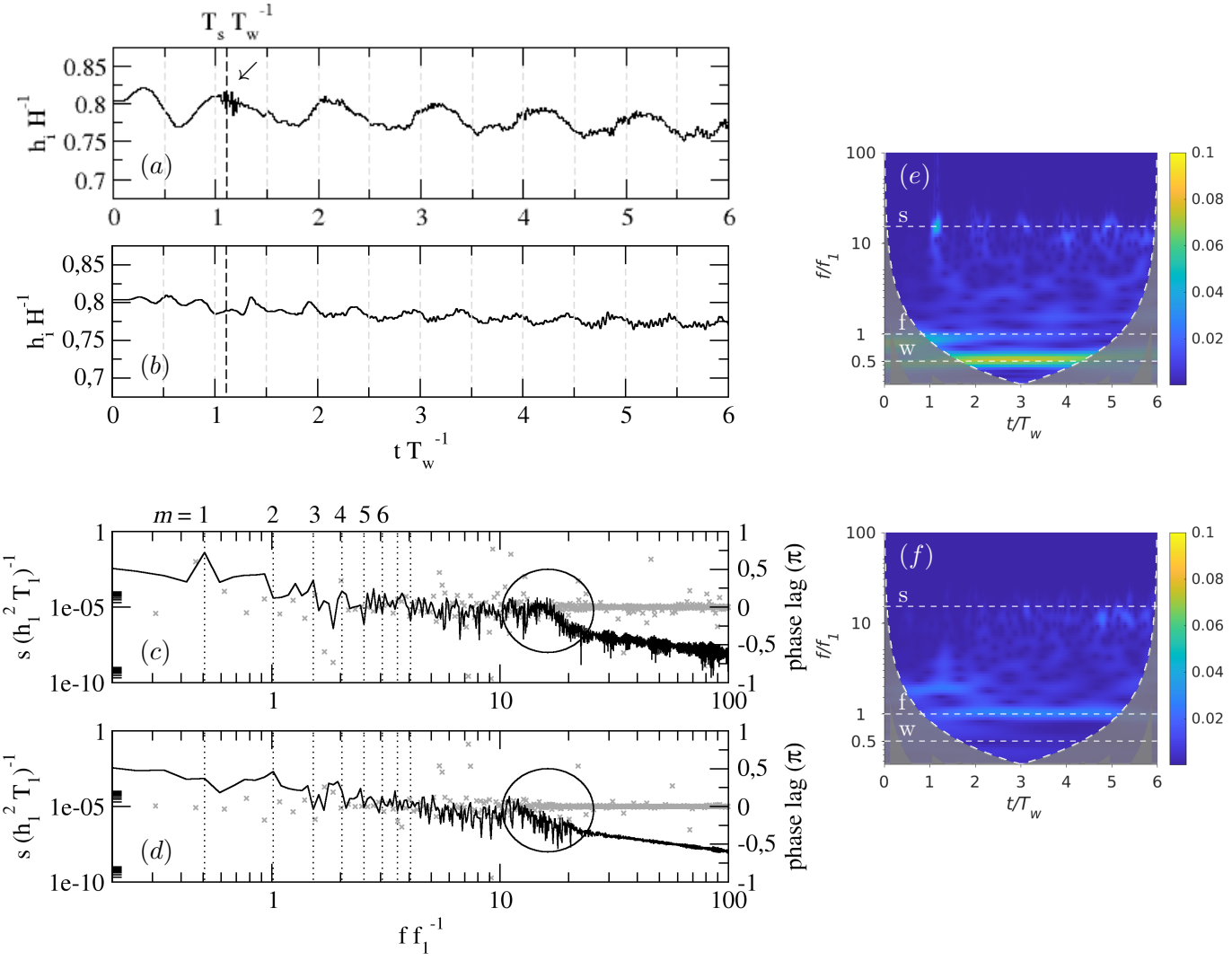

Figure 2.8: Panels (a, b) show the time series of non-dimensional interface height h_i/H for $r_T = 2$ plotted versus the number of forcing period at probes A and B, respectively. The dashed gray vertical lines denote the nondimensional time period T_1/T_w and multiple values, while dashed black vertical line denotes the nondimensional steepening time-scale T_s/T_w. Panels (c, d) contain nondimensional spectral energy of interface height (lines) and phase lag among isopycnals (x's) at probes A and B, respectively. Vertical dotted lines represent forcing frequency and its m-th superharmonics. Theoretical frequencies of modes of internal seiche can be read as integers from x-axis given that $f_n = nf_1$. Panels (e, f) show wavelet of interface height sampled at probe A and B, respectively, where colors represent absolute values of the CWT. . Dashed white horizontal lines denoted with letters indicate: w, forcing frequency f_w; f, fundamental frequency f_1; s, approximate frequency of solitary-like waves $\approx f_s$.

In spectral energy analysis of these time series (figure 2.8(c, d)), we can identify forcing frequency f_w as the most energetic. The energy spike that belongs to the fundamental wave V1H1 is found near f_1 at location A. At location B, that is nodal for fundamental wave, the spike of energy near f_1 a is associated

with a nonlinear wave that occurs as a superharmonic of the forcing frequency f_{w2} whose frequency is close to f_1. Higher super harmonics of forcing frequency can be identified: f_{w3} at non-nodal location A ; f_{w4}, f_{w5} at nodal position B. Phase lag near f_w and f_{w4} indicates that these waves are in form of higher vertical modes. There is increased energy in the region with solitary-like waves (circled) which is characterized by the absence of a phase-lag, indicating the presence of V1 mode.

The wavelet analysis of interface height series (figure 2.8(e, f)) shows that, initially, both the fundamental frequency and the forcing one are energized. During the second forcing period, the energy of the fundamental wave mode decreases rapidly (figure 2.8(e)), followed by the transfer of energy to nonlinear waves (figure 2.8(f)) and towards the high-frequency solitary-like waves. Upon transfer, energy is soon dispersed. After the decay of the fundamental mode, the energy of the wave with the frequency of forcing f_w rises. Part of this energy is transferred to higher modes f_{wm} up to the solitary-like waves that develop as a result of steepening of the nonlinear waves.

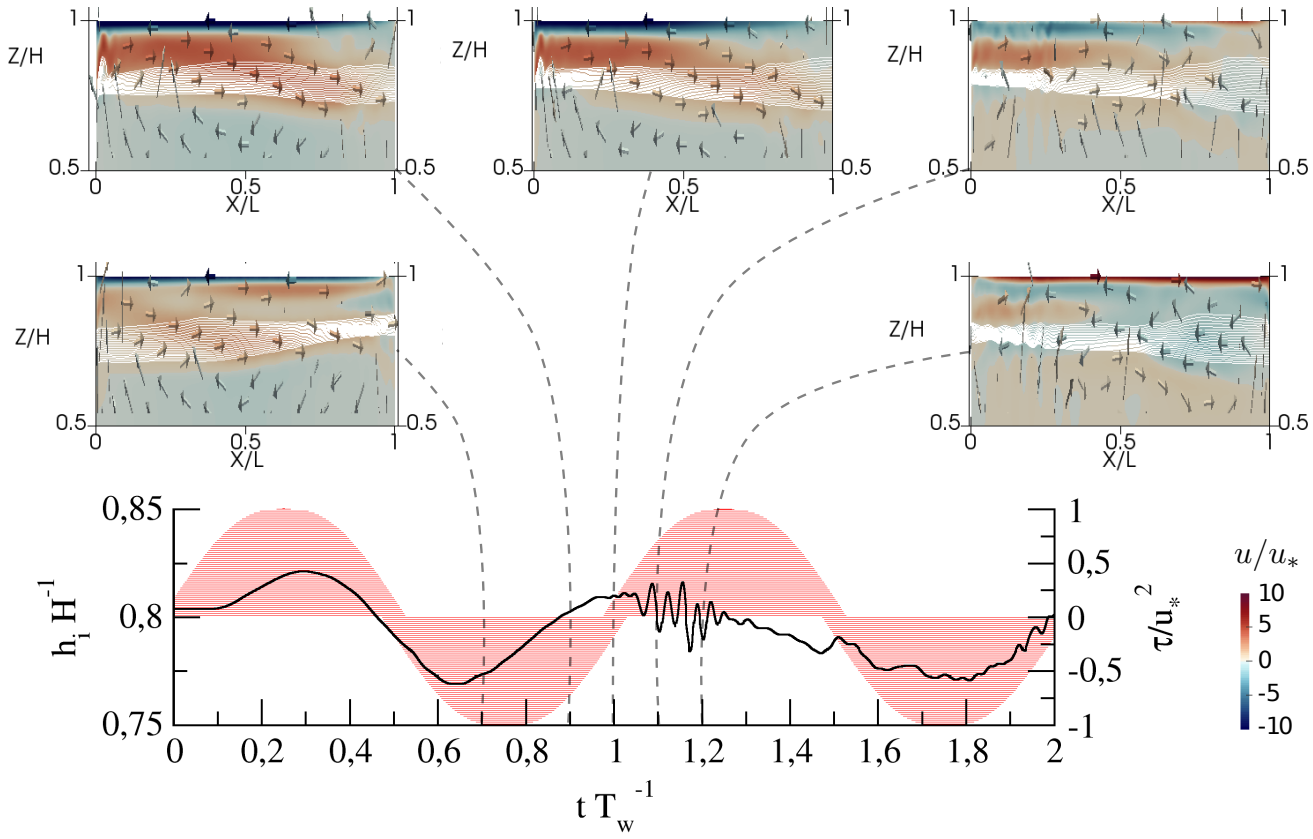

Figure 2.9: Preview of the behavior of the velocity and density field during the wave cancellation event. Time series display the oscillation of isopycnal ρ_0 at probe A while red areas display the state of the nondimensional forcing τ/u_*^2. Panels above the time series show internal fields at various times. White lines show the isopycnals in range $\rho_0 \pm 0.5\Delta\rho$, arrows show velocity direction and field is colored with nondimensional streamwise velocity u/u_*.

Antenucci et al. (2000) analyzed data from field observations using an analytical model and found that a forcing period equal to that of the internal wave is not enough for resonant amplification. If the wave is pre-existing, the phase between wind and wave plays an important role. A zero phase causes resonant amplification, while a phase equal to 180° (half-period) causes antiresonance and wave

cancellation. Vidal et al. (2007) further hypothesized that strong wind events that are out of phase with the dominant wave drain its energy and energize other vertical modes. Observing the destruction event on figure 2.8(a) (marked with an arrow), we see that the existing wave reaches its peak amplitude when forcing is at phase $\varphi = 0$, yielding a phase of about a quarter of the forcing period. This difference is enough to drain energy from the fundamental mode and cause a wave cancellation. This process occurs with energy transfer from linear fundamental wave to nonlinear and solitary-like waves, and subsequent energizing of the nonresonant wave with frequency f_w and higher vertical mode.

The behavior of the velocity and density fields during the wave cancellation events is depicted in figure 2.9. At $t/T_w = 0.7$ the wave starts its upward motion and develops positive streamwise velocity u in the middle layer while forcing produces negative u near the surface, same as in the bottom layer. At $t/T_w = 0.9$ to $t/T_w = 1$ the velocity in the middle layer intensifies, and spread and contraction of the metalimnion occur respectively at the left and at the right end-wall the right. At $t/T_w = 1$ the basin-scale V1 wave is at its own peak and about to start the downward motion (at the left side, where the sampling point is) and reverses circulation. At $t/T_w = 1.1$ close to the bottom and end-walls, u reverses, while most of the middle and upper layer are still strongly dominated with the forcing induced velocities from the previous forcing period. At the left side of the basin, where metalimnion is contracted, the short waves appear whose signature in u is visible throughout the upper part of the water column. At $t/T_w = 1.2$ both density and velocity field are favorable for the formation of V2 waves.

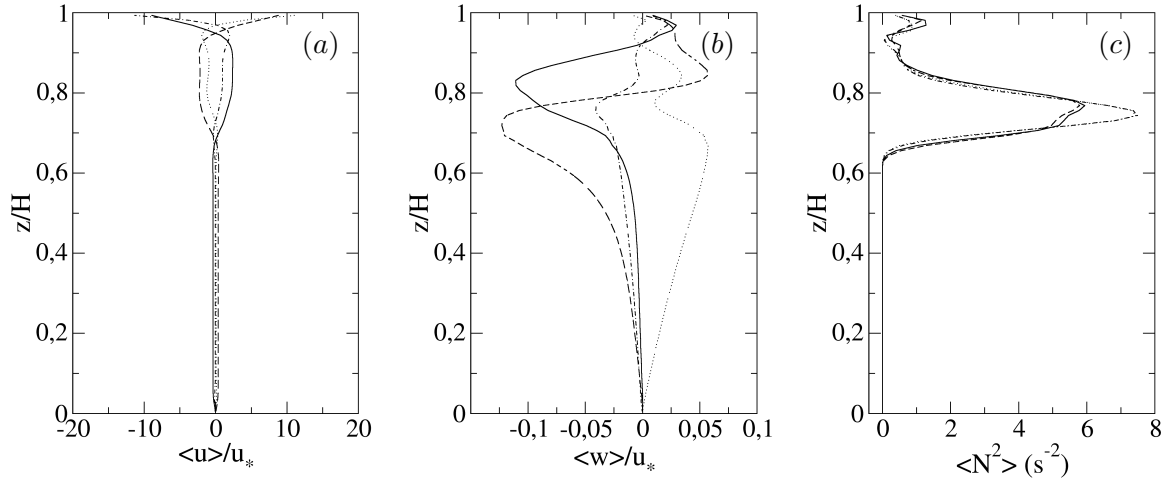

Figure 2.10: Vertical profiles at probe B of: (a), $\langle u \rangle / u_*$; (b), $\langle w \rangle / u_*$; (c), N^2. Line code: ——, $\varphi = 0$; · · · · ·, $\varphi = 0.5\pi$; – – – –, $\varphi = \pi$; – · –, $\varphi = 1.5\pi$.

The increase of the period of oscillation substantially changes the response of the basin, namely it moves from two-layer to three-layer dynamics. Vertical profiles of the averaged velocity components and squared buoyancy frequency at the probe B are shown in figure 2.10 at different phases during the oscillatory cycle. A clear three-layer response is depicted with two horizontal velocity inversions at the edges of the metalimnion. Basically, at the surface layer and at the bottom layer the flow moves along the same direction, and inversion is present in the intermediate stratified region. This comes from a combination of a spatially evolving wave (typical of oscillatory flows) and the inversion required by mass

conservation due to the presence of the end-walls. This structure clearly indicates that the dominant response of the system is in terms of second vertical mode V2 with forcing frequency. The maximum of the streamwise velocity of the metalimnion is about $\approx 3u_*$ and of hypolimnion $\approx 0.4u_*$. Vertical velocity is more sensitive to the passage of different waves. Together with profiles with one vertical reversal (at $\varphi = 0$ and 0.5π), that corresponds to the second vertical mode, we can observe a profile with no reversals (at $\varphi = 0.5\pi$) that correspond to the passage of a wave with the first vertical mode. The system adjusts to the forcing period via second vertical mode, while waves with first vertical mode remain present. The profile of N^2 shows periodic behavior where N^2 increases at $\varphi = 0.5\pi, 1.5\pi$ and decreases at $\varphi = 0\pi, 1\pi$. The increase of N^2 corresponds to stronger stratification as a consequence of the contraction of metalimnion, while the decrease of N^2 corresponds to the metalimnion spread, which is a behavior characteristic for the waves with second vertical mode. In this case, the Reynolds number of the bottom SBL is $Re_\delta = 12.6$ for which the flow is again in the strictly laminar regime.

2.4.3 Forcing period $r_T = 3$

A third forcing period was considered, resulting in the response of the interface height time series depicted in figure 2.11(a, b). At the non-nodal location A we observe that the initial response is in terms of nonresonant fundamental seiche (the fundamental period is marked by vertical dashed gray lines) as predicted for the two-layer system based on the results of Boegman and Ivey (2012). During the third forcing period, the fundamental wave degenerates, and solitary-like waves become dominant. We note that the fundamental wave is canceled and re-formed several times. The first cancellation is observed at the beginning of the second forcing period, similarly to the $r_T = 2$ case; fundamental wave peak appears at forcing phase $\varphi = 0$ which results in fundamental wave cancellation and formation of a new fundamental wave; the transition is always followed by energy transfer towards higher frequencies and appearance of the high-frequency solitary-like waves. At the nodal location B, the initial response has a half-fundamental period, therefore corresponding to V1H2 mode. At the beginning of the second forcing period, nonlinear and solitary-like waves with a half-forcing oscillatory period appear, corresponding to forcing superharmonic f_{w2}. Growth of nonlinear waves and appearance of solitary-like waves is not related to T_s, indicating that their origin has fundamentally different dynamics compared to that of the two-layer theory, by which the steepening time scale T_s is derived.

We show the spectral energy of the interface height time series in figure 2.11(c, d). At non-nodal location A, the highest energy peak is found at fundamental and forcing frequencies f_1 and f_w respectively; at the nodal location B, the superharmonic f_{w2} is even more energetic. At the non-nodal position, peaks of energy can also be observed for superharmonics f_{w4}, f_{w5} and, at the nodal position for f_{w4}, f_{w6}. Phase lag is generally high across most frequencies, indicating that the motion of isopycnals $\rho_0 \pm 0.25\Delta\rho$ is practically decoupled and that the system responds with higher vertical mode. This is also true for the region with solitary-like waves.

The wavelet analysis of the interface height shown in figure 2.11(e, f) indicates that fundamental and forcing frequencies are dominant at probe A (figure 2.11(e)). The wave with fundamental frequency has a particular behavior with respect to energy content, which is characterized by several events of increase and decrease of energy. These events coincide with the appearance of energy in the higher frequencies. The sudden losses in fundamental wave energy are caused by wave cancellation, due to phase difference between wave and forcing. Besides the solitary-like waves that originate from the wave cancellation events, there are energy bursts in solitary-like waves with lower frequencies whose energy increases with

each occurrence which will be discussed later.

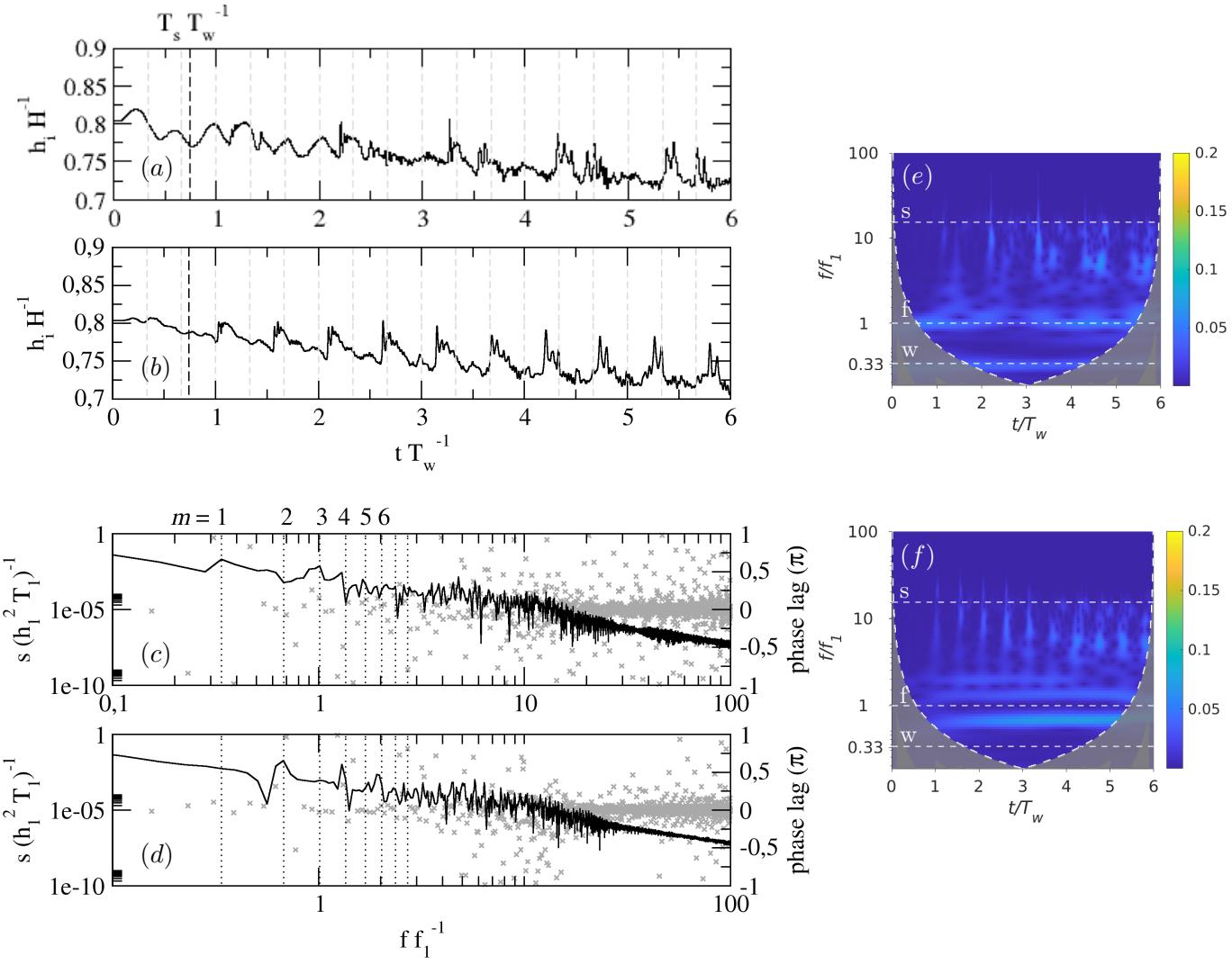

Figure 2.11: Panels (a, b) show the time series of non-dimensional interface height h_i/H for $r_T = 3$ plotted versus the number of forcing period at probe A and B, respectively. The dashed gray vertical lines denote the nondimensional time period T_1/T_w and multiple values, while dashed black vertical line denotes the nondimensional steepening time-scale T_s/T_w. Panels (c, d) show nondimensional spectral energy of interface height (lines) and phase lag among isopycnals (x's) at probe A and B, respectively. Vertical dotted lines represent forcing frequency and its m-th superharmonics. Theoretical frequencies of modes of internal seiche can be read as integers from x-axis given that $f_n = nf_1$. Panels (e, f) show wavelet of interface height sampled at probe A and B, respectively, where colors represent absolute values of the CWT. . Dashed white horizontal lines denoted with letters indicate: w, forcing frequency f_w; f, fundamental frequency f_1; s, approximate frequency of solitary-like waves $\approx f_s$.

At location B (figure 2.11(f)), substantial energy is contained in the nonlinear superharmonic f_{w2}. In fact, energizing of f_{w2} coincides with energy loss from both f_w and cancellation of f_1 upon which energy of f_{w2} remains constant throughout the simulation. This leads to the conclusion that the system adjusts to the f_{w2} response. Given that this wave is absent at location A, and this location is nodal for H2 waves,

we can identify this wave as nonlinear horizontal H2 mode. The wavelet analysis of the time record at probe B shows that nonlinear superharmonics originate from f_{w2}. Besides, we see the pathways of energy towards solitary-like waves which occur with period $0.5T_w$ (corresponding to f_{w2}). By inspecting the instantaneous fields, (discussed in the next section) we find that these are V2 mode solitary-like waves that periodically pass through the probe with frequency f_{w2}.

The vertical profiles of the spanwise-averaged velocity components are shown in figure 2.12. The streamwise velocity profile (figure 2.12(a)) has a three-layer structure similar to that of the $r_T = 2$ case, but it is substantially less uniform across the metalimnion. This indicates that the second vertical mode V2 dominates in the presence of other superimposed waves. Occasionally, metalimnion jet-like behavior appears, which is related to the V2 response. It reaches the velocity of about $4u_*$. By examining the instantaneous fields, we found that this behavior is associated with the occurrences of V2 solitary-like waves. Similar association of the V2 mode solitary-like waves with the metalimnic jet is in Boegman et al. (2003). Excluding the jet-like events, the maximum of the streamwise velocity in the middle layer is $\approx 2u_*$ and up to $\approx 0.4u_*$ in the lower layer. The vertical velocity profile (figure 2.12(b)) at $\varphi = 0.5\pi$ clearly belongs to the wave with the second vertical mode, while in other profiles different waves are superimposed. The metalimnion appears deepened compared to other cases (figure 2.12(c)), which is partially the consequence of substantially different duration of the numerical experiment. Even in this case ($Re_\delta = 15.4$), the bottom layer flow is strictly in the laminar regime.

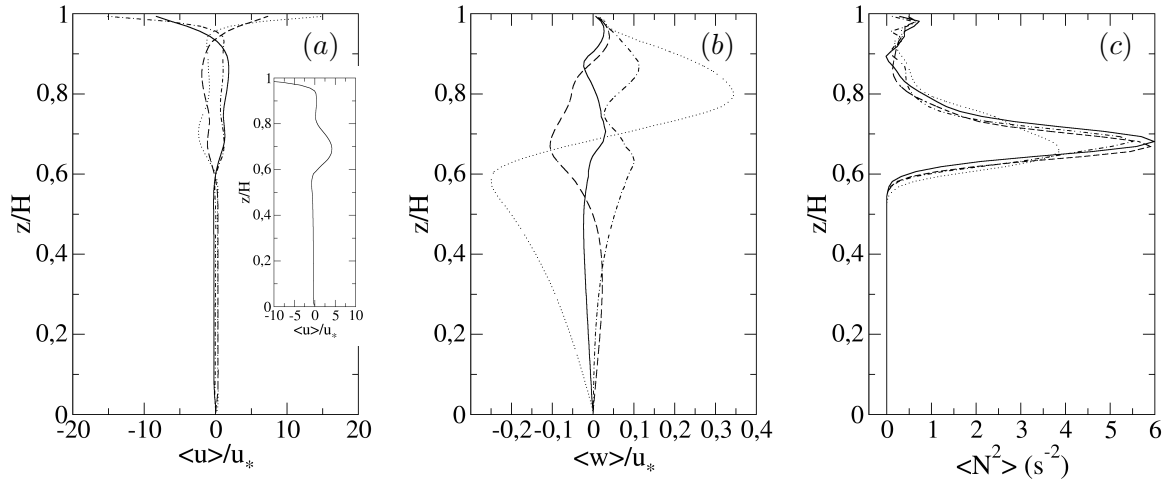

Figure 2.12: Vertical profiles at probe B of: (a), $\langle u\rangle/u_*$; subfigure showing the metalimnion jet at $\varphi = 1.6\pi$; (b), $\langle w\rangle/u_*$; (c), N^2: ——, $\varphi = 0$; · · · · ·, $\varphi = 0.5\pi$; – – – –, $\varphi = \pi$; – · –, $\varphi = 1.5\pi$. φ indicates the phase within the forcing cycle.

Ulloa et al. (2020) resonantly forced nonlinear V2H1 wave that is characterized by V2 undular bore and found that it is followed by a train of V2 solitary-like waves. Thorpe (1971, 1974) observed internal surge with similar characteristics but with the first vertical mode. In our case nonlinear V2H2 wave is the dominant response and its period corresponds to that of the passage of V2 solitary-like waves, therefore, V2H2 is likely the wave they originate from. The inspection of the structure of V2 solitary-like waves corresponds to the description of Ulloa et al. (2020) where each wave consists of the two cores

with opposite vorticity (not shown). While the association of the nonlinear V2 wave and V2 solitary-like waves corresponds to the one observed by Ulloa et al. (2020), the general response differs. Namely, we do not observe the differentiation on the quiescent and disturbed part of the domain by the nonlinear wave. This may be because in our case nonlinear response is nonresonant wave and there is a variety of other superimposed waves in the field.

2.4.4 Summary

In basins where metalimnion thickness cannot be neglected and when periodic forcing has period close to or greater than the fundamental one (which is the case of most small and mid-size lakes), only resonant forcing of V1H1 ($r_T \approx 1$) excite the response in terms of first vertical mode; forcing with larger forcing period produces a response with higher vertical mode, in the cases we tested $r_T = 2, 3$, the wave response has a second vertical mode. The excitation of the higher vertical modes by larger r_T is well expected because wave speed of wave with vertical mode Vn decreases roughly with n^{-1} (Monismith, 1987), which increases the period of these waves with n. We may argue that the limit for resonant excitation of V1H1 is $r_T \gtrapprox 1.5$ as determined by Boegman and Ivey (2007) for a two-layer system. The results of Boegman and Ivey (2007) are also valid for the initial response for forcing periods larger than those given by the above condition, where the initial response is in terms of the nonresonant fundamental wave. Differences arise after a time period when forcing conditions become unfavorable to the fundamental wave, and lead to its cancellation. This process results in transfer of energy from the fundamental mode to solitary-like waves through nonlinear mechanisms. In $r_T = 2, 3$ cases, the first cancellation occurs at about $\approx 1.15T_w$. Upon cancellation, the wave field develops differently depending on the forcing period. Namely, for $r_T = 2$, this cancellation is permanent; the system adjusts to forcing by energizing the V2H1 wave whose frequency corresponds to that of the forcing. For $r_T = 3$, the fundamental wave V1H1 re-forms and gets canceled several times during the oscillatory cycles; upon the first cancellation, forcing superharmonic f_{w2} is energized as nonlinear V2H2, while the energy of f_w decreases, therefore system adjusts to nonlinear f_{w2} and it becomes the dominant response.

Generalizing the results, a lake-like system with a fundamental period shorter than diurnal and having relatively thick metalimnion compared to other layers is susceptible to the formation of higher vertical modes and will respond with higher vertical mode waves unless fundamental wave is resonantly forced with $r_T \lessapprox 1.5$. The response can adjust to forcing frequency f_w or to its superharmonic. The ability of the system to adjust to the periodicity of forcing is closely related to the occurrence of nonlinear and solitary-like waves, and they might be a bridge for internal adjustment.

2.5 Influence of Inclination of the end-walls

Here we investigate how the inclination of the end-walls modifies the response of the basin to the periodic wind forcing discussed in the previous Section. Specifically, we vary angles of the end-walls $\alpha = 30°, 45°, ..., 90°$, where the latter stands for vertical walls (see figure 2.1). This bathymetry is representative of alpine glacier-carved lakes whose water basins are typically found in steep valleys.

The variations of the domain are obtained by varying the angle α that is the angle between the end-walls and the bottom along L (figure 2.1). The end-walls are varied such that the length of the domain at the height of the interface where $\rho = \rho_0$ (h_2) is kept constant. Shintani et al. (2010) gave a formulation of the effective Wedderburn number that accounts for the sloping bottom geometry. The

effective Wedderburn number slowly changes with geometry variations due to physical characteristics such as symmetry over the yz-plane, constant pycnocline length, and relatively steep slopes. We found that for the different geometrical configurations herein investigated, differences in Wedderburn number are of the order of 10^{-3}, therefore (1.1) is valid for all the cases.

As in the previous Section, turbulent statistics are obtained averaging the instantaneous field data along the spanwise direction and shown at a given time instant during the last forcing period. Due to continuous mixing during the simulations, averaging in time was considered not appropriate, thus we discuss separately the cases at constant r_T and analyze the effect of the inclination of the end-walls.

2.5.1 Resonant response, $r_T = 1$

The time series of interface height of figure 2.13(a, b), show that, as α decreases, high-frequency solitary-like waves (circled) appear before the steepening time scale T_s, indicating that the mechanism of their formation is not the gradual energy transfer from linear waves to the nonlinear ones and their subsequent steepening. As in the previous Section, the presence of solitary waves in the time series is characterized by high-frequency pulse-like waves superimposed on the main almost sinusoidal low-frequency wave-field. Another effect of inclination of the sidewall is that the time series are smoother, with less pronounced solitary-like waves for small values of α. The time series appear very similar among them, apart for $\alpha \leq 45°$, for which the amplitude of the oscillation of density interface reduces substantially with time at both probes. This matches the behavior speculated by Ulloa et al. (2020), that waterbodies with a lower slope angle will escape resonance sooner than the ones with the steep slopes due to enhanced mixing at the sloping boundaries that changes the background stratification. We will further discuss these effects later on.

The energy spectra of the time series of interface height are very similar for all inclination angles of the end-walls (not shown). Also, the phase lag between the two chosen isopycnals is generally low, except at frequencies near f_1 in the middle of the channel. This corresponds to periodic spread and contraction of metalimnion in the middle of the basin which is the indicator of the formation of higher vertical modes. This effect is more pronounced for the lower inclination of the end-walls.

The wavelet analysis of the time series for $\alpha = 30°$ shown in 2.13(f, g) reveals that solitary-like waves form before T_S, at the end of the first forcing period, which can be observed as an increased amount of energy near the dashed line 's' (figure 2.13(f)). We note that, before reaching high-frequency waves, energy is transferred through the lower frequencies. The origin of these waves may be attributed to forcing-induced nonlinear surge, like the ones observed by Farmer (1978), that quickly steepens, thus producing solitary-like waves. This is confirmed by inspecting at the instantaneous fields: figure 2.13(h) shows the formation of the surge at the interface (denoted with a downward triangle), while figure 2.13(i) shows the degeneration of the surge into the solitary-like waves.

The energy contained in the region of the solitary-like waves is relatively low until the third forcing period, which corresponds to the formation of solitary-like waves by the nonlinear steepening (timed by T_S) after which their energy is reduced. This behavior is significantly different than that of the rectangular case, where, for $t > T_S$, a quasi-steady state is reached. The cause of this behavior will be discussed later in this section.

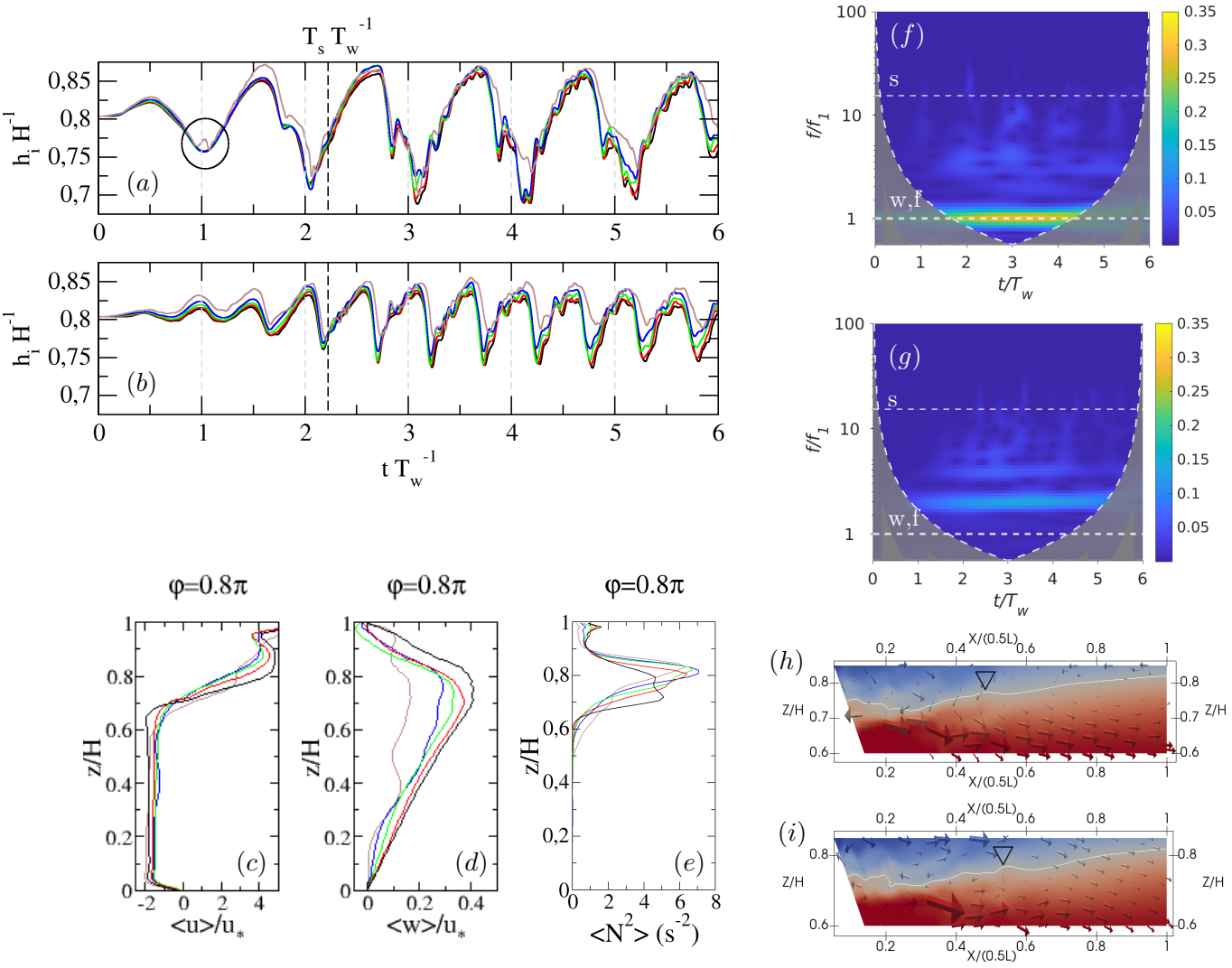

Figure 2.13: Panels (a, b) contain time series of interface height for $r_T = 1$ and different values of α at probe A and B, respectively. Panels $(c - e)$ contain vertical profiles of velocity component and $\langle N^2 \rangle$ sampled at probe B for all values of α. Panels (f, g) contain wavelets for $\alpha = 30°$ at probe A and B repectively. Dashed white horizontal lines denoted with letters indicate: w, forcing frequency f_w; f, fundamental frequency f_1; s, approximate frequency of solitary-like waves $\approx f_s$. Panels (h, i) show slices through the instantaneous density field together with velocity vectors and interface $\rho = \rho_0$ denoted with white line for the case $\alpha = 30°$ at time instants $t/T_w = 0.9$ and $t/T_w = 1$. Color code for $(a - e)$: $\alpha = 90°$, $\alpha = 75°$, $\alpha = 60°$, $\alpha = 45°$, $\alpha = 30°$.

Vertical profiles of averaged streamwise and vertical velocity components and squared buoyancy frequency are shown in figure 2.13$(c - e)$. The vertical profiles of buoyancy frequency squared (figure 2.13(e)) show that the epilimnion becomes more stratified for steeper slopes. Given that the initial state of epilimnion is uniform density $\langle N^2 \rangle = 0$, this indicates that, as the slope steepens, there is more mixing in the upper layer. Going down, we observe that for steep slopes $\alpha = 75°, 90°$, a maximum of $\langle N^2 \rangle$ (indicating pycnocline) is shifted downwards. Both these phenomena can be explained by vigorous corner flow at the downwind end that appears for steep slopes (as the one described by Monismith (1986), Stevens and Imberger (1996)). This flow cannot penetrate through the metalimnion,

but it erodes it with time. On the lower end of the metalimnion, the stratified region, with nonzero $\langle N^2 \rangle$ spreads downwards with a decrease of α. Mixing under the metalimnion can be explained in relation to the reduction/decrease of the solitary-like waves from the wave field (as observed in figures 2.13(a, b, f, g)), as a consequence of breaking of the solitary waves at the slopes, which is known to cause mixing in the lower layer (i.e. Michallet and Ivey (1999)). Widening of the metalimnion is known to promote the formation of higher vertical modes.

The vertical velocity profiles (figure 2.13(d)) do not exhibit reversals, indicating V1 as the dominant vertical mode for all end-walls angles. However, as α decreases, a substantial reduction of the vertical velocity and additional spatial oscillations occur. The first one is explained by the resonance-escape hypothesis of Ulloa et al. (2020) where the latter indicates the existence of higher vertical modes superimposed over the profile of the dominant V1H1 mode. The additional waves drain energy from the fundamental mode, causing the further reduction of the amplitude of vertical velocity, as observed in figure 2.13(d).

The vertical profile of streamwise velocity (figure 2.13(c)) changes little with the variation of the angle of the end-walls and the behavior roughly corresponds to that described for the rectangular domain. We observe that as α decreases the vertical profiles become less sharp which is related to the appearance of higher vertical modes that create non-uniform distribution of velocity in each layer.

The spatial oscillations observed in the vertical velocity profiles together with the progressive irregularities of profiles of horizontal velocity component, for low sidewall angles α, indicate the increase of the number of shearing layers.

The quantity $\langle S^2 \rangle = \langle \partial u/\partial z \rangle^2 + \langle \partial v/\partial z \rangle^2$ is indicative of regions with high shear, where shear-induced turbulence is more likely to occur if stratification is weak resulting in low values of Richardson number. The largest values are close to the free surface in all cases, due to the action of the wind stress. The second region with high $\langle S^2 \rangle$ is found in the lower end of metalimnion where velocity reverses (see figure 2.13). Lowering of α introduces higher shear further down the water column, as a direct consequence of the occurrence of the higher vertical modes. Indeed, they produce a number of layers moving with different velocities. In all cases, shear is evident close to the bottom surface, indicating the presence of a weak boundary layer, and at the inclined walls, for a low value of α. As already discussed the bottom boundary layer is very weak and in the laminar regime.

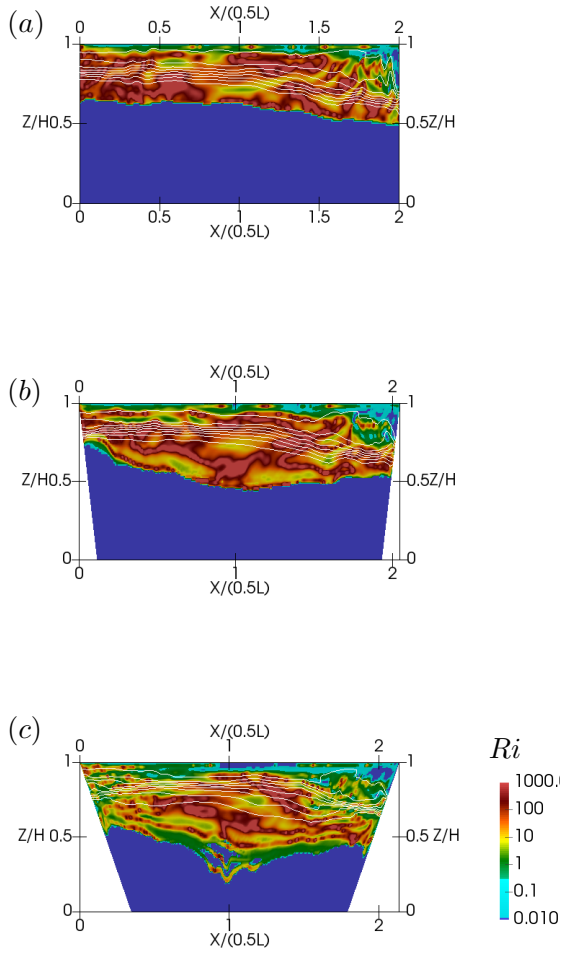

Figure 2.14: Richardson number Ri for $r_T = 1$ at $\varphi = 1.2\pi$: (a), $\alpha = 90°$; (b), $\alpha = 60°$; (c), $\alpha = 30°$. The turquoise color scale represents subcritical Ri.

This holds also in presence of inclined walls.

The gradient Richardson number$Ri = \langle N^2\rangle/\langle S^2\rangle$ shown in figure 2.14 quantifies the relative importance of the local stabilizing buoyancy forces against the destabilizing effect of shear. In general, in our simulations, Ri is very high, due to the very strong, laboratory-type stratification used. There is a thin near-surface layer where Ri is under the critical value $Ri_{cr} = 0.25$, which corresponds to the surface mixed layer, where $\langle N^2\rangle$ is very low and $\langle S^2\rangle$ is very high. This is the case also in real scale basins. The region with subcritical and negative Ri can be found near the corner due to the return jet, where the downward jet creates overturns. We observe that the downward reach of this jet increases with α. In the interior, Ri is generally supercritical; exceptions are the intermittent regions with subcritical Ri that appear at the lower edge of metalimnion (where N^2 is very low) for lower α. For the lowest α some wider regions with $Ri < Ri_{cr}$ are observed, in particular near the walls, as a consequence of wave breaking that will be further discussed in the following paragraphs. We acknowledge that due to laboratory-type setup there is a lack of patches with subcritical Ri that would produce shear instabilities and turbulence in the interior, compared to the real lakes (Saggio and Imberger, 2001).

In our numerical experiments, as in real lakes, the flow is strongly dominated by the internal wave field characterized by continuous variations in space and time which produces high intermittency. In such situations, vertical fluxes (such as $\langle\rho'w'\rangle, \langle u'w'\rangle$...) appear at a similar rate as down-gradient and counter gradient (Saggio and Imberger, 2001), indicating the presence of reversible fluid rearrangement, stirring (see Linden (2018), Villermaux (2019), Caulfield (2021)). This characteristic of lakes makes it difficult to quantify the irreversible part of vertical density flux $\langle\rho'w'\rangle$ and subsequently the buoyancy flux $B = g/\rho_0\langle\rho'w'\rangle$, that are needed in order to calculate the diffusivity of density $K_\rho = \langle\rho'w'\rangle/\frac{\partial\langle\rho\rangle}{\partial z} = B/N^2$. The vertical fluxes are dominated by the reversible component in all simulated cases. In other words, these quantities are not very robust for quantification of mixing in the case herein studied.

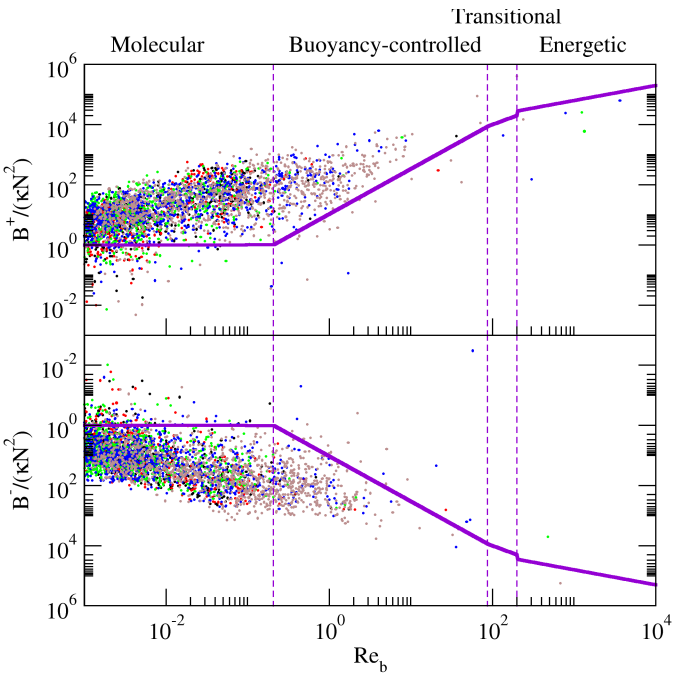

Figure 2.15: Non-dimensional buoyancy fluxes $B/(\kappa\langle N^2\rangle)$ as function of turbulence intensity parameter Re_b for $r_T = 1$ at $\varphi = 0.8$. Directly calculated positive B^+ and negative B^- buoyancy flux. Thick lines represent: ■ Bouffard and Boegman (2013) parametrization for $Pr = 500$. Color code: ■$\alpha = 90°$, ■$\alpha = 75°$, ■$\alpha = 60°$, ■$\alpha = 45°$, ■$\alpha = 30°$.

There are several methods that have been developed in the literature to extract information on the turbulent mixing: the widely used Osborn-Cox method (Osborn and Cox, 1972) evaluates the turbulent diffusivity of the scalar, after some assumptions which may be hardly verified in transitional non-equilibrium flows; the available potential energy methods (i.e. Winters et al. (1995)) directly relate changes in the available potential energy to irreversible diapycnal mixing; finally, there are pa-

rameterizations which constitute a simple and efficient way to obtain the desired field. We follow this strategy and use of parametrization of Bouffard and Boegman (2013).

The laboratory-scale parametrization of K_ρ for Prandtl number $Pr = 0.7$ proposed by Shih et al. (2005) was extended in the range $0.7 < Pr < 700$ by Bouffard and Boegman (2013). These models are based on the strong correlation between K_ρ and the turbulence intensity parameter $Re_b = \epsilon/(\nu N^2)$, where ϵ is the dissipation rate of turbulent kinetic energy, $K_\rho = C_1 \nu Re_b^n$ where C_1 and n are constants characteristic for mixing regimes initially defined by Shih et al. (2005) and successively expanded by Bouffard and Boegman (2013) as: molecular, buoyancy-controlled, transitional and energetic regime.

We calculated turbulence intensity parameter (or Reynolds buoyancy number) Re_b using dissipation rate $\epsilon = -(\nu + \langle \nu_{sgs} \rangle)\langle \frac{\partial u_i''}{\partial x_j} \frac{\partial u_i''}{\partial x_j} \rangle$, $i, j = 1, 2, 3$ and buoyancy frequency $\langle N^2 \rangle$.

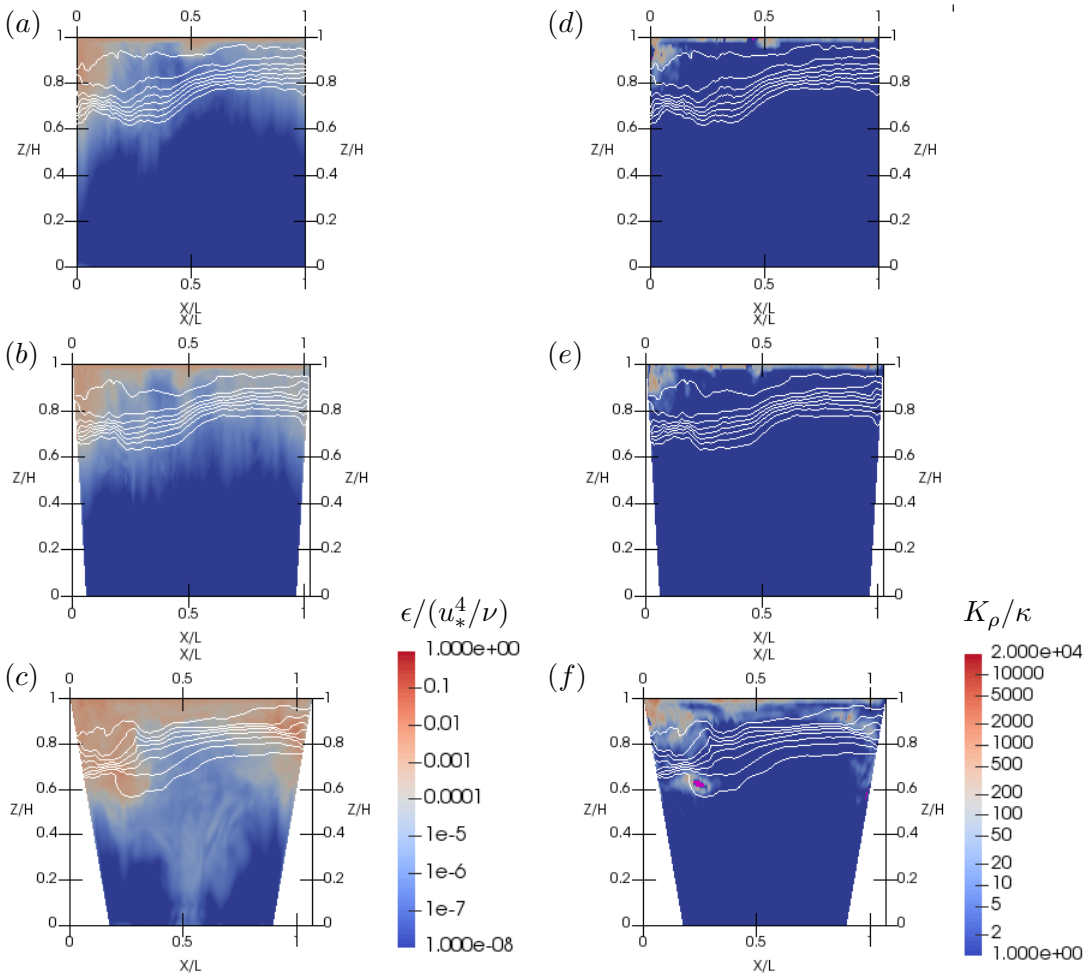

Figure 2.16: Fields of nondimensional turbulent dissipation rate (a, b, c) and turbulent diffusivity of density K_ρ/κ (d, e, f) for $r_T = 1$ at $\varphi = 0.4\pi$: (a, d), $\alpha = 90°$; (b, e), $\alpha = 60°$; (c, f), $\alpha = 30°$. White lines represent isopycnals. Pink color represents the unstable stratified regions with negative $\langle N^2 \rangle$.

Instantaneous resolved buoyancy fluxes in metalimnion for the phase $\varphi = 0.8\pi$ are plotted as a function of the turbulence intensity parameter $Re_b = \epsilon/(\nu\langle N^2 \rangle)$ in figure 2.15. As metalimnion, we considered the region $0.5 < z/H < 0.9$, which is wider than in the initial setup, in order to account for metalimnion spread due to mixing (see figure 2.13(e)). We show the values of positive and negative

buoyancy flux events as B^+, B^- made nondimensional with κN^2. We are not replacing $B/(\kappa N^2)$ with the equivalent expression K_ρ/κ because the first contains events of reversible fluid rearrangement which do not contribute to turbulent mixing. We note that in our simulations the events with Re_b values are significantly lower than in the real scale simulations of Ulloa et al. (2019) where typical values of Re_b in metalimnion are $\approx 10^2$ and at the sloped walls from about 10^2 to 10^5. Vertical lines divide different regions as defined by Bouffard and Boegman (2013). Most of the distribution is found to be in the molecular and buoyancy-controlled regimes. This is due to the laboratory scale employed in our study, which is better suited for the analysis of internal wave dynamics rather than for the analysis of mixing. The values obtained in our simulations are higher than those estimated using Bouffard and Boegman (2013) parametrization for $Pr = 500$, probably due to the reversible buoyancy fluxes associated with internal waves. The effect of the angle α is hardly detectable from these plots since the dots are overlapped over the same regions, but histograms (not shown) show the shift of distribution towards higher values for lower α.

Spatial distributions of the turbulent dissipation rate and turbulent diffusivity of density calculated using Bouffard and Boegman (2013) parameterization based on laboratory and numerical data are shown in figure 2.16.

Turbulent dissipation rate ϵ (figure 2.16$(a-c)$) is larger near the surface and near the corner where vigorous corner flow is present. With the decrease of α, we observe that spatial distribution of dissipation rate changes substantially; regions with significant dissipation rate, that are in the path of the downward beams radiating off-slopes, penetrate further into the hypolimnion; for lowest values of α we find high dissipation rate in the regions where the metalimnion encounters the end-walls. For the lowest inclination angle, large nondimensional dissipation rate $\epsilon/(u_*^4/\nu)$ occurs in metalimnion near the walls $\sim 10^{-2} - 10^{-3}$ while in the interior it is $\sim 10^{-5} - 10^{-6}$. This difference is close to the one observed by MacIntyre et al. (1999) for onshore and offshore dissipation rates (two to three orders of magnitude) while it is somewhat higher than the one simulated by Ulloa et al. (2019) and substantially higher than the one observed by Wain and Rehmann (2010).

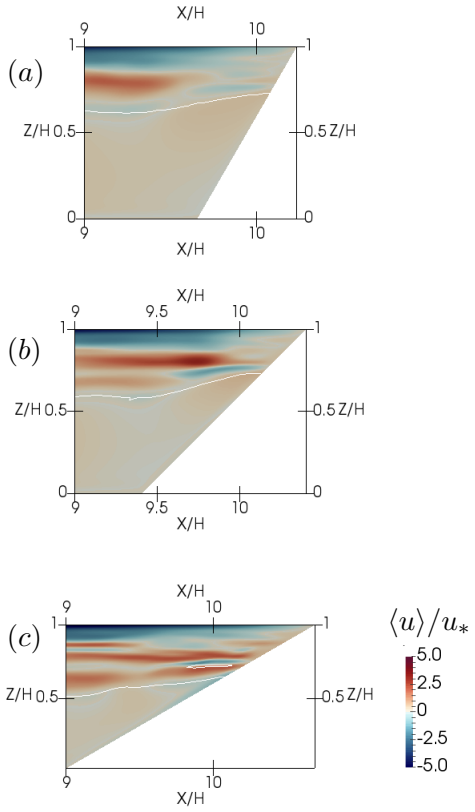

Figure 2.17: Nondimensional streamwise velocity component for $r_T = 1$ at $\varphi = 0$ for: (a), $\alpha = 60°$; (b), $\alpha = 45°$; (c), $\alpha = 30°$. The line shows slope criticality parameter $\varepsilon = 1$

The turbulent diffusivity of density K_ρ (figure 2.16$(d-f)$) for steep slopes is high only near the surface and corner, where mixing is a direct consequence of forcing. As slope angle decreases, we observe some mixing also near the walls, at the edges of the metalimnion. The increase of mixing as the slope moves from steep to moderate, together with lowering of mixing location toward the lower end of metalimnion for gentle slopes, corresponds to the behavior associated with solitary wave breaking (Michallet and Ivey, 1999, Boegman et al., 2005a) and shear-induced convective mixing Lorke et al. (2005) at the sloped walls.

For the lowest angle $\alpha = 30°$, we observe the overturn event (region with negative $\langle N^2 \rangle$) at the lower end of metalimnion. We also observe downward beam-like activity near the sloped walls, and we investigate the criticality of the slopes, where slopes with angle equal to natural internal wave propagation angle are considered critical. We use the slope criticality parameter (Garrett and Kunze, 2007, Gayen and Sarkar, 2010, 2011) defined as $\varepsilon = \tan\alpha / \tan\theta$, where $\tan\theta = \sqrt{\omega_w^2/(\langle N^2 \rangle - \omega_w^2)}$ is the slope of the forced internal wave and corresponding frequency $\omega_w = 2\pi f_w$. Slope criticality and observed beams are shown in figure 2.17. Slopes are near-critical at the bottom edge of metalimnion (white line) and supercritical above it. In the streamwise velocity we observe the downward beams, that radiate away from the slopes, which is a known behavior at the supercritical slopes (Sarkar and Scotti, 2017). These downward beams can induce turbulence and overturns on their path (Aucan et al., 2006). This explains the particular spatial distribution of Ri, where cases with low α show regions in the deep interior where the Richardson number is near-critical or subcritical. For $\alpha = 30°$, there is a weak downslope flow near the critical region of the slope, which induces weak mixing ($K_\rho \approx 20\kappa$) at the sidewalls and creates a region with subcritical Ri.

Near-shore mixing can be generated by seiching currents or breaking of internal waves. We observed in both time series and their wavelet analysis, that solitary-like waves are substantially reduced for low α. In figure 2.18 we can observe the formation of an unstable layer during the upslope seiching event that corresponds to the shear-induced convective mixing as described by Lorke et al. (2005). We can therefore conclude that the increased mixing and dissipation rate near the wall is due to the combination of wave breaking events and shear-induced mixing.

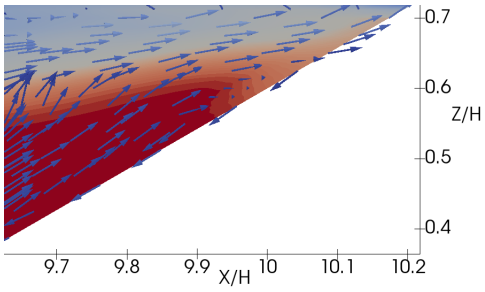

Figure 2.18: Contours of density field and velocity direction for $\alpha = 30°$ at $\varphi = 1.8\pi$ showing generation of unstable stratification during the upwelling event.

Time development of horizontally (along x and y directions) averaged field $\langle N^2 \rangle_h$ is shown in figure 2.19. In all cases, deepening of the metalimnion is more rapid during the initial transient, when shear-induced mixing occurs. According to Spigel and Imberger (1980) this mixing is later damped by the internal waves and the deepening slows down. There is a clear tendency of faster metalimnion deepening for basins with lower α. It should be stressed that this deepening weakly stratifies the hypolimnion (that initially has uniform density) and it becomes susceptible to the occurrence of internal waves. On the other hand, deepening does not cause such dramatic changes in the stratified region, in terms of relocating isopycnals as seen in figures 2.13(a, b) and 2.16.

The cross-examination of signal analysis of the time series, velocity, indicators of stratification and turbulence fields suggests the following scenario: after the initial transient, the mechanism that deepens the metalimnion for lower slope angles is a combination of wave breaking, seiching currents, downward beams and the presence of higher vertical modes. Due to wave breaking, shear-induced mixing and near-critical or supercritical slopes, fluid under the metalimnion is getting mixed near the boundaries, whereas the higher vertical modes enhance the intrusion that transports this mixed fluid towards the interior (Wain and Rehmann, 2010).

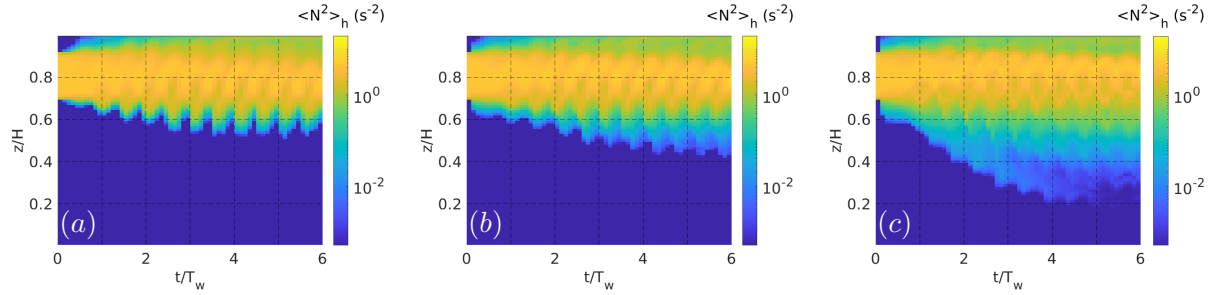

Figure 2.19: Time development of the horizontally averaged buoyancy frequency squared $\langle N^2 \rangle_h$ for: (a), $\alpha = 90°$; (b), $\alpha = 60°$; (c), $\alpha = 30°$.

2.5.2 Nonresonant response and wave destruction, $r_T = 2$

In the interface height time series of figure 2.20(a, b), we observe similar oscillatory behavior for cases with different angles of the end-walls. First, the fundamental mode is excited, later on, the forcing frequency dominates the oscillatory cycle. The inclination angle of the end-walls does not affect the response much. For lower inclination angles high-frequency waves appear earlier, being less pronounced in the latter forcing periods compared to the rectangular case, likewise the case of resonant forcing. A larger quantitative variation of the amplitude of oscillation of the density interface occurs for $\alpha \geq 45°$. There is a characteristic behavior of interface height to decrease with time and this decrease is greater for larger α. This is due to the already discussed erosion of the upper side of the metalimnion by forcing. We notice that, as in the previous case, solitary, pulse-like waves appear earlier in the time series, but are substantially reduced at later times for the low α cases. The explanation for this behavior is the same as for $r_T = 1$.

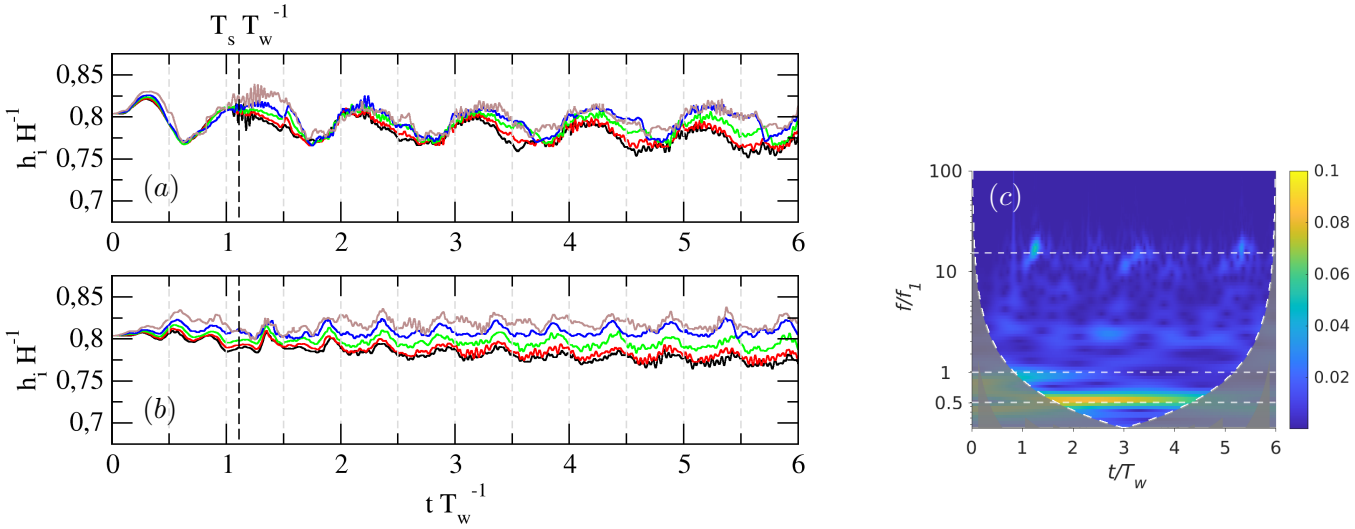

Figure 2.20: Panels (a, b) contain time series of interface height for $T_w/T_2 = 2$ sampled at probe A and B for all values of α. Panel (c) contain the wavelet for $\alpha = 30°$ at probe A. Color code for (a, b): ■$\alpha = 90°$, ■$\alpha = 75°$, ■$\alpha = 60°$, ■$\alpha = 45°$, ■$\alpha = 30°$.

The response in terms of spectral energy of these time series does not exhibit substantial modification

from case to case (not shown). For all inclination angles, f_w and f_{w2} are the dominant response frequencies. Phase lag around forcing frequency increases with a decrease of α indicating stronger V2 response for lower inclination angles. The wavelet for $\alpha = 30°$ shown in figure 2.20c is very similar to that of the rectangular case. The main differences are that high-frequency waves appear earlier (at $\approx 0.5t/T_w$) and that f_w and its superharmonics are more energetic.

The inclination of the walls produces only minor modifications of the streamwise velocity profiles. The streamwise velocity maximum at the metalimnion is up to $3 - 4u_*$ and at the hypolimnion $0.4 - 0.7u_*$. Vertical velocity profiles show a variety of profiles with a different number of velocity reversals. Profiles for cases with lower α tend to have more vertical velocity reversals that intrude deeper into the interior of the basin. Profiles of buoyancy frequency show similar behavior as in the $r_T = 1$ case. In addition, we can observe the tendency of cases with lower α to have multiple local maximums, indicating the formation of a multiple-layer structure.

Given that we identified the second vertical mode as the dominant response for forcing $r_T = 2$, we are interested in the analysis of how different responses affect the spatial distribution of internal fields.

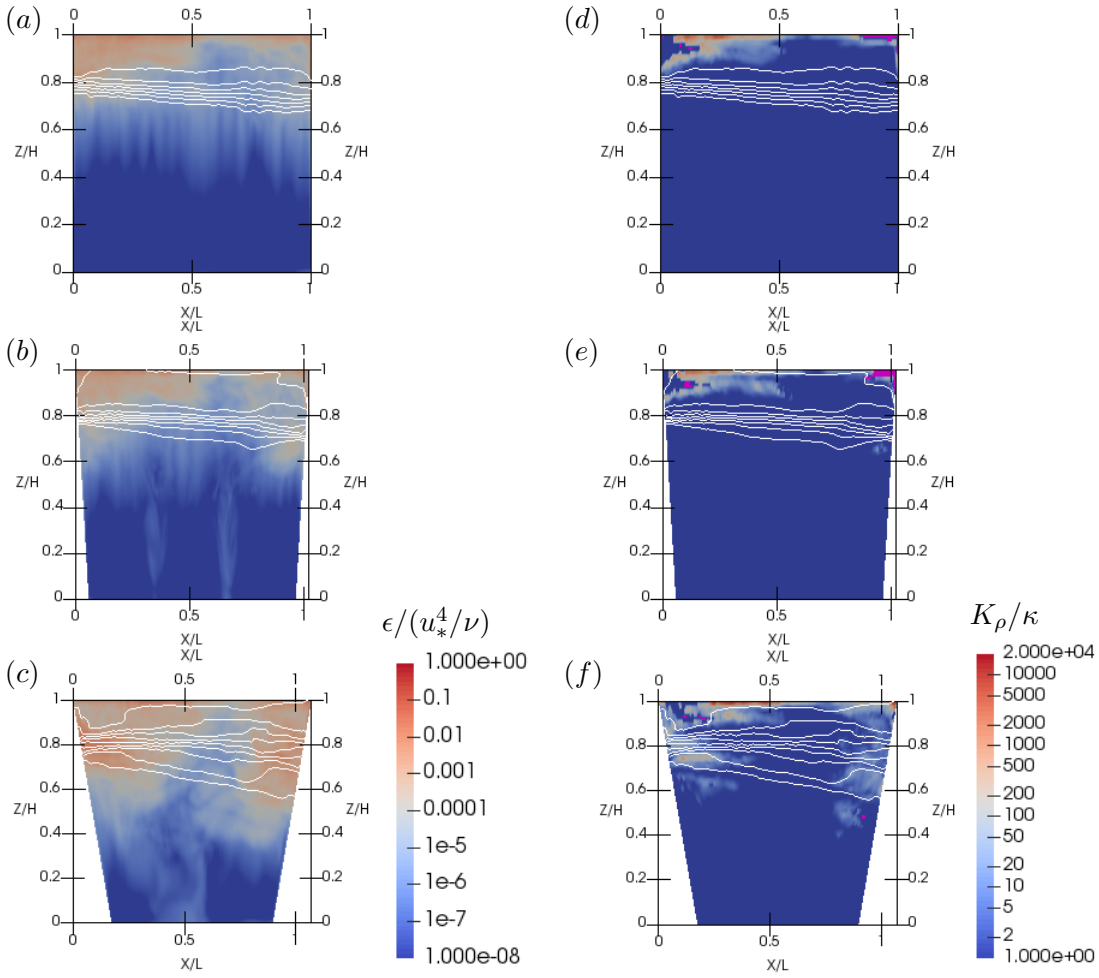

Figure 2.21: Fields of nondimensional turbulent dissipation rate (a, b, c) and turbulent diffusivity of density K_ρ/κ (d, e, f) for $r_T = 2$ at $\varphi = 0.4\pi$: (a, d), $\alpha = 90°$; (b, e), $\alpha = 60°$; (c, f), $\alpha = 30°$. White lines represent isopycnals. Pink color represents the unstable stratified regions with negative $\langle N^2 \rangle$.

The tendency of cases with lower α to develop multiple shearing layers is present for $r_T = 2$, similar to the case $r_T = 1$. Due to the nature of the V2 response, for $r_T = 2$, there are two layers with high shear, corresponding to two regions with horizontal velocity reversals. Nondimensional turbulent dissipation rate ϵ and turbulent diffusivity of density K_ρ shown in figure 2.21 exhibit similar characteristics as in the previous case; most of the dissipation rate and mixing occurs near the surface, while the decrease of α promotes the intrusion of dissipation rate and mixing events, from the near-wall region further into the interior. In figure 2.21, we can also observe substantial larger amplitude of the V2 mode for the lowest values of α as isopycnals have a much wider opening.

The turbulent dissipation rate has higher values in the region of the first horizontal velocity reversal compared to the $r_T = 1$ case. Still, most of the dissipation rate is a direct consequence of forcing and is located near the surface and near the corners. For $\alpha = 60°$ (figure 2.21(b)) we observe additional dissipation rate near the walls, under the intersection of walls and metalimnion. For $\alpha = 30°$ (figure 2.21(c)) dissipation rate increases throughout the metalimnion close to the walls, eventually spreading far into the interior. Spatial distribution of regions with increased ϵ coincides with the spatial distribution of shear squared (not shown), suggesting that this is the consequence of the appearance and distribution of shearing layers due to the higher vertical modes.

The turbulent diffusivity of density K_ρ shows that for the rectangular case (figure 2.21(d)), mixing dominantly occurs above the metalimnion, near the surface and the walls; in this case, solitary-like waves are clearly visible in the isopycnals as short waves locally present throughout the isopycnals in a water column. As inclination angle decreases, additional mixing appears also under the metalimnion, next to the wall by the side where metalimnion widens (figure 2.21(e)). For the lowest angle, mixing is present near walls inside and under the metalimnion at both end-walls. Substantial mixing is present inside the contracted side of metalimnion. Under the widened side, we observe a region with negative $\langle N^2 \rangle$ which indicates overturning events. The reduction of the number and amplitude of solitary-like waves observable in the time series, together with increased mixing near the walls for the nonrectangular cases, indicate the occurrences of solitary-like waves and breaking events at the sloped walls. Based on the classification of breaking events (Aghsaee et al., 2010, Nakayama et al., 2019), the vast majority of the wave breaking events are surging breakers. Plunging breakers are possible only for the gentle slopes $\alpha \leq 45°$ and the solitary-like waves with amplitude larger than $0.1h_1$; such high amplitude waves occur only at the wave cancellation event. Similarly to Ulloa et al. (2019), we found that $K_\rho/\kappa = O(1)$ throughout the interior and $K_\rho/\kappa = O(10^4)$ near the surface. Besides this, we found some mixing $K_\rho/\kappa = O(10^2)$ at the bottom end of metalimnion in the region spreading from the sloped walls, namely the location where most of the mixing processes in the metalimnion occurs.

The substantial difference in the region where mixing occurs under variation of α modifies the time evolution of the density field and produces differences in the interface heights as observed in figure 2.20. Mixing in the upper layer is dominant for steep slopes, which pushes the metalimnion downwards. For moderate slopes, the effect of upper metalimnion mixing due to forcing is weaker, while mixing under metalimnion caused by wave breaking and shear-induced mixing increases, which results in smaller variations of the interface height over time.

2.5.3 Nonresonant response and internal adjustment to resonance, $r_T = 3$

As the forcing period gets larger than the fundamental one, the role of the inclination angle of the end-walls becomes substantially more important. In the interface height time series of figure 2.22(a) on a

non-nodal location A, we can observe that the initial response corresponds to a nonresonant fundamental seiche as previously described for the rectangular case. The fundamental wave remains dominant until the third forcing period, during which its shape degenerates. Upon degeneration, solitary-like waves become dominant for cases with the steep slopes ($\alpha > 45°$), while the system starts to adjust to forcing for moderate slopes ($\alpha \leq 45°$). For the lowest α we observe that a resonant response develops, characterized by resonant amplification of the wave amplitude. Upon degeneration, steep slopes ($\alpha \geq 75°$) behave as described for the rectangular case; high-frequency waves are always present and the main response adjusts to nonresonant, nonlinear, second vertical mode V2H2. Besides this response, multiple fundamental waves form and cancel, thus energizing solitary-like waves. For moderate slopes, ($\alpha \leq 45°$), the system starts to adjust to forcing during the third forcing period and the amount of high-frequency waves decreases. For the lowest angle ($\alpha = 30°$) case, there is a significant amplification in the wave amplitude, indicating that resonant response occurs. The interface for the slope angle $\alpha = 60°$ (green line) shows intermediate behavior: it develops a V2H2 mode which is substantially less energetic than that for steeper slopes; at the same time, its response adjusts to forcing period but less effectively compared to cases with lower angles.

There is a significant deepening of the interface ρ_0 over time, and this deepening is directly related to the slope angle α, as it increases with steepening of the end-walls. This is related to different mixing mechanisms that change the background density over time. In figure 2.22(g, h) we show the final background density profiles and their variation throughout the simulation, respectively, calculated by sorting the density field according to Peltier and Caulfield (2003). The density field was sorted in order to achieve the most stable stratification while considering the actual volume and shape of the domain for different values of α. In the epilimnion and metalimnion, the change of background density due to mixing is greatest for steep slopes. This is due to vigorous corner flow that erodes the metalimnion. In the bottom end of metalimnion, mixing increases with the decrease of α, as processes at the end-walls intensify.

Spectral energy of the interface height time series is shown in figure 2.22(c, d). On the non-nodal position (figure 2.22 (a)) there are two dominant spikes, near forcing frequency f_w and near fundamental frequency f_1, respectively. The amount of energy near f_w decreases with an increase of α, showing a connection between the inclination of the end-walls and efficiency of internal adjustment to forcing. The phase lag near the forcing frequency is high revealing its vertical structure as higher vertical mode, while near f_1 there is no phase lag, indicating the presence of V1H1 mode. On the nodal position for linear waves (figure 2.22 (b)) there are three dominant spikes near super harmonics of forcing f_{w2}, f_{w4}, f_{w6} where $f_{w6} \approx f_2$. High phase lag near f_{w2} and f_{w4} indicates higher vertical modes, while the lack of phase lag near the f_{w6} spike indicates that the V1H2 mode is excited by nonlinear interactions with V1H1. Cases with steep slopes ($\alpha > 45°$) have generally more energetic nonlinear modes, which confirms that their adjustment occurs essentially through nonlinearities.

The wavelet analysis of the interface height shown in the figure 2.22(e) for the resonant case ($\alpha = 30°$), indicates that fundamental and forcing frequency were both energized at the beginning of the forcing. After three forcing periods, the energy contained in the fundamental frequency waves decreases, while the energy in waves with forcing frequency dramatically increases, indicating the occurrence of resonance. After the system adjusts and reaches resonance, the fundamental wave is not re-formed as in the case for the steep slopes. At the nodal location (figure 2.22(f)) the energy of superharmonics f_{w2}, f_{w4} increases later compared to the rectangular case. In fact, the occurrence of these waves is related to energizing of

f_w due to resonance, indicating that they originate by energy transfer via nonlinear interactions. This is significantly different than for the rectangular and steep slopes, where the same frequency wave was excited directly by the forcing.

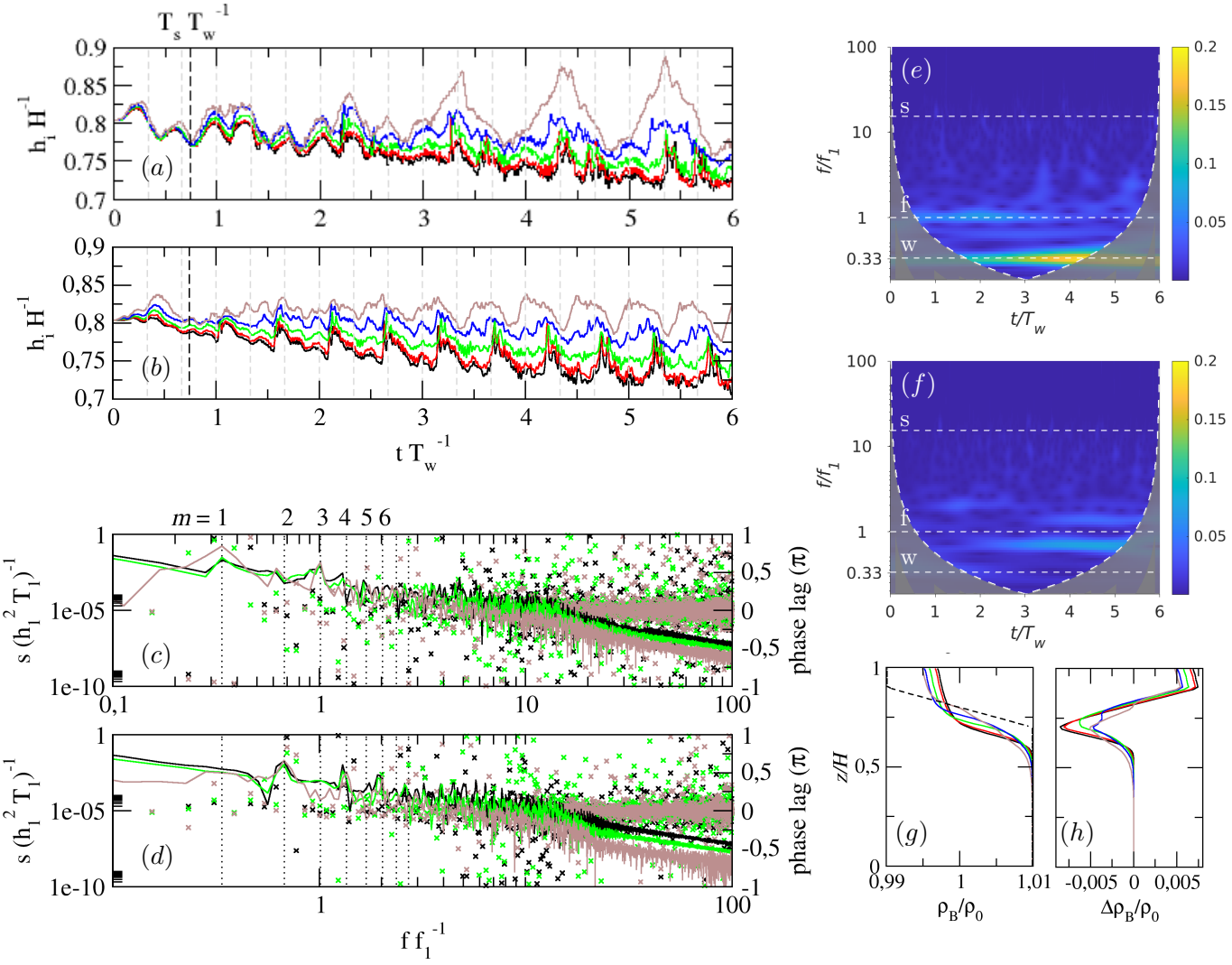

Figure 2.22: Panels (a, b) contain time series of interface height for forcing $r_T = 3$ and different values of α at probes A and B, respectively. Panels (c, d) contain nondimensional spectral energy of interface height (lines) and phase lag among isopycnals (x's) at probes A and B, respectively. Vertical dotted lines represent nondimensional forcing frequency and its m-th superharmonics. Figures (e, f) show wavelets of interface height for $\alpha = 30°$ sampled at probe A and B, respectively. Dashed white horizontal lines denoted with letters indicate: w, forcing frequency f_w; f, fundamental frequency f_1; s, approximate frequency of solitary-like waves $\approx f_s$. Panel (g) shows the vertical profile of the final background density field ρ_B/ρ_0 where dashed line represents the initial background density profile and panel (h) shows the vertical profile of the total change of the background density field $\Delta\rho_B/\rho_0$. Color code: ■$\alpha = 90°$, ■$\alpha = 75°$, ■$\alpha = 60°$, ■$\alpha = 45°$, ■$\alpha = 30°$.

The vertical profiles of averaged velocity components (not shown) behave as for $r_t = 2$ for large inclination angles, whereas substantial differences are evident for small angles where we have observed

internal adjustment to forcing and resonance. Vertical velocity profiles show the second vertical mode as the most dominant and less additional oscillations compared to the other forcing cases. Profiles of $\langle N^2 \rangle$ show the same tendencies as in previous cases.

The spatial distribution of $\langle S^2 \rangle$ (not shown) is very similar to the one for $r_T = 2$ for steep slopes, while for the low ones we observe fewer additional shearing layers in the interior, indicating that V2 may be the highest vertical mode that appears.

Non-dimensional dissipation rate $\epsilon/(u_*^4/\nu)$ is shown in figures 2.23$(a-c)$. As α decreases, the region with dissipation rate deepens. Unlike $r_T = 2$, here we observe less spatial variation among cases with different α. This similarity of the distribution for different inclinations is associated with the occurrence of a single vertical mode V2. For the resonant response (figure 2.23(c)) we observe substantially increased dissipation rate inside the contracted part of the metalimnion, where jet-like flow and high shear occur.

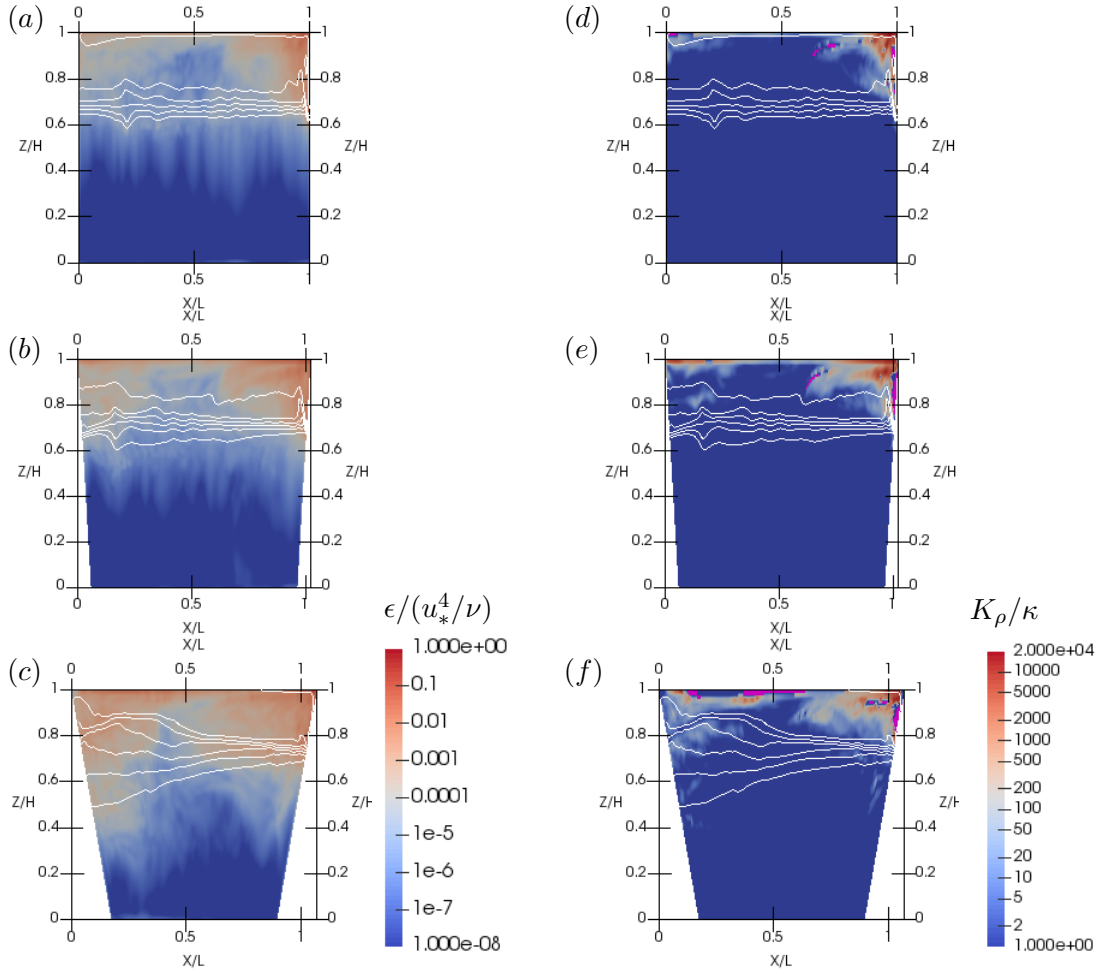

Figure 2.23: Fields of nondimensional turbulent dissipation rate (a, b, c) and turbulent diffusivity of density K_ρ/κ (d, e, f) for $r_T = 3$ at $\varphi = 0.8\pi$: (a, d), $\alpha = 90°$; (b, e), $\alpha = 60°$; (c, f), $\alpha = 30°$. White lines represent isopycnals. In (d, e, f) pink color represents the unstable stratified regions with negative $\langle N^2 \rangle$.

Parametrized diffusivity of density K_ρ is shown in figures 2.23$(d-f)$. We observe the general tendency of having more mixing near the end-walls and increased mixing with a decrease of α, consistently with previous cases. The return jet that turns downwards near the end-wall causes mixing and overturns in

the upper layer. For the steep slopes, this jet causes substantial contraction of the metalimnion next to the wall. For the moderate slopes, the jet meets the metalimnion under a milder angle, and it does not directly cause contraction of the metalimnion. Besides the contraction of the metalimnion, for the rectangular case, contours of the density field depict solitary-like waves with second vertical mode, as described by Ulloa et al. (2020).

2.5.4 Summary

In order to quantify globally turbulent quantities in terms of dissipation rate, we perform spatial (volume-weighted) and temporal (using 0.1π spaced time windows) averages over the last forcing period, which is representative of the fully developed flow. The nondimensional dissipation rate $\langle\epsilon\rangle_{s,t}$ is plotted in figure 2.24(a). There is a clear trend of decrease of total dissipation rate as the end-walls steepen. The dissipation rate is lowest for the resonant V1H1 response ($r_T = 1$) when the transfer of energy from the surface input to waves is the most efficient and more energy goes to additional modes rather than to turbulence. The nonresonant V2H1 response ($r_T = 2$) has nondimensional dissipation rate higher than for $r_T = 1$. The increase comes from the fact that the V2 mode response has two vertical reversals (Münnich et al., 1992) which increase shear. The relatively constant difference between $r_T = 1$ and $r_T = 2$ indicates that the mechanisms that lead to a decrease of dissipation rate for steeper slopes remain the same as internal wave dynamics change from the first to the second vertical mode. The largest forcing period, $r_T = 3$, deviates from the other two, which is mostly due to the dependence of the wave response on α. For the resonant V2H1 response ($\alpha = 30^\circ$) we see a substantial increase of the dissipation rate; this can be related to increased dissipation rate in the interior due to the development of a narrow jet. For intermediate angles, the dissipation rate is very close to the one for nonresonant V2H1 response ($r_T = 2$), but it decreases faster as the end-walls steepen.

In figure 2.24(b) we show the rate of change of the background potential energy over the duration of the simulations made nondimensional with $\rho_0 u_*^4/\nu$. In order to find the minimum background potential energy P_B, we calculate background density $\rho_B(z)$ by sorting the density field according to Peltier and Caulfield (2003) and average it horizontally. The rate of change of the background potential energy is mainly due to mixing (M) and, to some extent, to molecular diffusion processes (D), which are negligible compared to the former.

$$\frac{\mathrm{d}P_B}{\mathrm{d}t} = \frac{\langle g(\rho_{B,final} - \rho_{B,init})z\rangle_z}{6T_w} = M + D \tag{2.10}$$

For cases $r_T = 1, 2$ where the same wave response is dominant over the variation of α, we observe that the highest amount of mixing is for cases with gentle slopes, which can be associated with turbulent activity at the sloped walls. For steep slopes, we observe a trend in weak increase of mixing as slopes steepen, which can be associated with upper layer mixing due to downward jet that causes vigorous corner flow. The scenario is different for $r_T = 3$. In this case, we observe that most mixing occurs for the steep slopes, characterized by nonlinear V2 response. Mixing decreases as this response gets weaker for the cases with lower α and increases again for $\alpha = 30^\circ$ when resonant V2 response occurs.

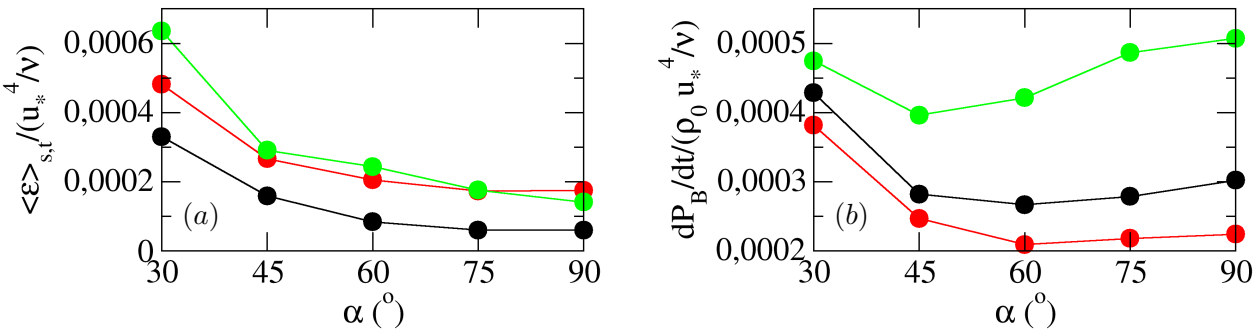

Figure 2.24: Panel (a), space-time averaged nondimensional dissipation rate $\langle\epsilon\rangle_{s,t}$ against inclination angle of the end-walls α. Panel (b), the nondimensional change of the background potential energy over the entire simulation $t = 6T_w$. Color code: ■$r_T = 1$; ■$r_T = 2$; ■$r_T = 3$.

We observe that here the lowest amount of mixing occurs for the linear nonresonant V2 response $r_T = 2$, while the longest forcing period $r_T = 3$ exhibits the highest amount of mixing for both resonant linear V2 response and nonlinear V2 response.

We can conclude that resonant responses introduce more mixing in the system, with V2 response being more effective on mixing than V1. This because of the multilayer structure of the flows characterized by higher shear. We find that a large amount of mixing is related to nonlinear V2 response. We also highlight that the nonlinear V2 response is the dominant wave response and its period is different than the forcing one.

Overall, we can depict the following scenario, upon definition of the state of the periodically forced system as stable or unstable. If the system responds with a wave that absorbs most of the energy input, and this state persists for several forcing periods, the system is in a stable state. On the other hand, if energy input by forcing feeds two or more highly energetic waves that are in competition among them and the state of the wave field changes from one forcing period to another, the system is in an unstable state. When the periodically forced system is close to a stable state, variations of the inclination from gentle to steep slopes do not play an important role in driving the kind of response. Namely, the system soon adjusts to the closest stable state and there it remains. In these cases, (namely $r_T = 1, 2$), the general response remains the same, while the amount of solitary-like waves and near boundary mixing vary with the variation of inclination. As time goes on, boundary mixing can have different effects on the wave field; among the others, the deepening of the metalimnion, which is characteristic for basins with gentle angles; for $r_T = 1$ it leads to escape from V1H1 resonance while for $r_T = 2$ it leads to increase of the amplitude of the V2H1 mode.

When a periodically forced system is far from a stable state, the variation of inclination plays a crucial role in the basin response. For $r_T = 3$ we saw how the transition from gentle to steep slopes moves the response from linear to nonlinear waves. We note that the nonlinear response that we obtain is unstable, as linear waves (in terms of fundamental V1H1) continue to form throughout the duration of numerical experiments. If periodic forcing ceases, these waves would remain present for a while as there is no wave cancellation.

2.6 Concluding remarks

In the present Chapter, we investigated the response of a periodically forced stratified basin in terms of excitation of internal modes and mixing. We discuss energy transfer in the wave field since the initial phase of excitation and, specifically, the transfer of energy to the nonlinear waves and their feedback on the dominant basin wave response. The analysis was carried out numerically, using Large Eddy Simulation, at a laboratory scale. The model was validated against two different laboratory experiments. We set a three-layer stratification, typical of real-scale basins, and studied the system under variation of the forcing frequency (the frequency of the forcing wind stress) and variation of the inclination of the end-walls of the basin. We obtained different basin responses, classified in table 2.5 according to wave modes and occurrence of resonance.

Resonant V1H1 response: For forcing period near fundamental period, resonant V1H1 response occurs for all end-walls inclinations analyzed. The resonant wave gradually energizes higher horizontal modes. There are slight differences among cases, related to the variation of the angle of the end-walls α. Generally, we found that decreasing the angles of the side leads to increased mixing near the sloped walls. This causes a more rapid transition from resonance and changes in the level of stratification in favor of excitation of higher vertical modes superimposed over the main wave response.

Nonresonant V2H1 response: For forcing period with $r_T = 2$ a particular situation develops. At the beginning, the fundamental response switches on, and after one forcing period, this response is out of phase with the forcing, causing cancellation of this wave. During that event, energy gets transferred from the fundamental mode into a nonlinear surge that quickly steepens and energizes the high-frequency solitary-like waves. After the destruction of the fundamental V1H1 response, a non-resonant V2H1 response with forcing frequency develops. As inclination angle decreases and the metalimnion widens, V2H1 becomes more energetic, yet in absence of a resonant response.

r_T	Main response	$\alpha[^\circ]$
1	resonant V1H1	$30, 45, 60, ..., 90$
2	nonresonant V2H1	$30, 45, 60, ..., 90$
	nonresonant V2H2	$60, 75, 90$
3	nonresonant V2H1	45
	resonant V2H1	30

Table 2.5: Dominant response with respect to r_T and α.

Nonresonant nonlinear V2H2: The system responds to $r_T = 3$ forcing with a superposition of fundamental wave response and waves with forcing frequency. For steep slopes, cancellation of the fundamental wave occurs several times, each time this wave forms again, as the system fails to adjust to the forcing. Instead, upon the first cancellation event, nonlinear wave V2H2 develops with twice the forcing frequency and remains the most energetic non-interrupted wave throughout the simulation. The nonlinear V2 wave response is specific for its own ability to produce V2 solitary-like waves, as recently investigated and described by Ulloa et al. (2020).. Nevertheless, the system is not stable in this state, as a linear fundamental wave, with an amount of energy similar to that of the V2H2 wave, continues to form and gets canceled, unlike the situation observed with V2H1, where this wave does not reoccur once the system adjusts to forcing.

The inclination of the end-walls also plays an important role. With the decrease of the angle of the end-walls the spatial distribution of mixing and dissipation rate changes dramatically. As α decreases, more mixing occurs at the intersection of the metalimnion and boundaries. This corresponds to the well known behavior of seiche interaction with the boundaries (Lorke et al., 2005) and wave breaking at the

slopes (Michallet and Ivey, 1999). The mixed fluid is subsequently transported towards the interior which leads to the thickening of the metalimnion (Wain and Rehmann, 2010). The thicker metalimnion enables the formation of the higher vertical modes that enhance the transport of fluid away from the wall (Wain et al., 2013) and creates shearing layers in the interior that can produce shear instabilities in the regions where stratification is weak.

As the inclination angle decreases, the system gains the ability to adjust to the forcing. For $\alpha = 60^\circ$ the main response is still characterized by nonlinear V2H2, but V2H1 with the forcing frequency appears more energetic than for steeper slopes, yet its energy decreases with time. For even lower inclination angle $\alpha = 45^\circ$, the system nonresonantly adjusts to the forcing frequency via V2H1, while the fundamental V1H1 is still present. For the lowest tested angle $\alpha = 30^\circ$, the system develops a resonant V2H1 response and the fundamental wave is not re-energized. We conclude that for a forcing period that is long enough compared to the fundamental one, $r_T = 3$ in this case, the fundamental wave will occur as a response even when the system adjusts to forcing via higher vertical modes, except in the case of resonant adjustment.

We recognize that due to low Reynolds and high Richardson numbers that are commonly used at the laboratory scales, our work likely underestimates mixing in the interior and near the bottom boundary layer compared to the real scales. We also acknowledge that the ratio of vertical to horizontal dimension is exaggerated compared to the lake dimensions and that the uniform density used in the hypolimnion and epilimnion is an approximation of a weak stratification commonly found in nature. Nevertheless, we find that the mechanisms that we have observed, such as internal adjustment, wave destruction, the influence of higher vertical mode on the spatial distribution of the turbulent fields, and dependence of the obtained response on the domain shape are relevant for the analysis of field and laboratory data. We hope to motivate more laboratory and numerical research on the internal adjustment to forcing.

Chapter 3

Stratified basin response to the periodic forcing: Effects of rotation

We are interested in investigating the influence of the periodic forcing on the internal waves in the rotational system. This situation is common in nature when lakes are exposed to diurnal winds. First, we investigate the conditions of the Alpine-like lakes. In the table 3.1 we show the main scales and parameters estimated for a number of Alpine lakes using the stratification data from Magni et al. (2008). Lakes with lengths under 5 km generally have high Burger number thus rotational effects are negligible (Antenucci, 2009). Besides, they have shorter T_1 (large r_T) which makes them susceptible to developing the response in the terms of second or higher vertical mode (LaZerte, 1980, Münnich et al., 1992). As lakes get larger, Burger number falls between 0.2 and 1, while fundamental period T_1 grows from 0.5 to 2 days, which corresponds to r_T between 2 and 0.5. For the presented Alpine lakes, the inertial period T_i is about 0.7 days. We use the parameters that correspond to the broad range of lake sizes in our simulations setup, from the large ones where rotational effects are well expected, to the small ones where they are usually neglected.

This chapter is organized in the following way: in Section 3.1 we define the mathematical model, in Sections 3.2 and 3.2 we show the results of model validation, in Section 3.4 we show and discuss our results, in Section 3.5 we give overview of the results and the concluding remarks.

The part of the research described in this chapter is going to be submitted as an independent paper.

3.1 Mathematical model

We solve the set of filtered three-dimensional Navier-Stokes equations under the Boussinesq approximation for the density field in a rotating frame of reference that is expressed through the Coriolis force:

$$\frac{\partial \overline{u}_j}{\partial x_j} = 0 \tag{3.1}$$

$$\frac{\partial \overline{u}_i}{\partial t} + \frac{\partial}{\partial x_j}(\overline{u}_i \overline{u}_j) = -\frac{\partial \overline{p}}{\partial x_i} + g_i \frac{\rho}{\rho_0} + \frac{\partial}{\partial x_j}\left[\nu_{eff}\left(\frac{\partial \overline{u}_i}{\partial x_j} + \frac{\partial \overline{u}_j}{\partial x_i}\right)\right] - 2\epsilon_{lmi}\Omega_l \overline{u}_m \tag{3.2}$$

$$\frac{\partial \overline{\rho}}{\partial t} + \frac{\partial}{\partial x_j}(\overline{\rho u}_j) = \frac{\partial}{\partial x_k}\left(\kappa_{eff}\frac{\partial \overline{\rho}}{\partial x_k}\right) \tag{3.3}$$

Lake	L(km)	S	T_1(days)	T_i(days)
Ledro	3	3.36	0.13	0.70
Caldonazzo	4	2.48	0.18	0.71
Bohinj	4	1.92	0.23	0.70
Varese	8	0.98	0.45	0.70
LakeOssiach	10	0.81	0.54	0.69
MillstaterSe	11	0.93	0.47	0.69
Annecy	14	0.74	0.60	0.70
Worthersee	16	0.63	0.70	0.69
Bourget	18	0.70	0.64	0.70
Iseo	20	0.74	0.60	0.70
Como	45	0.32	1.40	0.70
Maggiore	50	0.30	1.47	0.69
Garda	51	0.29	1.53	0.70
Geneva	70	0.20	2.22	0.69

Table 3.1: Size and nondimensional parameters for some Alpine lakes.

In eqs. (3.1),(3.2),(3.3), the overbar denotes a filtering operation, u_i is the velocity component along the x_i direction (hereafter we use x_1, x_2, x_3 and x, y, z respectively for along wind, transverse and vertical upward directions), p is pressure divided by the bulk density ρ_0, $g \equiv (0, 0, -g)$ is the gravity acceleration vector, ϵ denotes the Levi-Civita symbol, Ω is the vector of the frame's angular velocity, $\nu_{eff} = \nu + \nu_{SGS}$ is the sum of the kinematic viscosity ν and the sub-grid-scale (SGS) turbulent viscosity ν_{SGS}, ρ is fluid density, and $\kappa_{eff} = \nu/Pr + \nu_{SGS}/Pr_{SGS}$ is sum of molecular and SGS thermal diffusivity, Pr and Pr_{SGS} being the molecular and SGS Prandtl number respectively.

The turbulence modeling and numerical setup are the same as in the case without the rotation described in Section 2.1.

Initially, we consider the fluid at rest with a piecewise linear density stratification as initial condition as described with (2.6) where upper and lower layer with thicknesses h_1, h_2 have constant densities ρ_1, ρ_2 and middle layer with thickness Δh has a linear transition from ρ_1 to ρ_2 (see figure 3.1).

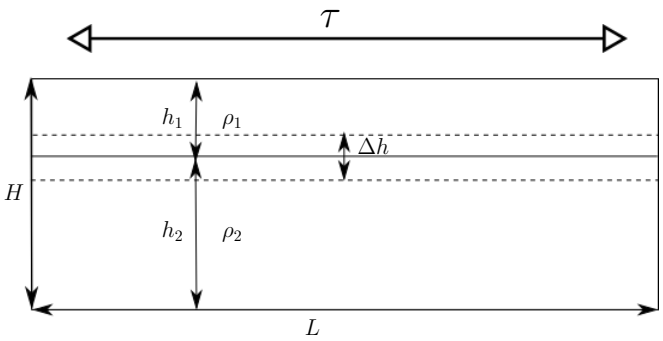

Figure 3.1: Sketch of the simulation setup in the xz plane.

Given that the estimated surface movement is very small (Boegman, 2009), we approximate the surface as a rigid lid and apply the periodic surface shear stress with period T_w as described with (2.7). The horizontal stress components are energized with fluctuations of 20% and 1% of the mean value of τ in x and y directions respectively. From the distances $0.1L$, $0.1B$ from the sides in the x and y direction, respectfully, applied stress decreases linearly and reaches zero at the end-walls and side-walls. The effects of rotation change the internal waves from two

to three-dimensional, making periodic boundary conditions unsuitable. For this reason, we use no-slip condition in the y direction instead of periodic condition used in Chapter 2. The no-slip condition for velocity is applied at the five solid walls, end-walls, side-walls and bottom. The boundary condition for the density field is zero gradient for surface, bottom, and walls (no-flux conditions). At the five solid walls, we use no-slip conditions for velocity.

The choice of time step $\Delta t = 0.01$s is justified in Section 2.1, as well as the notation for averaged quantities $\langle\theta\rangle$ and fluctuations θ''.

3.2 Ekman surface spiral

The solver without the rotation is validated on the two sets of experiments as described in 2.2, and proven to be able to resolve internal wave field and surface stress adequately. In order to validate our implementation of the rotational effects, we reproduced Ekman's surface spiral. The problem is described as fluid at rest with surface shear stress acting at the free surface. The analytical steady-state solution of this problem is:

$$u = \frac{\tau}{\sqrt{f\nu}} e^{z/\delta} \cos\left(-\frac{z}{\delta} + \frac{\pi}{4}\right),\ v = \frac{\tau}{\sqrt{f\nu}} e^{z/\delta} \sin\left(-\frac{z}{\delta} + \frac{\pi}{4}\right) \tag{3.4}$$

where u is the horizontal velocity component in the direction of the applied surface stress, v is stress-normal horizontal velocity component, τ is a kinematic surface shear stress, $\delta = \sqrt{2\nu/f}$ is thickness of the Ekman layer, $f = 2\Omega \sin\theta$ is Coriolis parameter and θ is latitude. The z-axis is directed vertically upward, such that the free surface is found at $z = 0$.

In our numerical setup, at the free surface, we apply the surface shear stress in the form of (2.7), while the lateral sides of the domain have periodic boundary conditions and bottom (referring to the bottom of the domain, not fluid) has the velocity conditions in form:

$$\frac{\partial u}{\partial z} = 0,\ \frac{\partial v}{\partial z} = 0,\ w = 0,\ z = -D \tag{3.5}$$

where D is depth of the domain. The free shear condition is used instead of the no-slip to prevent the formation of another Ekman spiral at the bottom of the domain. The density field is uniform and density has a fixed value at the top and bottom. The domain has size $(5 \times 5 \times 50)\text{m}^3$ and is discretized with $(5 \times 5 \times 60) = 1500$ cells with uniform distribution in x, y directions and expansion ratio of 0.2 in z direction.

We chose the set of variables ν, $\Omega = (0, 0, 2f)$ and τ such that $\delta = \sqrt{2\nu/f} = 1$ and $u_E = \tau/\sqrt{f\nu} = 1$. Given that we are using an unsteady solver (PIMPLE) the obtained solution is not steady, yet it slowly oscillates around the steady solution with a very long oscillation period about ≈ 33000s. If we average the fields in horizontal planes and over one period

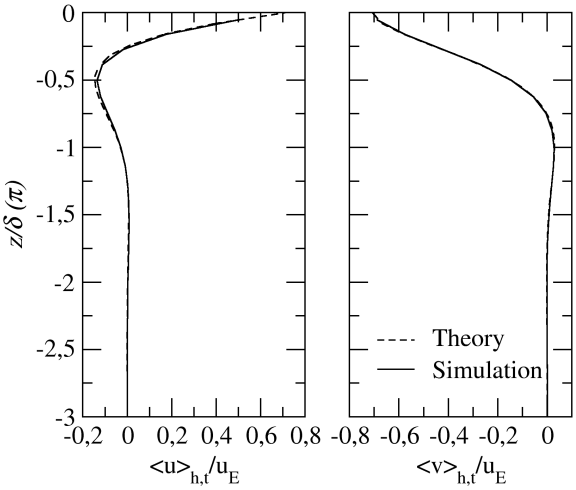

Figure 3.2: The vertical distribution of the horizontal velocity components. Solid lines represent temporally and horizontally averaged horizontal velocity components u and v. while dashed lines represent the analytical solution.

during which the solution oscillates, we obtain an excellent comparison between the simulated vertical profiles of u and v and the analytical profiles (equation (3.4)), as shown in figure 3.2. Given that our numerical simulation reproduces the analytical solution well, we conclude that our solver can be used to simulate the effects of rotation.

3.3 Grid validation

We conducted a grid sensitivity test in order to assure numerical accuracy of the results. In figure 3.3 we show horizontally averaged quantities obtained with three different grids for the case of oscillating surface shear stress at several phases of the forcing cycle. The initial and boundary condition of the grid tests are described in Section 3.1. Hereafter angle brackets denote averaged quantity, where phase averaging is considered by default and otherwise it is denoted by a subscript; a double prime denotes a fluctuating quantity.

With the introduction of the rotation into the system, the unphysical oscillations appear in the vertical velocity component in the vertically neighboring cells near the forced surface. We reduced these effects by refining the grid near the surface with stretching. We additionally apply filtering operation for these oscillations in the post processing. The grid was constructed using uniform and equal spacing in x and y directions, and cell expansion in z direction with the expansion ratio, that is the ratio of the surface cells to bottom cells, $\Delta z_s/\Delta z_b = 0.57$, where subscripts denote: s, surface and b, bottom cells. In this way, the maximum cell aspect ratio is found near the surface and it is close to 4.

Basic grid is the one used in our simulations $(n_x \times n_x \times n_z) = (300 \times 60 \times 90)$; we tested a grid that is 25% coarser in

$(n_x \times n_x \times n_z)$	n_{tot}	$\Delta x^+, \Delta y^+$	Δz_s^+	Δz_b^+
$(300 \times 60 \times 90)$	1,620,000	37.2	9.2	16.2
$(225 \times 45 \times 67)$	678,375	49.6	12.4	21.7
$(450 \times 90 \times 135)$	5,467,500	24.8	6.1	10.8

Table 3.2: Resolution of the grids used for testing.

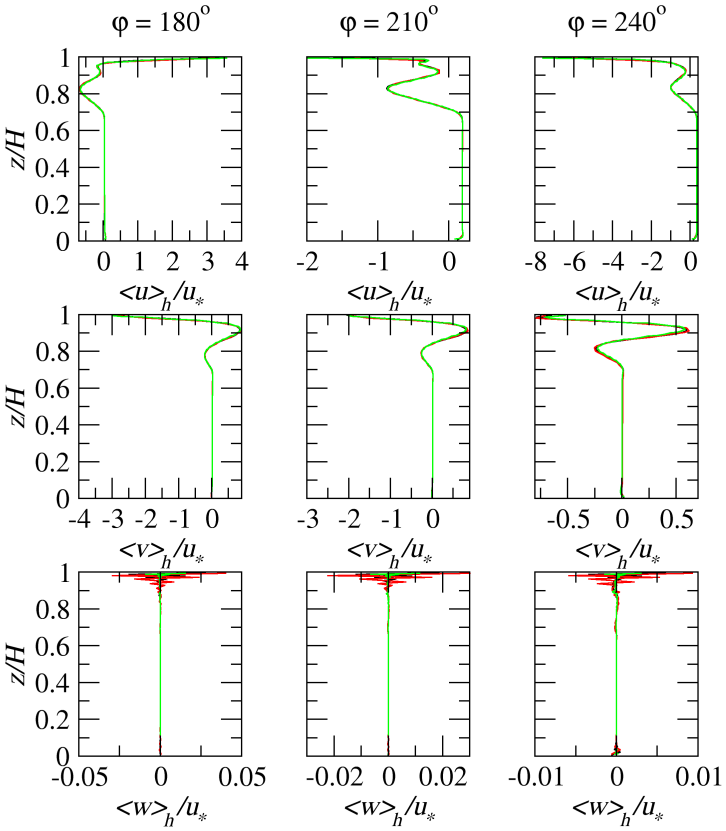

Figure 3.3: The vertical profiles of the horizontally averaged velocity components obtained for the resonant forcing $r_T = 1$ and rotation $S = 1$ for the three grids. The φ denote the phase of a forcing period. Color code: —— basic grid; —— coarse grid; —— fine grid.

all directions $(n_x \times n_x \times n_z) = (225 \times 45 \times 67)$; and the one that is 50% finer in all directions $(n_x \times n_x \times n_z) = (450 \times 90 \times 135)$. Grid resolution expressed in wall units $\Delta x_i^+ = \Delta x_i u_*/\nu$, as well as total number of cells per grid is shown in table 3.2. We note that our grid is not uniform in the vertical direction, therefore we express the dimension of smallest, near surface cells (Δz_s^+) and largest, near bottom cells (Δz_b^+). Based on the comparison of the vertical profiles shown in figure 2.5 we conclude that we have reached grid convergence. We obtained an excellent match in horizontal velocity components. In the near-surface region, coarsening of the grid increases the numerical oscillations of the vertical profile of vertical velocity. These oscillations reduce as the grid near the surface is refined. We minimize these oscillations by our grid choice. The remaining oscillations are small and confined in the near-surface region and they do not alter the physics of the flow, therefore do not give an important contribution to the physics we are studying. In our later work, we filter these oscillations in the post-processing.

3.4 Results

We conducted three sets of simulations with respect to the ratio of forcing to fundamental period $r_T = 0.5, 1, 2$. In each set, we varied Burger number as $S = 1, 2, 4, \infty$, while Wedderburn number was kept constant, $W = 5$, which corresponds to weak to moderate forcing. These numbers are chosen to mimic the conditions of lakes in the Alpine region (see table 3.1). We set the angle $\theta = 45°$ to mimic the conditions at the mid-latitudes and we orient the domain such that x-axis is pointing towards the axis of rotation (towards north), as most lakes in Northern Italy (Maggiore, Garda, etc) are approximately aligned in the south-north direction. The variation of S is achieved through the variation of angular velocity Ω, which consequentially changes the inertial period $T_i = 2\pi/f$. The change of ratio T_i/T_w corresponds to variation of latitude while considering diurnal forcing, where $T_i/T_w \approx 1$ corresponds to the diurnal forcing near 30° latitude.

L (m)	B (m)	h_1 (cm)	h_2 (cm)	Δh (cm)	ρ_1 (kg/m^3)	ρ_2 (kg/m^3)
2	0.4	4	16	4	1000	1020
	u_*^2 (m^2/s^2)	W	T_1(s)	T_s(s)	T_w(s)	
	3.11×10^{-5}	5	50.73	112.74	25,50,100	

Table 3.3: Main parameters of the numerical experiment.

S	T_i	T_{PW} (s)	T_S (s)	
0.3	23.91	21.55	312.10	
0.6	47.82	34.47	441.38	
1	79.69	42.20	569.82	
2	159.38	47.49	805.85	
4	318.77	49.15	1139.64	
∞	∞	-	-	-

Table 3.4: Case setup. Time scale T_S represents a spin-up time for the linearly stratified media (van Heijst et al., 1990).

The parameters that vary with the variation of S are shown in table 3.4. T_{PW} represents the period

of the basin scale internal Poincaré wave for the rectangular basin calculated according to Bouffard and Wüest (2018) as:

$$\frac{1}{T_{PW}^2} = \frac{1}{T_i^2} + \frac{1+r^2}{T_1^2} \tag{3.6}$$

where $r = B/L$ is basin aspect ratio at the thermocline depth. Before the application of the periodic surface shear stress, we let the system adjust to rotation during the spin-up time (Greenspan and Howard, 1963, Linden and Van Heijst, 1984, van Heijst et al., 1990). We use the time scale for the two-layer stratification $T_S = h_2/\sqrt{\nu f}$ (Linden and Van Heijst, 1984). T_S is an appropriate time scale when $T_W/T_S << 1$, where $T_W = 0.5L/(g'h_2)$ is the time during which information propagates from the boundary to the center of the tank. This condition is satisfied in all tested cases. The initial spin-up does not alter the density distribution. The simulations are run for 11 forcing periods.

We use several approaches to investigate the internal wave field. We sample the vertical profiles of density and velocity at several locations as shown in figure 3.4 where A and D are near-wall locations, B and C are internal locations and C and D are nodal locations for linear waves that oscillate along the length of the basin L. We discuss the results with a focus on spectral analysis of the time series (interface spectra, rotary spectra, coherence phase, wavelets), an inspection of the instantaneous and phase averaged fields as well as turbulent quantities.

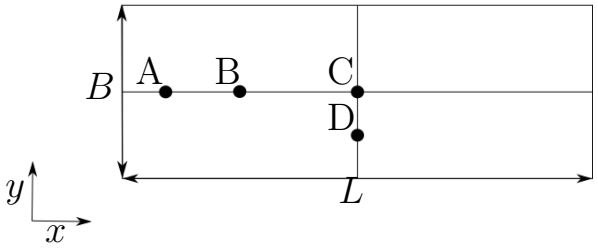

Figure 3.4: A sketch with locations where vertical profiles of density and velocity are sampled. The sampling points in (x, y) plane have locations: A, $(0.25B, 0.5B)$; B, $(0.25L, 0.5B)$; C, $(0.5L, 0.5B)$; D, $(0.5L, 0.25B)$.

We calculate the spectra of the interface height time series and rotary spectra of the horizontal velocity components sampled at the interface. The rotary spectra discern between the wave with cyclonic and anticyclonic rotating currents. To gain insight into the vertical structure of the waves, we calculate phase lag between the isopycnals $\rho_0 \pm 0.25\Delta\rho$. The existence of the phase lag indicates the occurrence of the wave with higher vertical mode, without giving the information on the modal structure.

In order to calculate turbulent quantities with respect to their spatial distribution we have to compute averages and fluctuations of the fields. This is a challenge in the three-dimensional unsteady flow. We decide to exploit the periodicity of the flow due to oscillating forcing conditions and we conduct phase averaging with respect to the forcing period. This kind of phase averaging is susceptible to the influence of waves with different periods, as well as mixing that happens over time. Both effects can cause higher fluctuations, which is why we consider the quantities herein calculated as more qualitative more than quantitative. We focus on their spatial distribution and comparison among the different cases. We ran the simulations for a total of 11 forcing periods and we use the last eight periods to calculate the phase averaged quantities.

3.4.1 Forcing period $r_T = 0.5$

The interface height time series sampled at locations shown in figure 3.4 for the case $r_T = 0.5$, when the forcing period is shorter than the fundamental one, are shown in figure 3.5. At the near-wall location

A, the initial response seems to have the forcing periodicity. This response degenerates at the beginning of the second forcing period and produces oscillations with the fundamental period. For low Burger numbers $S < 1$ the fundamental wave soon degenerates into higher frequency waves. At location B, for high S we observe waves with forcing periodicity which seems superimposed on the waves with a longer period. Here, we note that the amount and amplitude of the high-frequency waves are increased for the cases with strong rotation. At the central locations C and D, at low S dominant waves have about a half-forcing period, and their amplitude noticeably increases as rotation is getting stronger, especially for $S \leq 1$. For strong rotation, the response is dominated by the energetic high-frequency waves.

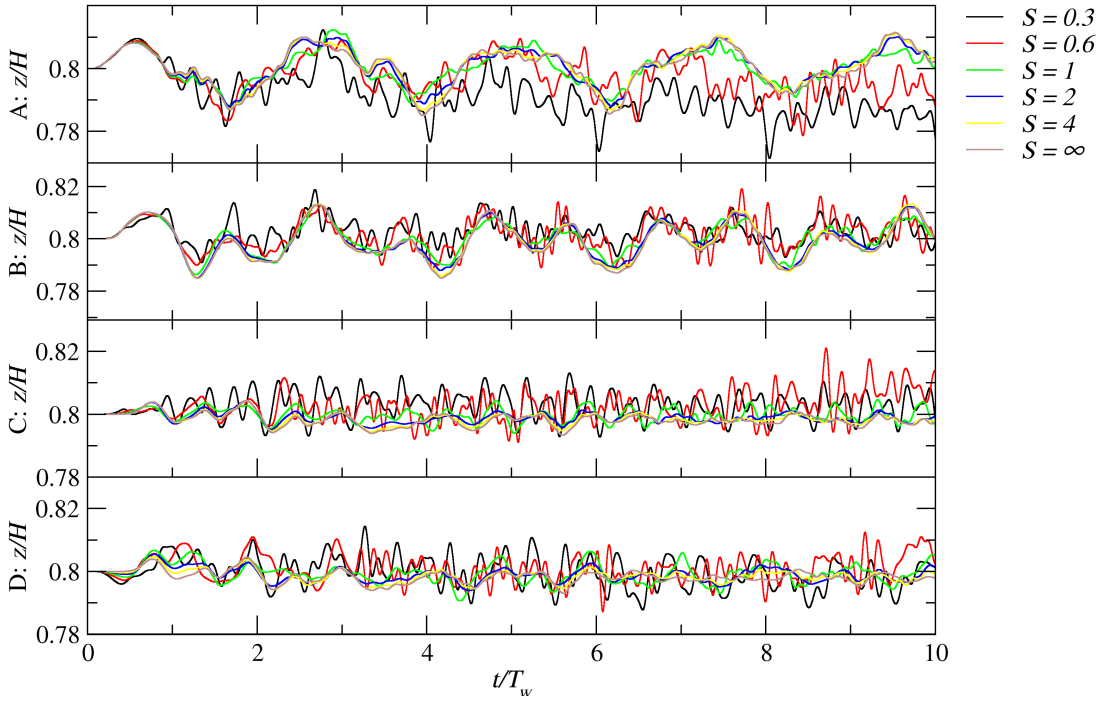

Figure 3.5: Time series of the interface displacement sampled at the four locations, defined in figure 3.4, for the cases with different Burger number S.

We inspect the wave field by conducting spectral analysis. For this case of r_T, we ran the simulations for the additional 5 forcing periods (16 in total) in order to resolve wave properties at low frequencies. In figure 3.6 we show the spectra and phase lag for some Burger numbers sampled at the four locations. The figure also denotes forcing frequency f_w, inertial frequency f_i and frequency of the Poincaré wave f_{PW}.

At the near-wall location A, interface wave response is the strongest for the fundamental wave, but the energy of this wave decreases for cases $S < 1$, where the fundamental frequency is subinertial ($f_1 < f_i$); the fundamental wave f_1 displays weakly cyclonic rotating currents in all cases with rotation; phase lag at f_1 is low. The wave response of interface ρ_0 near the forcing frequency f_w decreases as rotation gets stronger, the anticyclonic rotation develops and currents at f_w become more energetic, as long as forcing frequency is superinertial ($f_w > f_i$). In case $S = 0.3$ where f_w is weakly subinertial, the anticyclonic

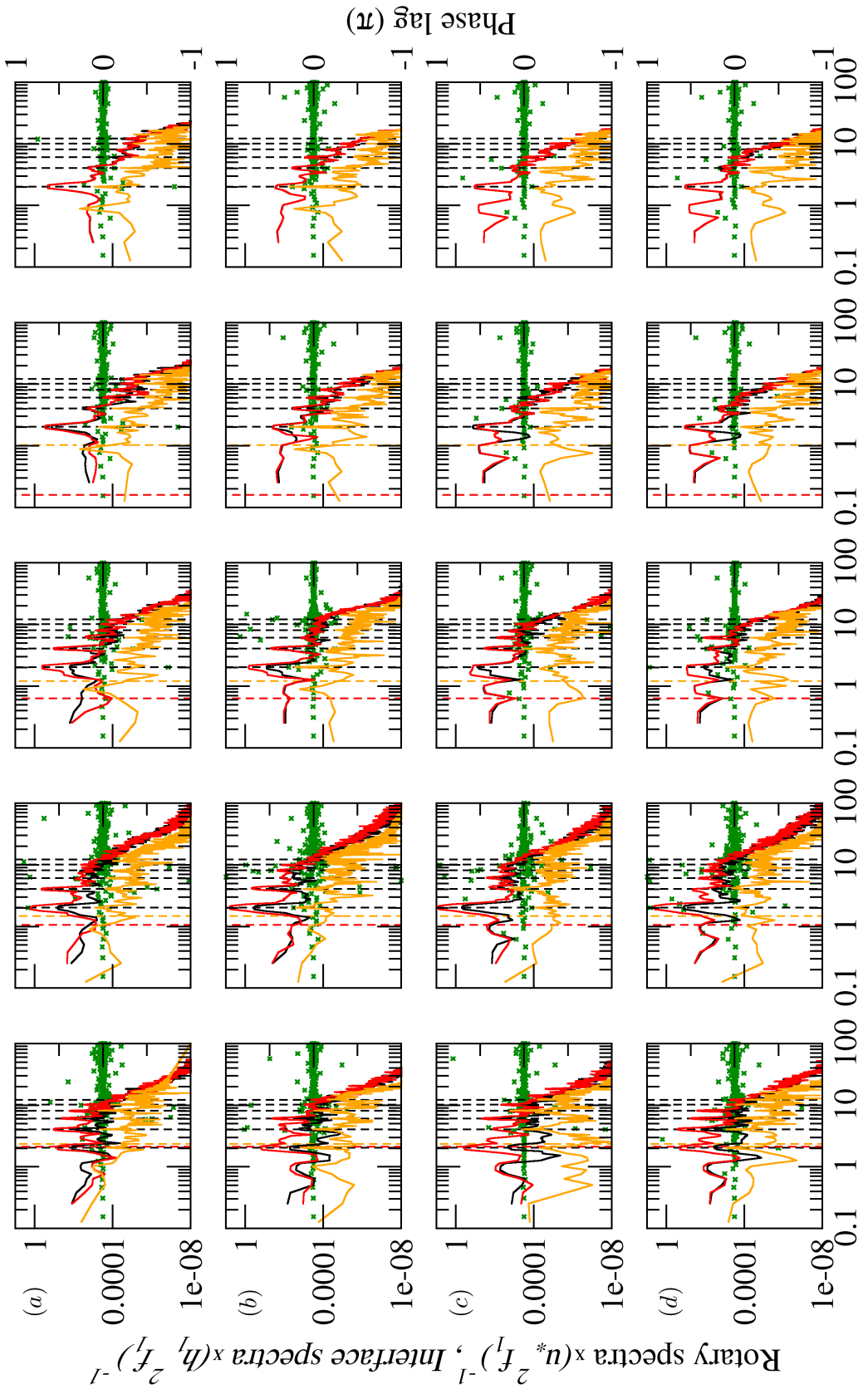

Figure 3.6: Rotary spectra of horizontal velocity components, interface height spectra and phase lag for Burger numbers denoted over columns. The sampling locations are grouped in rows as: (*a*), A; (*b*), B; (*c*), C; (*d*), D. The notation is following: —— cyclonic rotation; —— anticyclonic rotation; —— interface spectra; x phase lag. Dashed vertical lines denote: - - - forcing frequency f_w and its superharmonics wm; - - - inertial frequency. The fundamental frequency f_1 and its superharmonics f_n can be read directly from the x-axis that is scaled accordingly.

currents are substantially less energetic, which is unusual considering that $f_w \approx f_i \approx f_{PW}$ which opens a possibility for resonant excitation of Poincaré wave with frequency f_{PW}. On the contrary, energy is transferred more efficiently to the waves whose frequency is more distant from f_i. As a result, for $S = 0.3$ where f_w is very close to f_i and f_{PW}, but $f_w < f_i$, Poincaré wave forms but not very energetic, in fact, it is more energetic at f_{w2}. For other rotational cases, $f_w < f_i$, thus the formation of Poincaré wave is permitted at f_w and these waves are more energetic, even though there is a greater difference between f_w and f_{PW} compared to $S = 0.3$ case. The superinertial f_w waves are characterized by high phase lag, which indicates that this response belongs to the wave with higher vertical mode, while subinertial f_w has a low phase lag, indicating V1 response. A number of higher superharmonics of forcing frequency f_{wm} and fundamental frequency f_1 can be observed. For strong rotation ($S < 1$), f_3 develops as moderately energetic Poincaré wave; while f_4 V1 wave is superimposed on f_{w2} with higher vertical structure. In cases with a high phase lag f_{w2} prevails (as a superharmonic of f_w that is higher vertical mode), while for low phase lag f_4 is dominant. At the frequency $f_{w3} \approx f_6$, for strong rotation these waves are energetic and a high phase lag indicates that they are f_w superharmonics, while for weak rotation these waves are very weakly energetic and the absence of the phase lag indicates f_6 response. Only for subinertial forcing, for the $S = 0.3$, the phase lag is absent at near f_w and f_{w2} peaks, indicating Poincaré V1 response.

At location B, for the weakly rotational cases, the interfacial wave with f_1 and f_w are almost equally energetic, while the energy of f_1 decreases for strong rotation, when it is subinertial; the phase lag is relatively low ($\approx 0.25\pi$ at f_w) at both frequencies. The f_w wave has anticyclonically rotating currents for all cases, while f_1 is generally nonrotational. The f_4 wave appears with V1 character for high Burger numbers and as higher vertical mode wave (f_{w2}) for $S \leq 1$.

The central location C is an antinodal location for f_2, f_4 waves that have peaks in interfacial oscillations. Rotary spectra reveals nonrotational structure at f_1 and anticyclonic rotation at f_w. In the nonrotating case, there is an energy cascade of the interface spectra waves, where higher modes (f_4) have lesser energy than the lower modes (f_2). As rotation effects intensify, the energy in the higher modes increases and in a lower decrease. In case $S = 0.3$ there is an increase of energy with modes for f_2, f_4 and f_8. This distribution can be explained with the backward energy transfer as described by de la Fuente et al. (2008) where Poincaré waves do not steepen, but the energy of higher modes is periodically transferred back to the parent wave. Due to this mechanism, Poincaré waves rarely transfer their energy to the high-frequencies and excite solitary-like waves. Nevertheless, we do observe the increase of energy in the region of the high-frequency waves as the rotation intensifies which is in accordance with findings of Ulloa et al. (2014).

At location D, the interfacial wave at frequency f_1 is weakest and exhibits higher vertical mode behavior through weakly increased phase lag with an exception for $S = 0.3$. The absence of fundamental interfacial wave at the basin center is expected due to its linear nature, where the central location of the basin is the nodal one. In Section 2.4 we demonstrated that the basin with a wide metalimnion layer develops a particular vertical mode response near f_1 that is reflected in weak spreading and contracting of metalimnion at the central part of the basin. The interface wave response at f_w, as well as its phase lag and anticyclonic rotation, increase as rotation strengthens. For subinertial forcing $S = 0.3$ interface response is more energetic, while currents are less energetic than for the superinertial forcing ($S = 0.6$). This indicates that the observed f_w waves have different PE/KE distribution, where increased energetic of currents (KE) with respect to interface waves (PE) correspond to typical Poincaré wave occurrence. The dependence of the f_w wave to the rotational characteristics, together with the sampling location that is offset to the lateral sides, and comparison with interface spectra at location C, indicates that differences

come from the transversal nature of the observed wave. We note that except for superharmonics of forcing f_{wm}, anticyclonic currents also appear at f_3, given that for the strong rotation f_1 is subinertial, and therefore cannot represent Poincaré wave, we assume that this wave is excited through triad interaction among f_w and f_1 or f_w and f_{w2} because both pairs satisfy the conditions $f^{(1)} \pm f^{(2)} \pm f^{(3)} = 0$ that are necessary for such excitation (de la Fuente et al., 2008).

We also note that for the cases with strong rotation $S < 1$ at location D there are weak spikes of energy of interface displacement spectra near f_5. The frequency of this wave corresponds to the fundamental wave along the basin width ($\approx f_{1T} = c_0/(2B)$). These waves may be exited directly by forcing because near-surface currents are deflected by rotation and cause weak upwelling/downwelling also along basin width.

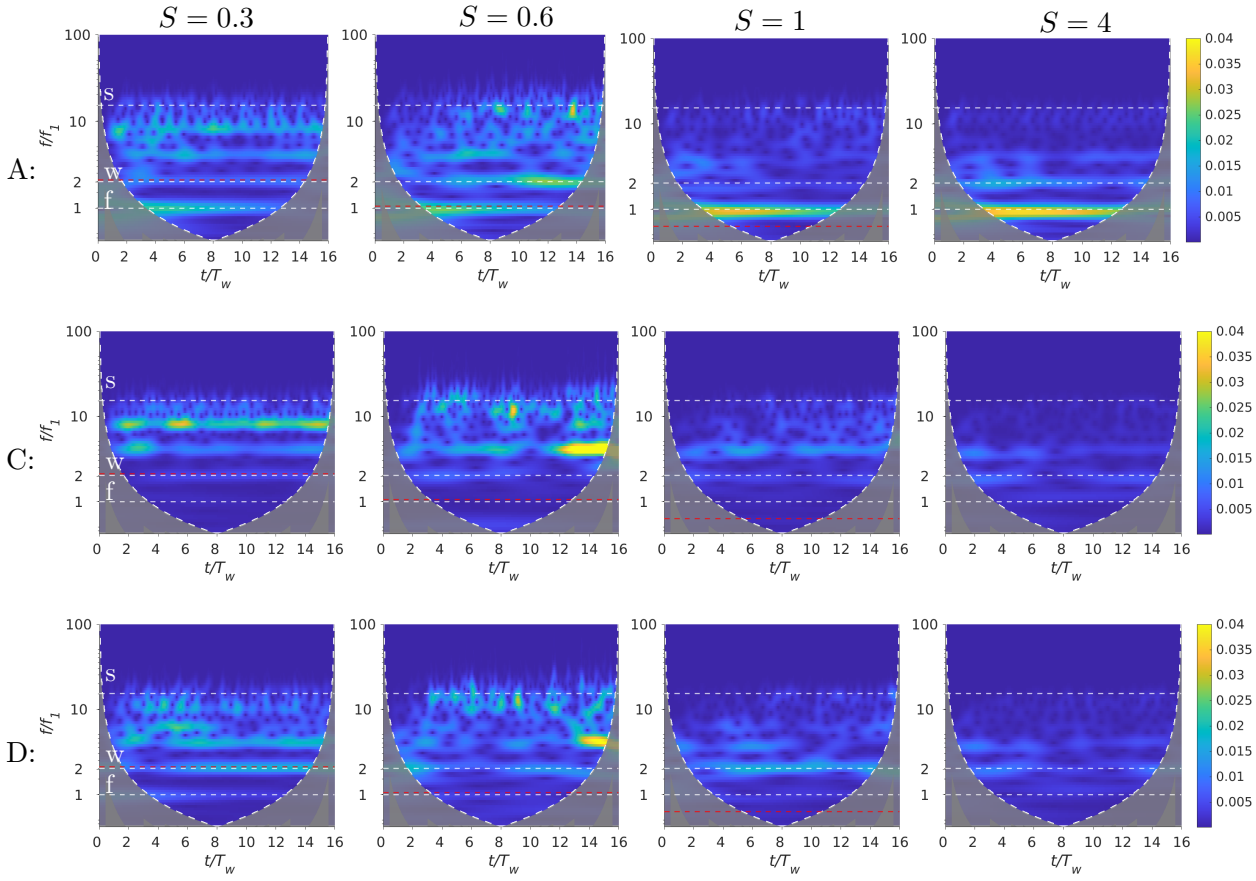

Figure 3.7: Wavelets of interface height sampled at locations A, C, and D shown in rows for $r_T = 0.5$ and S denoted in the figure. The colorbar represent absolute values of the continuous wavelet transform. Line – – – represents inertial frequency f_i, while dashed white horizontal lines denoted with letters indicate: w, forcing frequency f_w ; f, fundamental frequency f_1 ; s, approximate frequency of solitary-like waves $\approx f_s$. All frequencies are nondimensionalized with the forcing frequency f_1.

We conduct wavelet analysis of the interface height time series to observe the time development of the wavefield and its dominant waves. In figure 3.7 we show wavelets of the interface height time series for some Burger numbers. At the near-wall location A the wave with the near-fundamental frequency f_1 is the most energetic one, followed by the forcing one f_w and the multiple weakly energetic superharmonics. Further transfer of energy towards the higher frequencies energizes the high-frequency waves. We notice that for the cases with the strong rotation low frequency waves (f_1, f_w) are less energetic while high-frequency waves are more energetic compared to the weakly rotating and nonrotating case. We should

note that lower energies in the low-frequency waves may be attributed to the different partitioning of energy between the kinetic and potential one for the rotational gravity waves, as mentioned in Chapter 1 and to the focusing of Poincaré waves into the basin center.

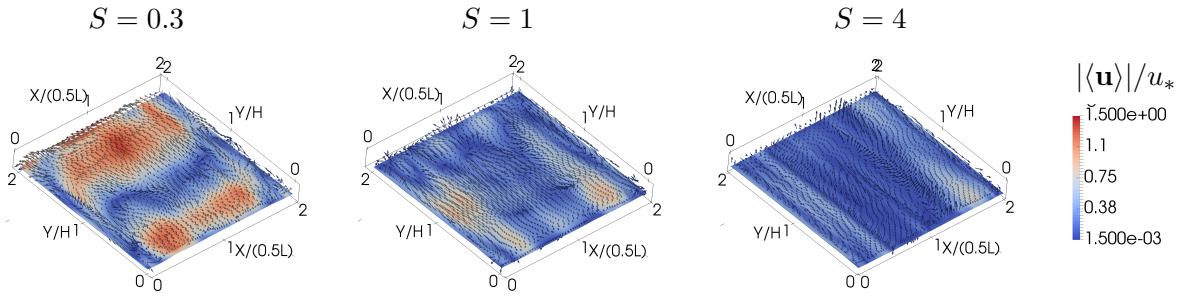

Figure 3.8: The nondimensional phase-averaged velocity magnitude at $\varphi = 30°$ shown at the isopycnal surface ρ_0.

At location B (not shown) we observe that the wave with the forcing frequency f_w is the most energetic while there is some energy content also in the fundamental wave and higher frequency waves. We note that the wave with forcing frequency observed here does not represent second horizontal mode V1H2 that has a similar frequency f_2 as the forcing one because this location is nodal for the H2 wave. There is a characteristic behavior that with the decrease of S the energy in the low-frequency waves decreases, while in the high-frequency ones it increases.

At the central location there is an increased energy content in waves with frequencies near $f_4 \approx f_{w2}$ and $f_8 \approx f_{w4}$ for the strong rotation cases $S < 1$. Based on our inspection of rotary spectra, these waves belong to anticyclonic Poincaré-type waves.

At location D, we observe the wave with the forcing frequency f_w and a higher superharmonic f_{w2}. Given the frequency and location, this wave can be either V1H2 mode f_2 or rotational wave with forcing frequency. We note that the weakly rotational $S = 4$ and nonrotational case have almost identical wavefields.

Overall we note that cases with $S \geq 4$ where rotation is weak or absent have the response that corresponds to a stable state as defined in Section 2.5. For $S = 1$ we observe that after about 8 forcing periods, the energy contained in fundamental and forced waves (at f_1 and f_w) decreases, and waves with higher

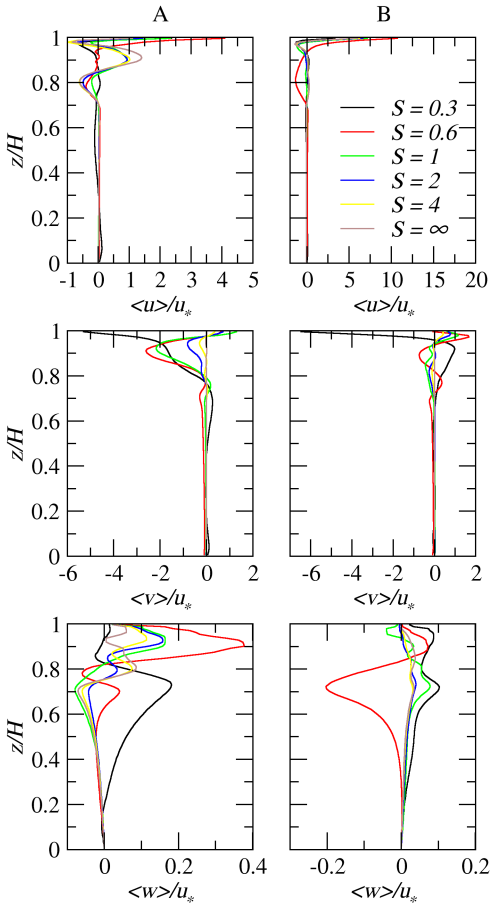

Figure 3.9: Vertical profiles of the phase averaged velocity components sampled at locations A and B at the forcing phase $\varphi = 120°$. Phase φ corresponds to phase of the the forcing period.

frequencies are energized. For $S = 0.3, 0.6$ we note that response is even more unstable, as forced wave and its superharmonics are energized and lose energy several times. Each loss of energy is followed by energizing of high-frequency waves.

In figure 3.8 we show the velocity field at the interface surface for the three cases with rotation $S = 0.3, 1, 4$. We observe that for the $S = 0.3$ there is a divergent central region that splits the flow into the two cells along with the y-axis. The cells have maximum in their central regions, at about $(0.5L, 0.25B), (0.5L, 0.75B)$, where sampling location D is located. This explains the most energetic readings that we observed there in spectral analysis and indicates that the dominant Poincaré waves appear as second horizontal mode. For weaker rotation $S = 1, 4$, there are multiple stripes with velocity maximum, corresponding to wave crests along the y-axis. We note that for $S = 1$ there are fewer stripes, they are wider and have higher velocities compared to the $S = 4$ case, which indicates that the most energetic wave response has a lower horizontal modal structure.

We inspect vertical profiles of the instantaneous velocity components sampled at locations A and B in order to gather more information on the vertical modal structure of the wave field. In figure 3.9 we show some of the phase averaged profiles. The profiles of the horizontal velocity component reveal the vertical mode of the dominant response, while vertical velocity is more sensitive to different modes that pass through the sampling location at the time instant.

At the near-wall location A, streamwise velocity $\langle u \rangle$ is lowest for $S < 1$, and its amplitude at the middle of metalimnion $\approx 0.8z/H$ decreases as the rotation intensifies. The profiles of cases with high S have a V4 structure. The spanwise component $\langle v \rangle$ shows V1, V2 structure for low S and V2, V2 structure for high S. The spanwise velocity amplitude increases for low S. The behavior of both velocity components can be interpreted as the development of Kelvin waves at low Burger numbers, which is characterized by the flow parallel to the boundary. Under the influence of Kelvin waves, vertical velocity component $\langle w \rangle$ is substantially higher for the cases under the strong rotation, and it displays the profiles that correspond to the multiple vertical modes: V2, V3, V4, where higher modes generally belong to the cases with weak rotation.

At the internal location B, for streamwise velocity component $\langle u \rangle$, the V3 structure prevails for most of the cases. The exception is $S = 0.6$ where a more energetic V2 response develops. The spanwise velocity $\langle v \rangle$ shows complex behavior with various vertical structures, from V2 to V4. The vertical velocity shows the dominant V1 behavior for most of the profiles, with additional oscillations on the main profile that indicate the existence of higher mode waves superimposed on the V1 mode. The exception is the most energetic $S = 0.6$ case which has a clear V2 structure.

In order to investigate how do the different responses influence the turbulence fields we calculate the turbulence dissipation rate and parametrize the turbulence diffusivity of density following the Bouffard and Boegman (2013). The slices through these fields for the five cases are plotted in the figure 3.10.

The highest values of the dissipation rate are located in the near-surface region. Throughout the metalimnion these values are elevated, while hypolimnion is generally calm. Throughout the slices, the values increase with the rotation rate (decrease of S) until $S = 0.6$. For the weakly rotational and nonrotational cases $S \geq 1$ the dissipation rate in the hypolimnion is slightly increased in beams that radiate from the metalimnion, and that likely originate from the solitary-like waves. For the rotation $S < 1$ there is weakly increased dissipation throughout the hypolimnion, with a particular layered structure observable in the $x - y$ plane which likely originates from the weak shear that appears due to vertical modes and Ekman spiral that appear in the bottom layer.

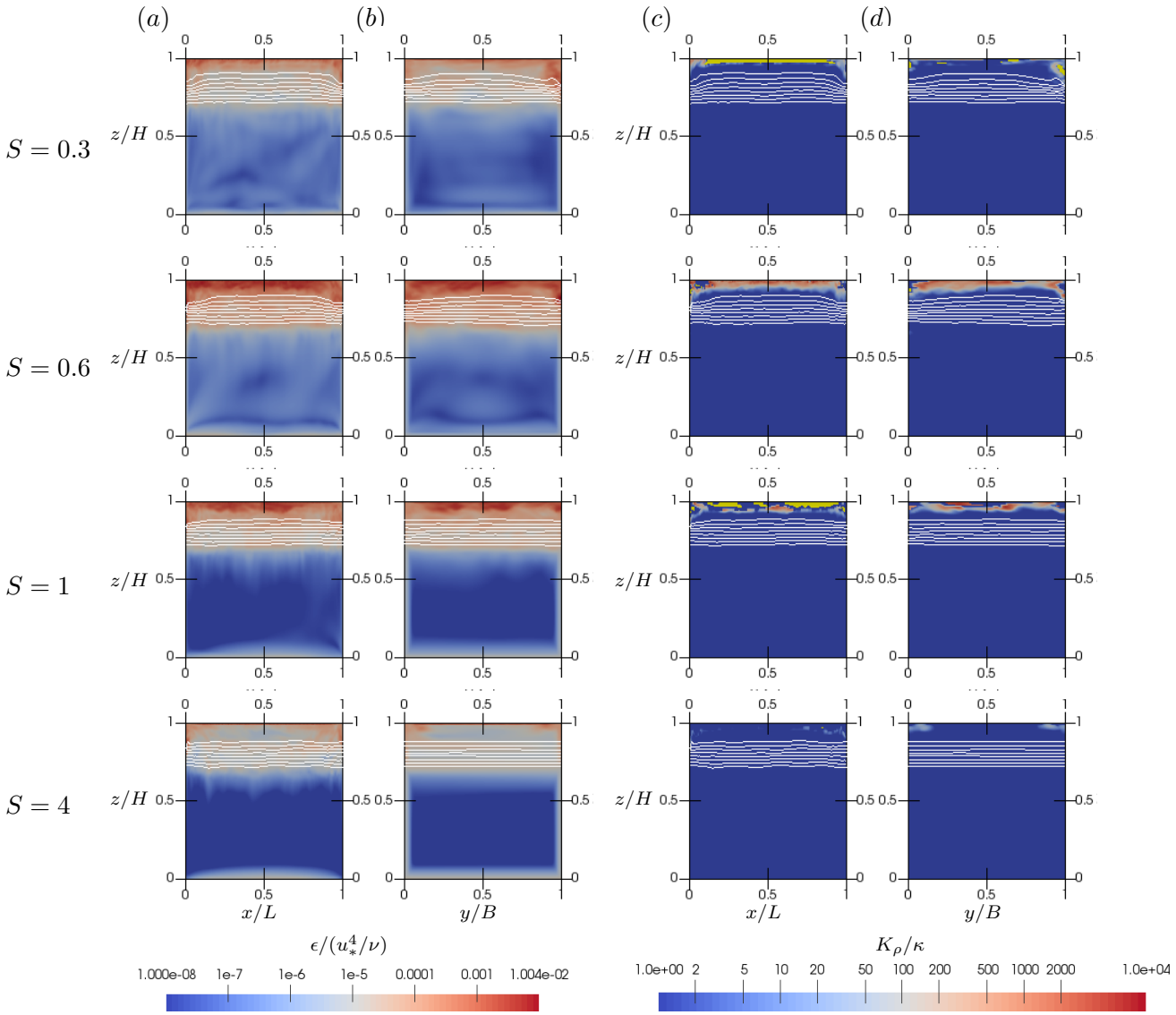

Figure 3.10: Slices in $x - z$ (a, c) and $y - z$ (b, d) planes through turbulence fields for $r_T = 0.5$ at the forcing phase $\varphi = 30°$: (a, b), nondimensional dissipation rate; (c, d) nondimensional turbulent diffusivity of density. White lines indicate isopycnals while the yellow color represents the regions with unstable stratification, where $\langle N^2 \rangle$ is negative.

The turbulent diffusivity K_ρ is high only in the near-surface layer, where also overturns occur (yellow regions in figure 3.10(c, d)). The shape of isopycnals shows that wave response is very weak and there is no observable upwelling.

In order to put the observed behaviors in the global perspective, we spatially and temporally average the dissipation rate using the volume-weighted averages in space and averages over forcing cycle with the phase step $\Delta\varphi = 30°$ in time. The averaged dissipation rate is plotted versus the Burger number S in the figure 3.11(a). The averaged dissipation rate generally decreases with the increase of Burger number. The only exception is $S = 0.3$, which indicates that for this rotation rate there is a change in the response mode compared to other cases, this is expected given that in this case forcing frequency is subinertial. For the increase of $\langle \epsilon \rangle_{s,t}$ compared to nonrotational case ranges from 50% for $S = 4$ to 15

times for $S = 0.6$.

In order to observe the influence that different rotation rates have on mixing, we use a sorting algorithm to find the horizontally averaged background density field at the final time and to calculate the total change of background potential energy as the indicator of total mixing (see equation (2.10) according to Peltier and Caulfield (2003)). The sorting procedure is used in order to eliminate the influence of the wave and forcing state on the density field. In figure 3.11(b) we show the nondimensional total change in background potential energy (mixing) with respect to Burger number. We observe that mixing increases as rotation intensifies for low Burger numbers $S < 1$. At higher Burgher numbers ($S \geq 1$), mixing is nearly constant with a weak trend of increase with the weakening of rotation. We find the difference between the final background density profile and the initial (background) density profile and use the differences in density as an indicator of mixing location, as shown in figure 3.11(c). Throughout the layer that was subject to mixing, the density difference is greatest for the cases with strong rotation $S < 1$. In the near-surface layer and the lower end of metalimnion, mixing increases with rotation for the full range of S. While the difference between the cases with weak rotation is small, it may be important for the development of the waves with higher vertical modes, that are sensitive to the thickness of the stratified layer. In the internal part ($z/H \approx 0.8$). the amount of mixing is not proportional to the rotation rate, as it decreases as rotation weakens up to $S = 1$, after which it increases with the weakening of the rotation.

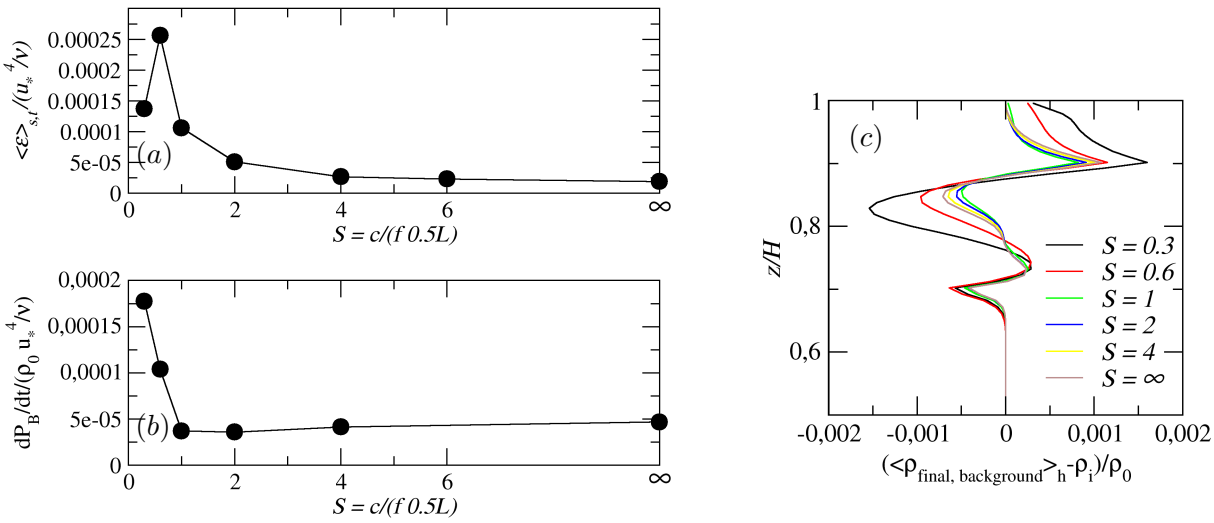

Figure 3.11: Averaged quantities as global indicators of turbulence and mixing for $r_T = 0.5$: (a), spatially and temporally averaged nondimensional dissipation rate with respect to Burger number; (b), the total change in the background potential energy; (c), the difference of the background final horizontally averaged density profile compared to the initial one.

Summary: A lake-like stratified system that is periodically forced by a weak-to-moderate wind shear stress with a period close to half-fundamental period will respond with weakly energetic wave field in which basin-scale waves with the forcing and fundamental frequency with higher vertical modes dominate, while waves with higher horizontal modes occur as superharmonics of the forcing frequency. The rotational effects significantly modify the internal wave response as they destabilize the wave response and tend to excite more energetically waves with higher frequencies. When forcing frequency is superinertial, the most energetic Poincaré waves occur near the forcing frequency for any tested case with rotation. When

forcing frequency is subinertial, Poincaré wave response is reduced, even if forcing frequency is close to inertial one. As rotation gets stronger Poincaré wave strengthens and appears also in form of higher vertical modes. The turbulence is generally confined in the near-surface region, which is where most of mixing occurs. Rotational effects increase the overall amount of dissipation as long as the forcing frequency is superinertial. This indicates that increased dissipation is directly related to the Poincaré wave response, in agreement with the findings of Bouffard et al. (2012) that Poincaré waves are responsible for increased dissipation and mixing in the metalimnion interior. In cases with a strong rotation, the amount of the mixing increases as rotation intensifies. In the rotational cases, the Kelvin wave appears with the fundamental frequency.

3.4.2 Forcing period $r_T = 1$

The time series of interface height shown in figure 3.12 reveal the occurrence of the resonant amplification of the wave response for all tested Burger numbers. As expected, we observe the fundamental V1H1 response at locations A and B and nonlinear V1H2 responses at locations C and D. We notice that for the rotating cases the occurrence of the high-frequency waves is not timed by the steepening time scale, which is the time when high-frequency solitary-like waves are expected to be excited by the steepening of the nonlinear waves that originate from the linear ones. The high-frequency waves appear earlier and are more energetic as Burger number decreases and rotation strengthens. For the cases with $S < 1$ the interface oscillations at location D contain much more medium and high-frequency waves, that are not present at location C, thus they may be coastal effects or transversal waves with a node at the center C.

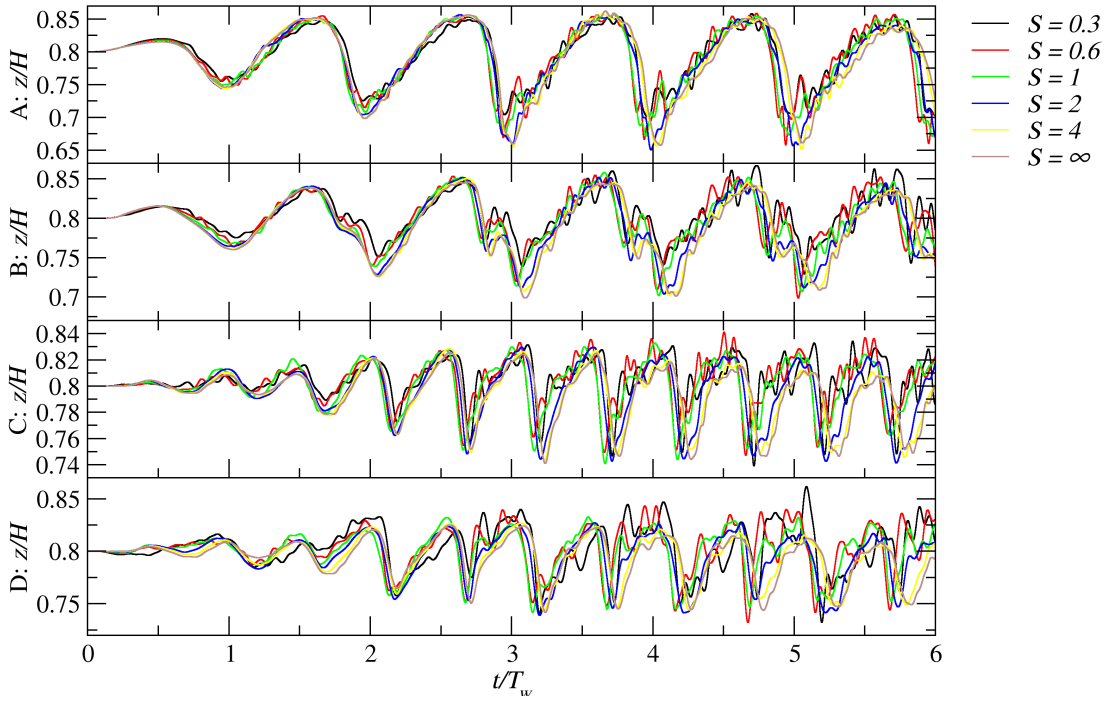

Figure 3.12: Time series of the interface displacement sampled at the four locations, defined in figure 3.4, for the cases with different Burger number S for $r_T = 1$.

The interface height spectra, rotary spectra and phase lag are shown in figure 3.13. At location A, we observe interfacial wave $f_1 \approx f_w$ followed by higher modes f_n. For the strong rotation cases $S \geq 1$, f_1 wave manifests as a cyclonically rotating Kelvin wave. This is true even in the case $S = 1$ when f_1 is superinertial frequency. We note that cyclonic currents with frequency f_1 are strongest in case $S = 0.6$, where $f_1 \approx f_i$. For the cases with weak rotation and superinertial forcing, anticyclonic Poincaré wave with f_1 dominates. The superharmonics f_n are mostly in the form of anticyclonic Poincaré waves. The phase lag is generally low near the low frequencies (with an exception at $0.4f_1$) and high in the region of high frequencies, except for the $S = 0.3$. The large phase lag here is likely to be caused by the disturbances caused by the wall effects, such as return jet, due to the proximity of the wall. The amount of energy in interface oscillations in the region of the high-frequency waves ($\sim 10f_1$) increases as rotation becomes stronger.

We note that the occurrence of Kelvin waves at $S > 1/\sqrt{2}$ (which is a theoretical limit for their occurrence in inviscid linear system) can be due to slowing down of the wave because of frictional effects as discussed by Wake et al. (2004). We also note that in our case, the frequency of Kelvin wave is not its natural frequency, rather the wave adjusts to forcing frequency, which was theoretically and experimentally shown and discussed in Rozas et al. (2014). Further, we stress the fact that in the rectangular case, S is not as definite as in the circular case due to a somewhat arbitrary choice of characteristic length. For instance, in Rozas et al. (2014), basin width instead of its length was used for calculation of S in a rectangular basin.

At location B, all waves are anticyclonic (Poincaré waves) in rotational cases. This is true also for f_1 in $S = 0.3$ case, which is atypical given that $f_1 < f_i$ and the formation of Poincaré waves is not permitted. The f_2 wave is absent from interface oscillations, which confirms it as an H2 wave for which this location is the nodal one, yet for the weakly rotational cases there is substantial phase lag associated with this frequency. A significant phase lag that varies on each case is present also near some of the higher (horizontal) modes f_6, f_7, f_8.

At location C, odd modes are absent from the interface spectra. The rotational characteristics reveal anticyclonic, Poincaré waves across all modes (for rotational cases). Substantial phase lag is present near f_1 for weakly rotational cases and f_3 for all cases. Phase lag near f_1 corresponds to previously observed (in Section 2.4) periodic contraction and spreading of the middle layer. We note that with the decrease of S the currents at higher modes f_n become more energetic. The increase of energy at higher modes can be explained with different energy partition among potential and kinetic energy, where for Poincaré waves $KE > PE$.

At location D, in the weakly rotational cases, the odd modes are absent from the interface spectra, while they become more energetic as rotation intensifies. The increase of energy in interface oscillations at location D compared to C for frequency f_1 would indicate that the observed wave is Kelvin-type, yet the rotation of the currents is anticyclonic. Substantial phase lag is present near f_1 (except for $S = 0.3$) and f_3. For strongly rotational cases $S < 1$ we observe energy spikes in interface displacement near $f_{1T} = c_0/(2B) = 5f_1$ which are not present at location C. These waves are likely to be excited by deflection of surface forcing to the lateral sides that cause internal setup (upwelling/downwelling) along the basin width.

The occurrence of weakly anticyclonic subinertial waves is more likely to be due to the influence of the Coriolis force on the currents due to the resonantly forced internal seiche than the occurrence of the subinertial Poincaré waves.

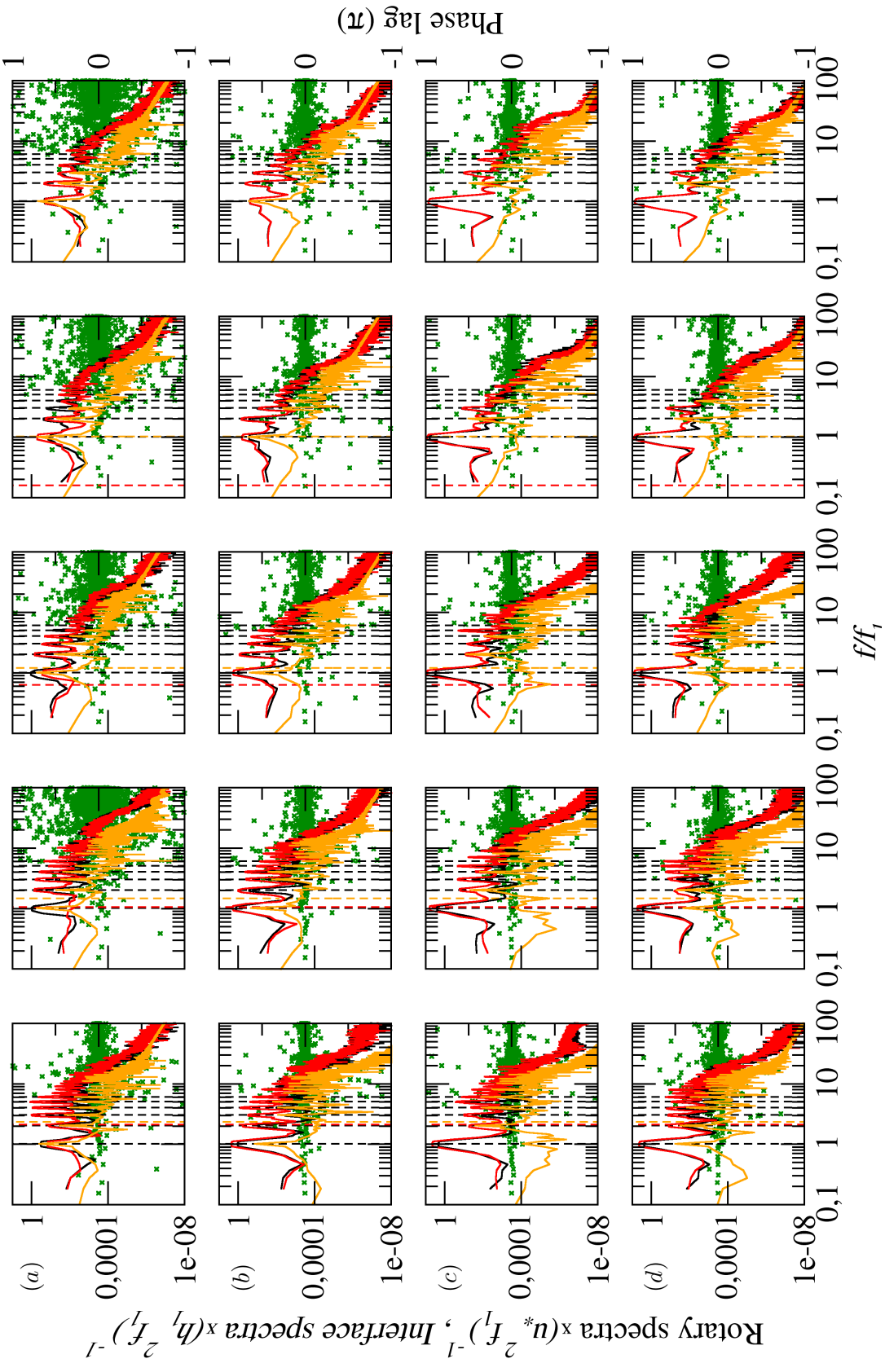

Figure 3.13: Rotary spectra of horizontal velocity components, interface height spectra and phase lag for Burger numbers denoted over columns. The sampling locations are set in rows as: (*a*), A; (*b*), B; (*c*), C; (*d*), D. The notation is following: —— cyclonic rotation; —— anticyclonic rotation; —— interface spectra; x phase lag. Dashed vertical lines denote: - - - forcing frequency f_w and its superharmonics $_{wm}$; - - - inertial frequency. The fundamental frequency f_1 and its superharmonics f_n can be read directly from the x-axis that is scaled accordingly.

The wavelet analysis of the interface height series shown in figure 3.14 reveals the highly energetic fundamental wave V1H1 and a number of higher modes. At location D, we observe that the most energetic is f_2, corresponding to V1H2, but as rotational effects become important, there is an increased amount of energy around to f_1 (f_w). Given that location D is nodal for the fundamental V1H1 wave, this indicates the formation of the rotational gravity wave. We observe that as the rate of rotation increases, more energy is transferred towards the medium and high-frequency waves and the transfer occurs earlier; this can be best observed on locations C and D where the energy scale is lower. Even the weakly rotational cases exhibit similar characteristics but in a much smaller amount. We note that all cases are in a stable state with only minor modifications in energy distribution with respect to rotational effects.

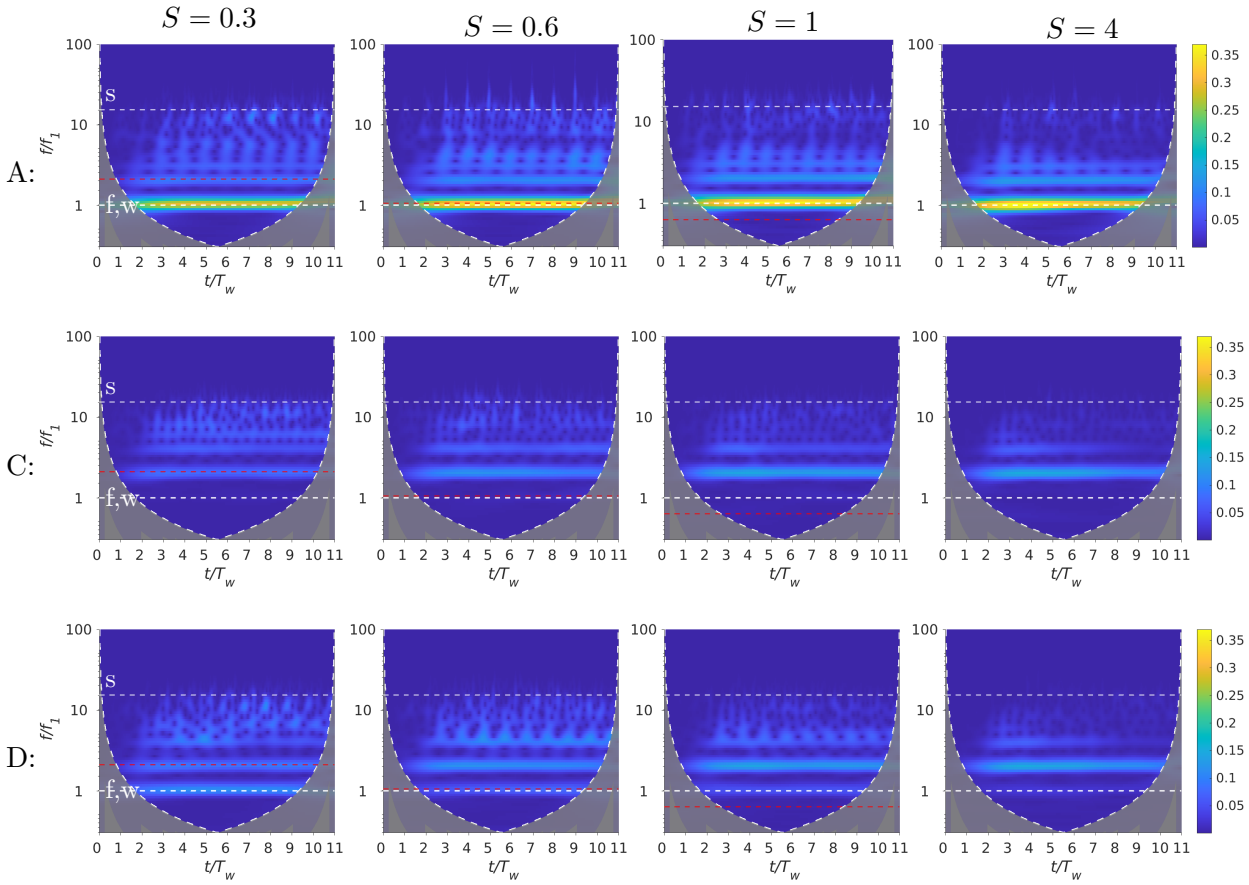

Figure 3.14: Wavelets of interface height sampled at locations A, C, and D shown in rows for $r_T = 1$ and S denoted in the figure. The colorbar represent absolute values of the continuous wavelet transform. Line – – – represents inertial frequency f_i, while dashed white horizontal lines denoted with letters indicate: w, forcing frequency f_w ; f, fundamental frequency f_1 ; s, approximate frequency of solitary-like waves $\approx f_s$. All frequencies are nondimensionalized with the forcing frequency f_1.

The phase averaged velocity vectors at the interface (surface with density ρ_0) are shown in figure 3.15. We observe that in all cases, the maximum velocity is next to the wall and decreases away from it, corresponding to the Kelvin wave behavior. As S decreases (due to the decrease of Rossby radius), the influence of the Kelvin wave moves from being basin-wide to the near-wall phenomena, which is followed by increased velocities. In the following figure, we see that at the later phase, the most energetic Kelvin wave ($S = 0.3$) steepens and produces nonlinear waves, which corresponds to the behavior for nonlinear and non-hydrostatic regime documented by Ulloa et al. (2015). In other cases, the degeneration of the

Kelvin wave belongs to the nonlinear regime. In Ulloa et al. (2015), they investigated the regimes for single Burger number $S = 0.25$ while varying the Wedderburn number and aspect ratio of Kelvin wave. We are keeping these parameters constant and observe that the regime changes when varying S, which was correctly hypothesized by Ulloa et al. (2015).

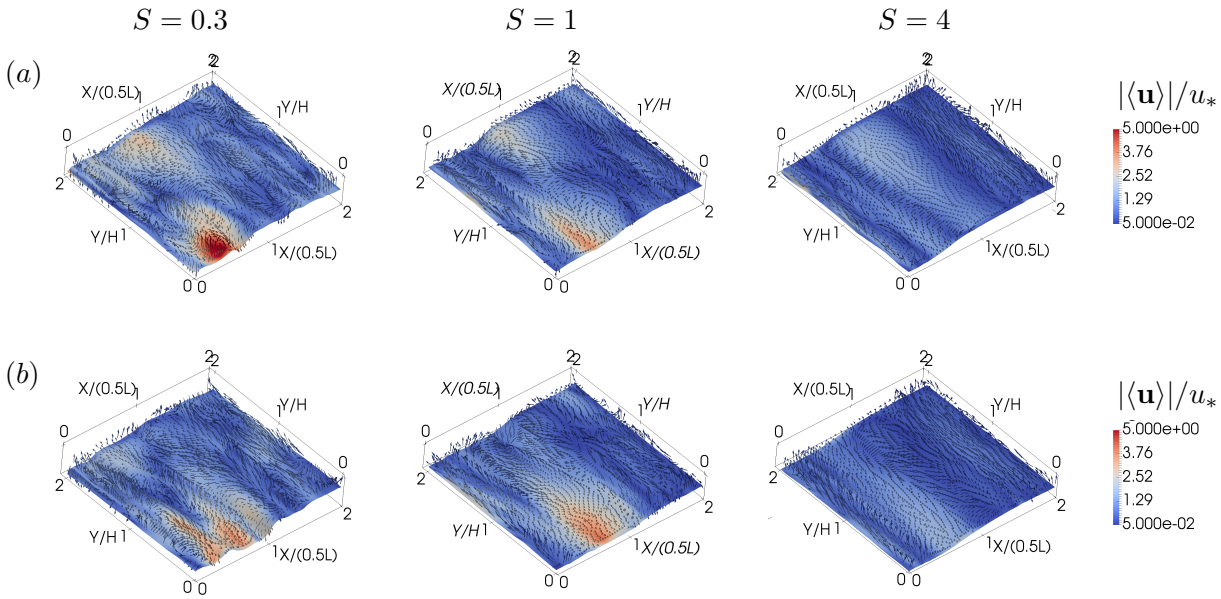

Figure 3.15: The phase averaged nondimensionalized velocity vectors $\langle \mathbf{u} \rangle / u_*$ shown on the interface surface ρ_0, both colored with the nondimensional velocity magnitude $|\langle \mathbf{u} \rangle|/u_*$, for the three Burger numbers denoted above at the forcing phase: (a), $\varphi = 30°$; (b), $\varphi = 60°$.

The vertical profiles of the velocity components are shown in figure 3.16. At the near-wall location A, $\langle u \rangle$ profiles have many oscillations at the profile for low S (corresponding to V4, V5), while high S cases display V1 behavior. The spanwise velocity component $\langle v \rangle$ mainly shows a V2 structure with many additional oscillations superimposed on the V2 main profile. The vertical velocity profile has V1 and V3 structures. As we noted in the discussion about the phase lag on this location, this is more likely to be the influence of the proximity of the wall than the actual development of waves with corresponding vertical modes.

Internal location B, shows a clear V1 structure in $\langle u \rangle$ profiles of all cases, while $\langle v \rangle$ profiles are a combination of V1 and V3 modes. The dominance of V1 modes is visible also in $\langle w \rangle$ profiles, but also V3 mode can be observed (for $S = 0.3$).

To characterize the turbulence fields, we calculate turbulence dissipation rate ϵ and parameterize turbulent diffusivity of density K_ρ shown in figure 3.17. The dissipation rate is highest in the corner where forcing causes the flow to turn downward, and downward movement is subsequently blocked by the strong stratification. The dissipation in this region is highest for weakly rotating and nonrotating cases. As rotation intensifies the dissipation rate in this region decreases, but additional regions with dissipation rate form at the sidewalls (figure 3.17(b)) as surface currents deviate due to the rotational effects. Throughout the metalimnion, the dissipation rate is moderate, while in the hypolimnion it is low,

but there is a characteristic increase of dissipation rate in these regions as rotation strengthens. While in the weakly rotating cases, the dissipation in the hypolimnion radiate from metalimnion in a beam-like form, which is associated with the passage of the solitary-like waves, for Burger number $S < 1$ there is a clearly layered structure, that originates from the shearing layers. In the $y - z$ plane, we do not observe dissipation beams associated with the solitary-like waves, that typically travel along the x axis. In this plane, we observe that rotational cases develop asymmetry, and we particularly notice the region with deviated isopycnals and increased ϵ for $S = 1$ that corresponds to the passage of the forced Kelvin wave.

On the figures 3.17(c, d) we observe parameterized turbulence diffusivity and regions with unstable stratification that indicate the overturning events. In the xz plane, we observe that most of the mixing occurs in the region that is under the direct influence of the return jet. Some amount of mixing is present also in the near-surface region. We note that the mixing location shifts from the near-wall metalimnion towards the surface layer as rotation intensifies. In the $y - z$ slice, we observe some near-surface mixing and a calm interior. For the rotational cases $S \leq 1$, we observe overturn event near the wall which is caused by the downward near-wall motion due to the surface current that is deflected by rotation.

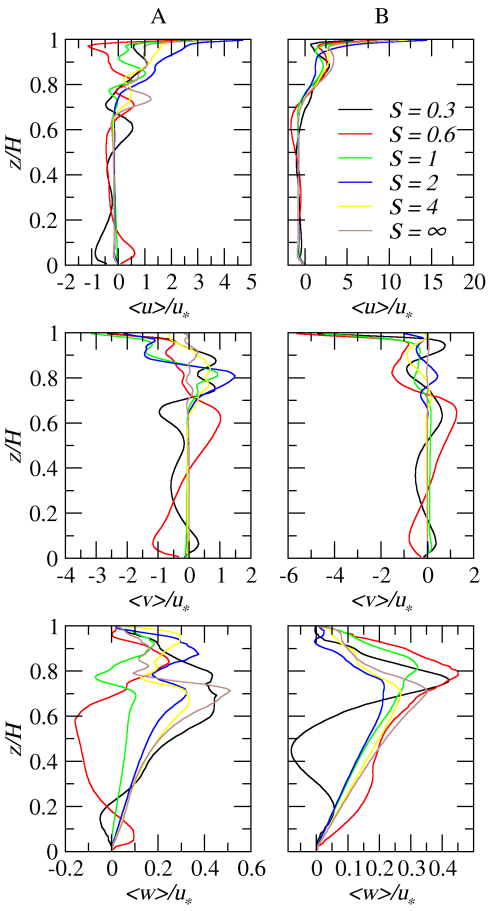

Figure 3.16: Vertical profiles of the phase averaged velocity components sampled at locations A and B at the forcing phase $\varphi = 120°$.

In the figure 3.18 we show quantities that we use to globally quantify the amount of turbulence and mixing. In figure 3.18 (a) we observe that the global amount of the turbulence dissipation rate increases as rotation intensifies. The deviation from this increase can be observed for the $S = 0.3$ case. The mixing indicator shown in figure 3.18 (b) reveals that mixing increases with a decrease of S for high S and decreases with a decrease of S for low Burger numbers $S \leq 1$. The range of S in which mixing decreases with the intensification of rotation corresponds to cases in which we observed the development of Kelvin wave with the frequency of forcing (see rotary spectra in figure 3.13(a)). The profile of difference between initial and final background density shown in figure 3.18 (c) shows an increased mixing at the lower end of metalimnion as rotational effects are included, which leads to the deepening of the metalimnion. Near the middle of metalimnion, $z/H \approx 0.8$, and in near-surface layer, the amount of mixing increases with Burger number. Overall, the most mixed case is $S = 2$. It seems that the amount of mixing and dissipation with respect to Burger number are not directly correlated. This is because most of the mixing occurs in the near-wall region, where both mixing and dissipation increase with S, while overall dissipation increases with the decrease of S, which is mostly due to the increased

dissipation in the internal regions where turbulence is not strong enough to substantially mix the density field, therefore we only observe small differences related to the deepening of the metalimnion. We note that the stratification used in our simulations is characteristic for laboratory scales, with Richardson number substantially higher than in real lakes. Besides, the uniform stratification herein used rarely occurs in nature, where usually weak stratification is present. In other words, more mixing and a higher correlation between dissipation and mixing can be expected in natural conditions.

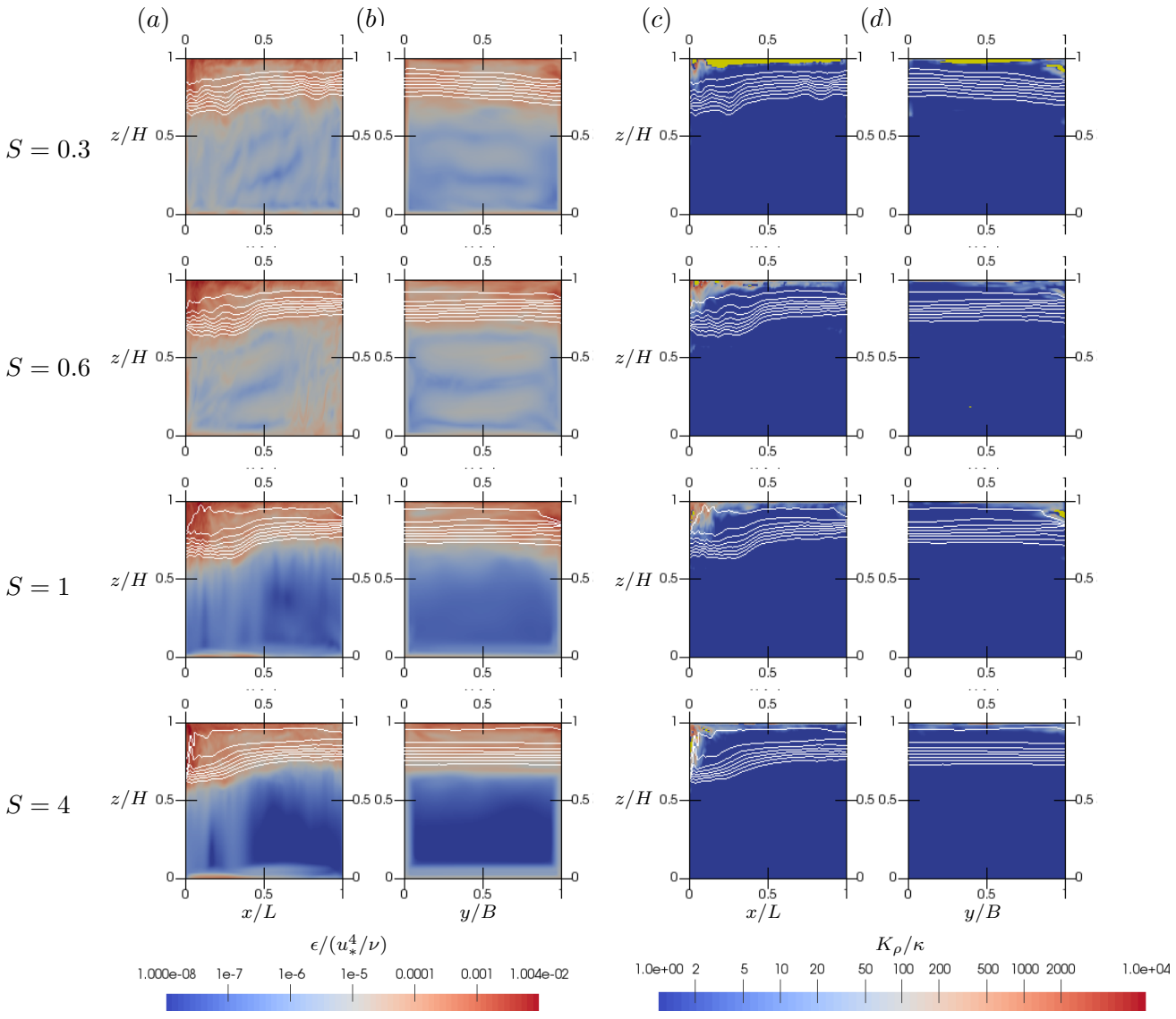

Figure 3.17: Slices in $x - z$ (a, c) and $y - z$ (b, d) planes through turbulence fields for $r_T = 1$ at the forcing phase $\varphi = 30°$: (a, b), nondimensional dissipation rate; (c, d) nondimensional turbulent diffusivity of density. White lines indicate isopycnals while the yellow color represents the regions with unstable stratification, where $\langle N^2 \rangle$ is negative.

Summary: A three-layer stratified system that is forced with weak to medium periodic forcing and whose period matches the fundamental one will develop a resonant response in terms of a resonant basin-scale wave, which passes its energy to its superharmonics in the mode of higher horizontal modes and

energy is further transferred to the high-frequency solitary-like waves. In this case. the rotating systems are clearly more efficient in passing the energy to the high-frequency waves. For cases with a strong rotation, the near-wall wave field is characterized by Kelvin wave with frequency of forcing. The wave field in the internal region is characterized by wave with frequency of forcing and its superharmonics that appear in form of Poincaré waves. Weakly anticyclonic, Poincaré-like waves appear near the resonantly forced frequency, even when it is subinertial due to deflection of its currents by Coriolis force. Waves generally have vertical structure of the first vertical mode V1. There is a tendency of increase of turbulence dissipation rate as rotation intensifies, while it decreases when the frequency of forcing becomes strongly subinertial. The increase in dissipation rate is related to the higher amount of the high-frequency waves and to stronger shear arising from Poincaré waves in rotational cases. The increase of dissipation with the rotation rate leads to increased mixing only in the lower edge of the metalimnion, while throughout metalimnion and in the near-surface region mixing decreases as rotation intensifies, due to weakening of the near-wall mixing by the return jet.

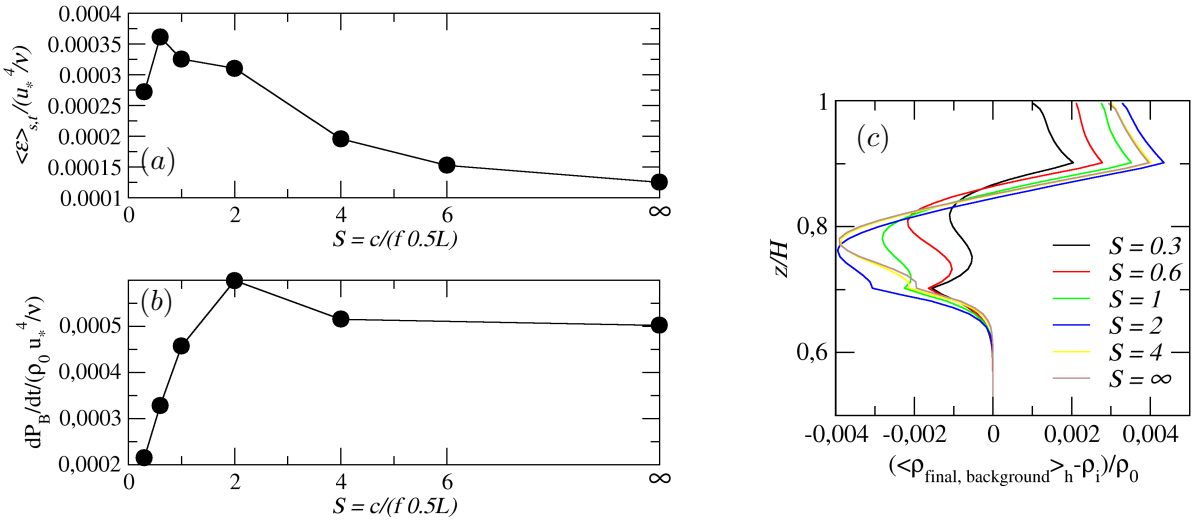

Figure 3.18: Averaged quantities as global indicators of turbulence and mixing for the $r_T = 1$: (a), spatially and temporally averaged nondimensional dissipation rate with respect to Burger number; (b), the total change in the background potential energy; (c), the difference of the background final horizontally averaged density profile compared to the initial one.

3.4.3 Forcing period $r_T = 2$

In the previous Chapter 2, we identified that the nonrotational system that is forced with $r_T = 2$ responds with the forced basin-scale second vertical mode V2H1 wave. Similar responses are obtained for rotational cases. In figure 3.19 we show the interface height series. We observe that the initial periodicity of the wave response corresponds to the fundamental period. The degeneration of this wave to the high-frequency waves occurs around the end of the first forcing period. As for the previous forcing periods, we observe that high-frequency waves appear earlier for the cases with lower Burger number S, while here the amplitude of these waves decreases substantially near the end of the time series for the cases with low Burger number $S \leq 1$ at locations A and B. At locations, C and D the period of the dominant waves for the high Burger numbers $S > 1$ correspond to the half-forcing period. While the cases with lower S

display much weaker long-wave responses and are dominated by the high-frequency waves. We note that the time series diverge with time, namely, there is a decreasing trend of interface height that is related to S, where higher S produces a larger decrease as a direct consequence of mixing and changes in the background density.

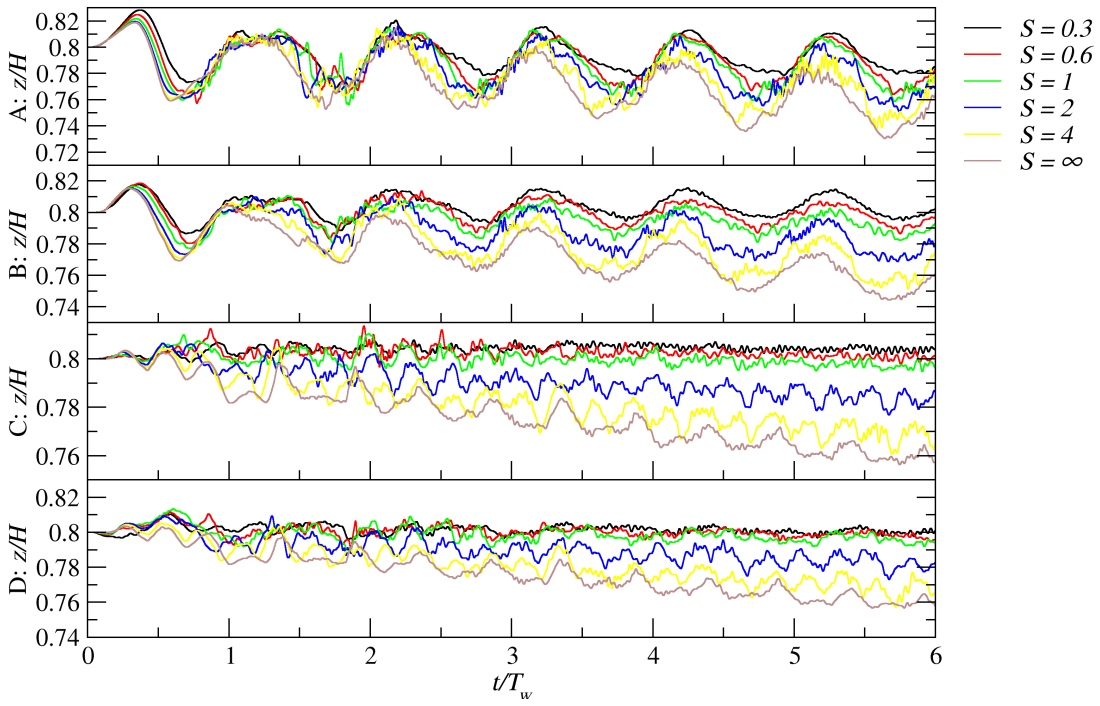

Figure 3.19: Time series of the interface displacement sampled at the four locations, defined in figure 3.4, for the cases with different Burger number S for $r_T = 2$.

The combination of graphs of interface spectra, rotary spectra and phase lag is shown in figure 3.20. At location A, we observe that cyclonically rotating Kelvin wave with the frequency of forcing f_w develops only for low Burger numbers $S \leq 1$ where $f_w < f_i$ with higher superharmonics f_{wm} in terms of Kelvin waves appear at subinertial frequencies. We note that for the case $S = 0.3$ cyclonic currents at f_w are negligible, while they do appear in f_{w2}. Superinertial superharmonics f_{wm} mostly have anticyclonic rotation and correspond to Poincaré waves. Interface oscillations correspond mainly to f_w, while for $S = 0.3$ additional peaks are present at f_{w2}, f_{w3} where Kelvin wave develops. There is weak phase lag near f_w, while in the high-frequency region high phase lag is associated with the wall effects.

The interface spectra at the B location shows the most energetic f_w and some of the higher modes f_{w2}, f_{w3}. The energy of these higher modes is higher in cases where they are subinertial. The rotational characteristics of most of the present waves are anticyclonic. A phase lag near f_w and superharmonics f_{wm} is high for $S \geq 1$ which reveals the vertical wave structure as a higher vertical mode. For stronger rotation, phase lag at f_w is low, while it appears elevated at the higher modes that have $f_{wm} > f_i$, which indicates that Kelvin wave appears with V1 structure, while Poincaré waves have a higher vertical structure.

The central location C shows the dominance of even superharmonics f_{w2}, f_{w4} in interfacial oscillations and we can identify them as even horizontal modes. The currents are mostly nonrotational for subinertial frequencies. At superinertial frequencies, anticyclonic Poincaré waves dominate. We note that the energy

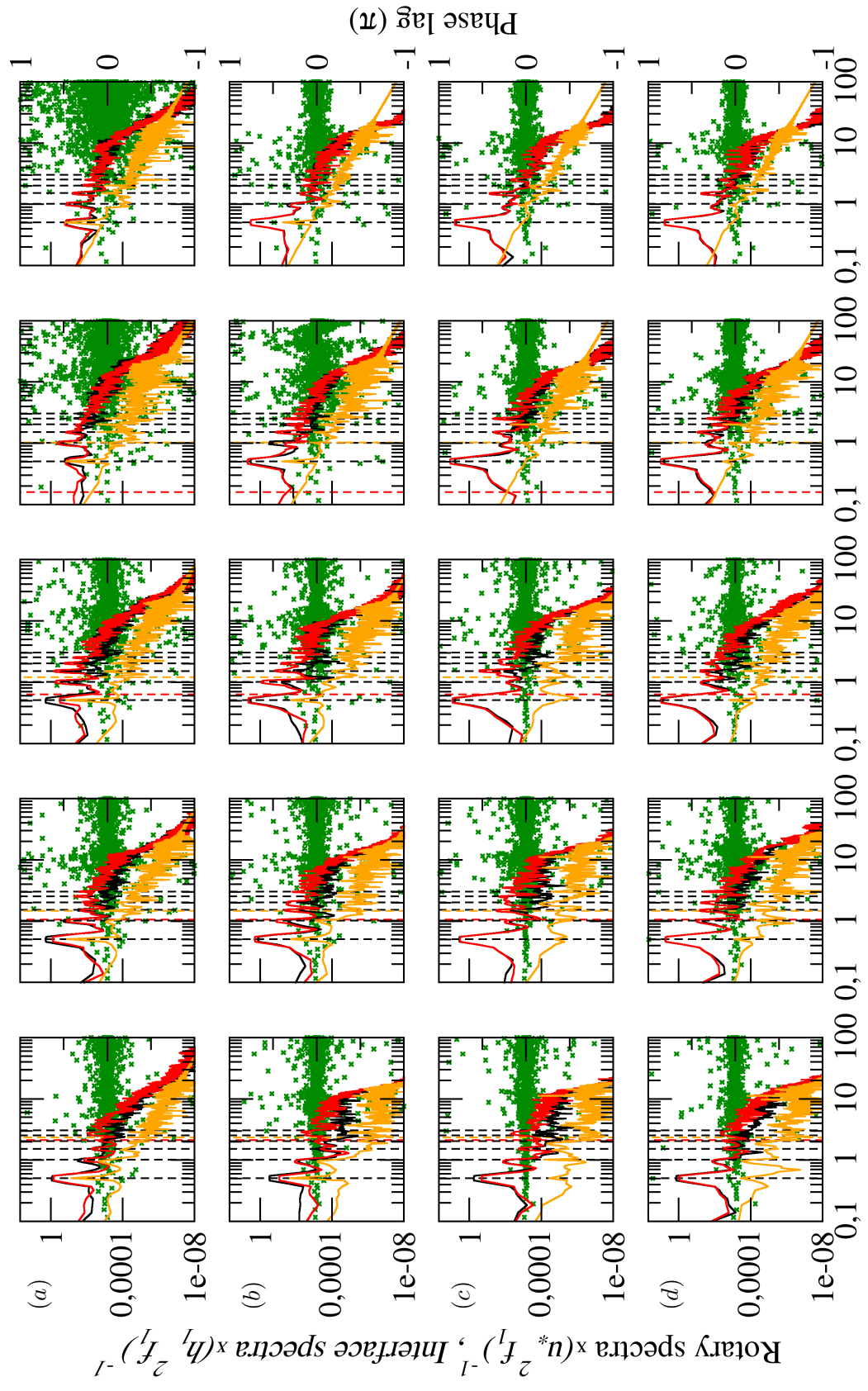

Figure 3.20: Rotary spectra of horizontal velocity components, interface height spectra and phase lag for Burger numbers denoted over columns. The sampling locations are set in rows as: (*a*), A; (*b*), B; (*c*), C; (*d*), D. The notation is following: —— cyclonic rotation; —— anticyclonic rotation; —— interface spectra; x phase lag. Dashed vertical lines denote: - - - forcing frequency f_w and its superharmonics $_{wm}$; - - - inertial frequency. The fundamental frequency f_1 and its superharmonics f_n can be read directly from the x-axis that is scaled accordingly.

of the currents at the same frequencies (i.e. f_w) decreases as it becomes subinertial (with the decrease of S) which corresponds to energy partition related to Poincaré waves. Phase lag is high at superinertial frequencies.

At location D, interfacial f_w wave is absent at high S, revealing the odd horizontal structure of this wave. At low S, an energy spike at f_w is present and this frequency is characterized by a large phase lag. Some of the higher modes are present (f_{w2}, f_{w4}). The rotary spectra reveal an anticyclonic, Poincaré, nature of the observed superinertial waves, while phase lag indicates the occurrence of the higher vertical modes. We note that for the low Burger numbers ($S < 1$), phase lag at f_w can be observed only at location D, which indicates that the waves with the higher vertical mode that appear there have a transversal propagation.

Wavelet analysis of the interface height time series shown in figure 3.21 reveals the wave with forcing frequency f_w as the most energetic at locations A and B for all cases. The initial response was characterized by the f_1 wave that is soon canceled and its energy is transferred towards the high-frequency waves (detailed discussion in Section 2.4). Unlike the first two discussed cases ($r_T = 0.5, 1$), the weakly rotational case $S = 4$ contains more energy in the region of the high-frequency wave compared to the other cases. At location D, we observe the nonlinear f_{w2} and $f_{w,4}$ for the $S = 4, \infty$, while these waves are absent for the rotational case $S = 1$.

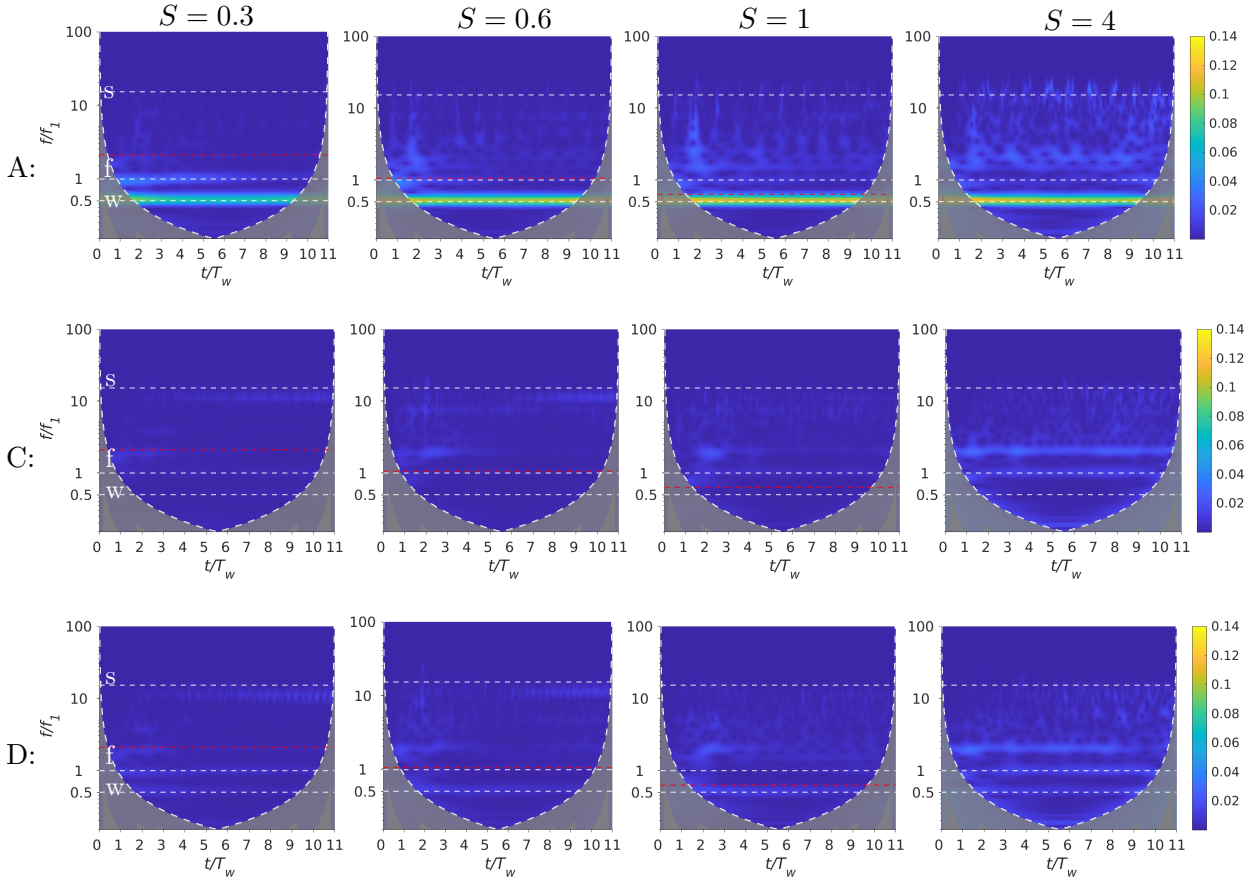

Figure 3.21: Wavelets of interface height sampled at locations A, C, and D shown in rows for $r_T = 2$ and S denoted in the figure. The colorbar represent absolute values of the continuous wavelet transform. Line – – – represents inertial frequency f_i, while dashed white horizontal lines denoted with letters indicate: w, forcing frequency f_w ; f, fundamental frequency f_1 ; s, approximate frequency of solitary-like waves $\approx f_s$. All frequencies are nondimensionalized with the forcing frequency f_1.

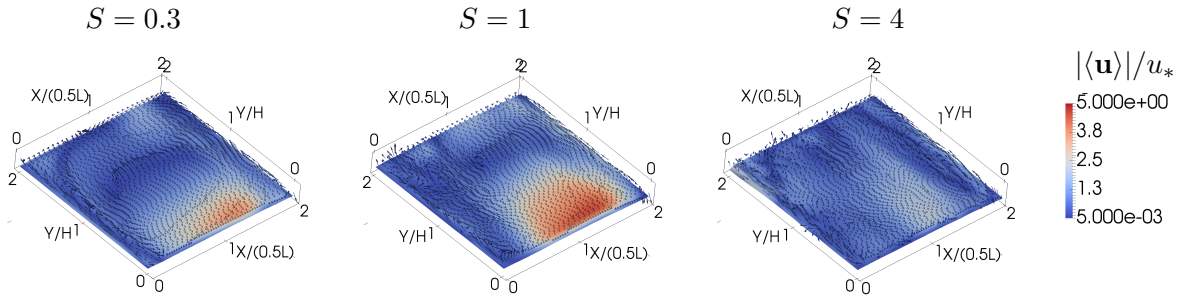

Figure 3.22: The nondimensional phase-averaged velocity magnitude at $\varphi = 30°$ shown at the isopycnal surface ρ_0.

In figure 3.22 we show the nondimensional phase-averaged velocity magnitude at the density surface ρ_0. We note that velocity maximum is located near the boundary and decreases away from it with the rate of decrease increasing as rotation intensifies, corresponding to the Behavior of Kelvin waves. We note that this structure is visible even for the weakly rotational case $S = 4$ where forcing is strongly superinertial. In this case, we do not observe the degeneration of Kelvin wave with the high-frequency waves and we find that behavior in all cases belongs to the nonlinear regime as defined by Ulloa et al. (2015).

In order to understand the vertical structure of the detected waves, we inspect vertical profiles of the velocity as shown in figure 3.23.

At the near-wall location A, streamwise velocity $\langle u \rangle$ profiles display complex layered behavior, while spanwise velocity has typical V1 behavior for all rotational cases. This indicates the development of the Kelvin wave that propagates parallel with the side-wall. Nonintuitively, the magnitude of $\langle v \rangle$ increases with the weakening of the rotation (an increase of S), with the exception of the nonrotational case $S = \infty$. This is consistent with the weakest signal of forced Kelvin wave found at location A for the strongest rotation ($S = 0.3$) in rotary spectra. Vertical velocity $\langle w \rangle$ profiles mostly display V2 structure.

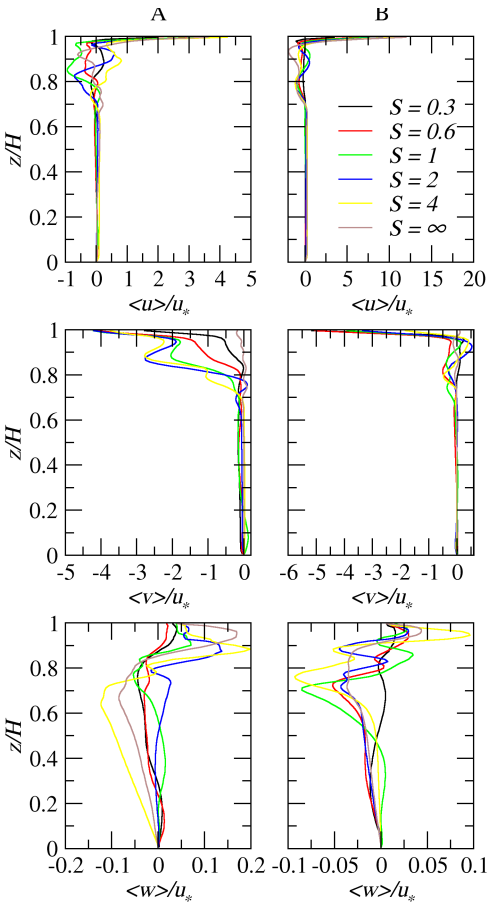

Figure 3.23: Vertical profiles of the phase averaged velocity components sampled at locations A and B at the forcing phase $\varphi = 120°$. Phase φ corresponds to phase of the the forcing period.

At the internal location B, $\langle u \rangle$ profiles, display V2 structure for most of the cases, where V4 structure characterize $S = 1, 2$ profiles. Profiles of $\langle v \rangle$ for rotating cases have structure from V1 to V3 while nonrotating case shows V4 structure. The profiles of vertical velocity component vary in structure from V2 to V5.

The slices of turbulence dissipation rate and turbulent diffusivity of density are shown in figure 3.24. The dissipation in hypolimnion increases with the increase of rotation rate, while the upper layers show the opposite behavior. A high amount of dissipation that is present in the region of the return jet is substantially reduced as the rate of rotation increases.

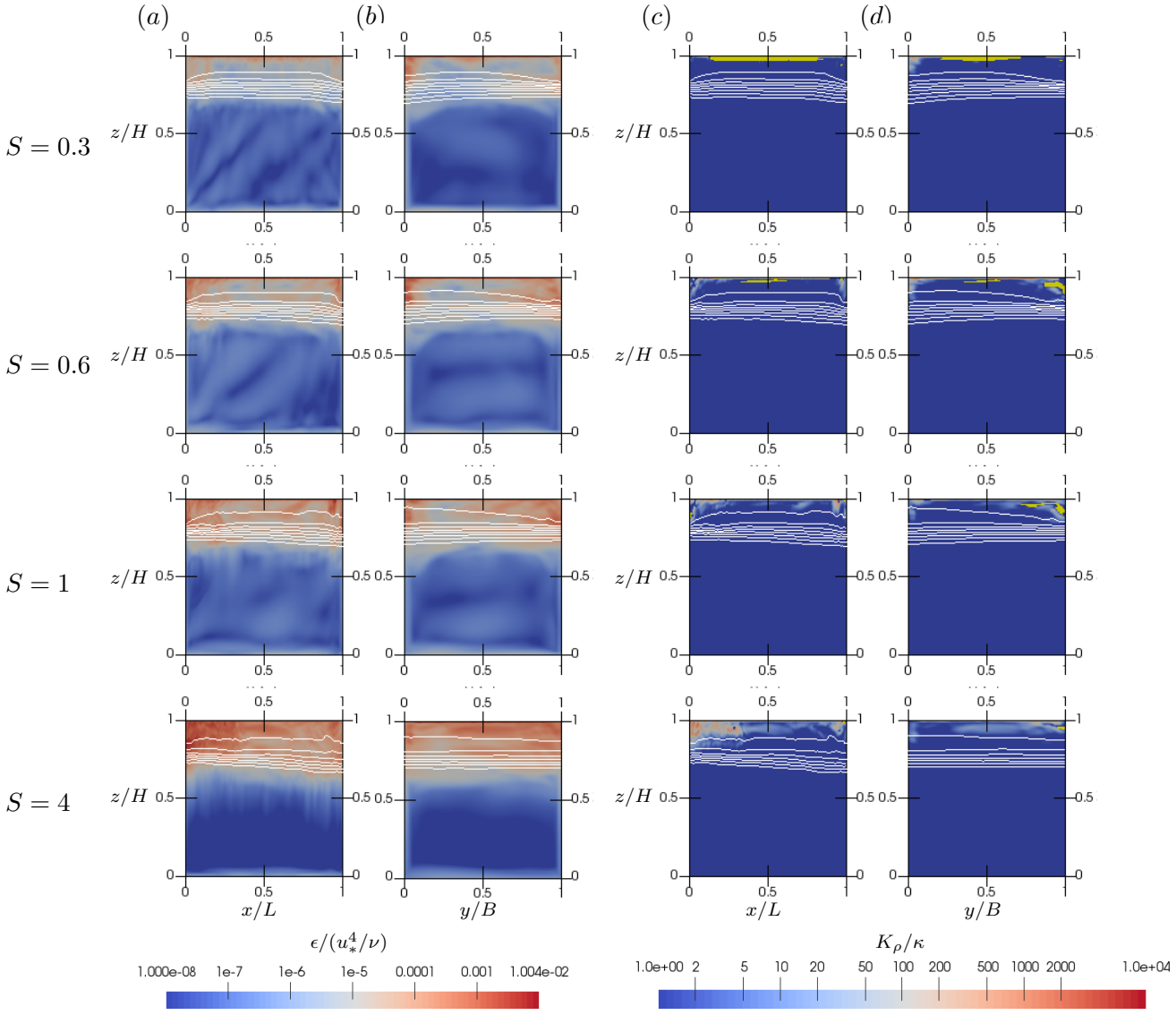

Figure 3.24: Slices in $x - z$ (a, c) and $y - z$ (b, d) planes through turbulence fields for $r_T = 2$ at the forcing phase $\varphi = 30°$: (a, b), nondimensional dissipation rate; (c, d) nondimensional turbulent diffusivity of density. White lines indicate isopycnals while the yellow color represents the regions with unstable stratification, where $\langle N^2 \rangle$ is negative.

In figure 3.24(c, d) the slices through parameterized K_ρ show that the amount of the near-wall mixing decreases with S, while near-surface overturns increase. For low S, mixing and overturns are present also at the lateral walls. By observing the isopycnals for $S > 1$, along the length of the basin, we observe a second vertical mode response with contracted isopycnals at one end and isopycnals spread at the opposite end, while for lower S isopycnals at both ends seem contracted and spread is found in the middle of the

basin. In the $y-z$ plane (figure 3.24(d)) we observe that isopycnals form a V2 response (contracted and spreaded isopycnals) for all rotational cases.

In figure 3.25 we plot global quantities for turbulence and mixing. The global dissipation rate increases as the rotation intensify while rotation is weak with respect to Burger number ($S > 2$). For low Burger numbers dissipation decrease with a decrease of S. Mixing shows different behavior and decreases as rotation gets stronger (S decreases). The change in mixing is more pronounced for smaller Burger numbers ($S \leq 2$), which correspond to the cases where forcing frequency is smaller than or close to the inertial one. The vertical variation of mixing is described through the relative difference of the final and initial density profile. Overall, the nonrotational case is the most mixed one, and the amount of mixing decreases with a decrease of S. The cases with strong rotation ($S \leq 2$) get mixed mostly in the upper metalimnion, while for $S > 2$ the most of the mixing is located near the surface and lower end of metalimnion, leading to metalimnion deepening as we observed in the time series in figure 3.19.

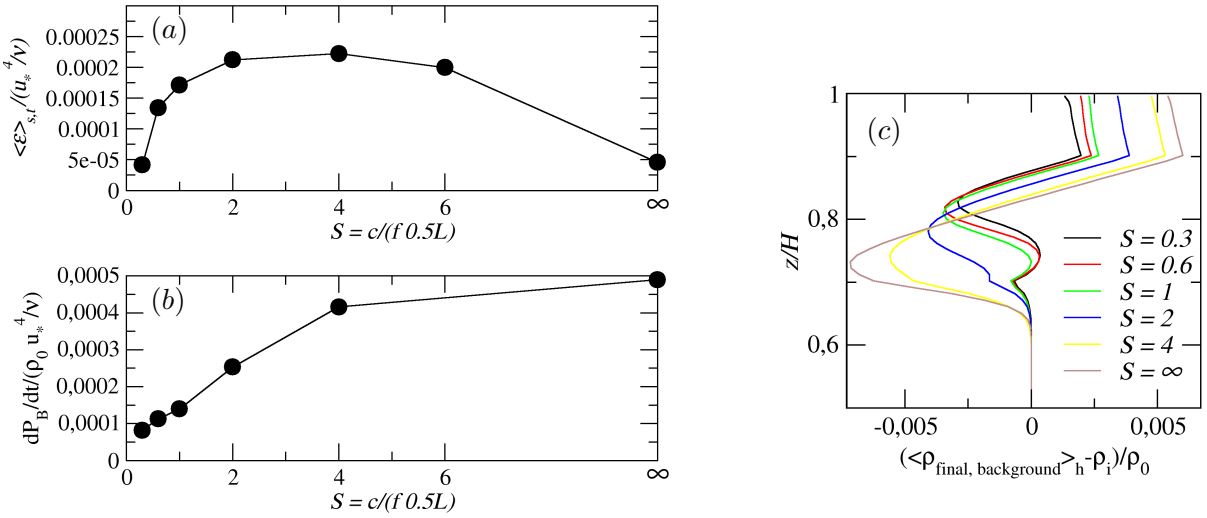

Figure 3.25: Averaged quantities as global indicators of turbulence and mixing for the $r_T = 2$: (a), spatially and temporally averaged nondimensional dissipation rate with respect to Burger number; (b), the total change in the background potential energy; (c), the difference of the background final horizontally averaged density profile compared to the initial one.

Summary: A periodically forced stratified system, whose fundamental period is half of the forcing one will develop the wave response with forcing frequency whose vertical modal structure depends on the rotational effects. When forcing frequency is superinertial, forced wave response is in terms of V1 Kelvin wave in the near-boundary region, while for the subinertial forcing frequency weakly anticyclonic Poincaré wave response with V2 structure develops. The overall dissipation increases with the increase of Burger number if the forcing frequency is superinertial. For subinertial forcing frequencies, the most energetic Poincaré waves are inhibited and overall dissipation decreases. Mixing decreases as rotation intensifies, due to the weakening of the return jet and internal mixing by Poincaré waves (because of the relation among inertial and forcing frequency).

3.5 Concluding remarks

In the present Chapter, we investigated the wave response of a periodically forced stratified basin under the influence of rotation. The wave response was discussed with respect to modal structure and type of internal waves and mixing.

We carried out a numerical investigation, using Large Eddy Simulation, at a laboratory scale. The model without the rotation was validated against two different laboratory experiments, while the effects of rotation were validated against the analytical solution for the Ekman spiral. We set a three-layer stratification, typical of real-scale basins, and studied the system under variation of the forcing frequency (the frequency of the forcing wind stress) and variation of the rate of rotation expressed through Burger number. We obtained different basin responses, classified in table 3.5 according to wave modes and occurrence of resonance. We identified that the ratio between forcing and inertial period plays an important role in the determination of the type of wave response, therefore we introduce a new parameter $r_I = T_i/T_w$ as a ratio of inertial and forcing periods. The case of $r_I > 1$ corresponds to the case when $f_w > f_i$ thus forcing frequency is superinertial and Poincaré waves are favored, while $r_I < 1$ corresponds to $f_w < f_i$ thus forcing frequency is subinertial which favors Kevin waves.

Forcing with $r_T = 0.5$: A weak but complex wave response appears with superimposed multiple horizontal and vertical modes. For nonrotational and weakly rotational cases fundamental V1H1 wave and forced wave VnHm appear with similar energy content. We do not identify the unique modal structure of the forced wave over cases with a different rotation, but our inspection of the fields indicates that it generally appears as higher horizontal mode and, for superinertial forcing, as higher vertical mode. As rotation intensifies, the fundamental wave transforms to a weakly cyclonic Kelvin wave and its amplitude decreases, while the forced wave (that is generally superinertial) transforms to anticyclonic Poincaré wave. We also observe complex behavior such as triad interactions. We note that wave response is less stable in the rotational cases, where waves lose their energy and re-energize often while transferring their energy to the high-frequency waves.

r_T	Main response	r_I
0.5	(f_1 V1H1+), (f_w V1Hm-)	$\lessapprox 1$
0.5	(f_1 V1H1+), (f_w VnHm-)	> 1
1	resonant (f_1 V1H1+)	$\lessapprox 1$
1	resonant (f_1 V1H1-)	> 1
2	(f_w V1H1+)	$\lessapprox 1$
2	(f_w V2H1)	> 1

Table 3.5: Frequency and modal structure of the dominant response with respect to r_T and r_I. Symbols + and - denote cyclonic and anticyclonic rotational characteristics of the wave respectively.

Forcing with $r_T = 1$: The resonant response develops as Kelvin wave when forcing frequency is subinertial or as weakly anticyclonic Poincaré wave when forcing frequency is superinertial. In each case, superinertial superharmonics appear as Poincaré waves. The decrease of Burger number pushes the degeneration of the Kelvin wave from nonlinear to the nonlinear and non hydrostatic regime, as defined by Ulloa et al. (2015).

Forcing with $r_T = 2$: A wave response with the frequency of forcing develops as Kelvin wave when forcing frequency is subinertial and nonrotational for superinertial forcing frequencies. We note that the Burger number is high in the tested cases with superinertial forcing frequencies. The development of Kelvin wave response pushes the dominant dynamics to the first vertical mode behavior, compared to V2 behavior in nonrotational and weakly rotational cases.

The rotational effects also influence the amount and distribution of mixing and dissipation in the basin. Dissipation rate has a general tendency to increase as rotation strengthens for $r_I > 1$ (superinertial forcing frequency), while for $r_I < 1$ it decreases as rotation rate increases. The first is the effect of increased dissipation due to the development of Poincaré waves as described by Bouffard et al. (2012) and the second of development of Kelvin waves that adjust to forcing in the near-boundary region and decrease the turbulent boundary effects. The effects of mixing are somewhat different partially due to the fact that we are using laboratory scales with layers with constant density and transitional layer where Richardson number is substantially higher than in real scales, thus reducing mixing. We note that near-surface mixing decreases in rotational cases, due to shallower penetration of the return jet. The decrease of boundary effects with a strengthening of rotation can be observed also in decreased phase lag in the near-boundary sampling location.

Chapter 4

Conclusion

In this thesis, we investigated the response of the stratified basin to the periodic forcing, in terms of the internal waves, turbulence and mixing and their interconnection. We used three-dimensional numerical simulations set on laboratory scales, such that main nondimensional parameters correspond to the conditions in weakly or moderately forced, summer stratified mid-sized lakes.

In the first part of our research (chapter 2) we considered the system without rotation, with variable inclination of the end-walls and forcing period. We found that for forcing frequency that is close to the natural frequencies of the system (associated with system's geometry and stratification) the wave response develops with the frequency of forcing and with the modal structure of the closest natural mode as a stable wave response whose energy does not vary considerably with time. On the other hand, when the frequency of forcing is far from the system's natural frequencies, it becomes unstable and a fundamental wave (with first horizontal and first vertical mode) occurs and disperses multiple times. We observe that such an unstable state is suitable for the development of the strongly nonlinear wave response.

Regarding the influence of the sloped walls on the wave field, we find that the influence of mixing on the sloped walls can change the background density field, thus leading the system further or closer to the resonant state.

In the second part of our research (chapter 3) I consider the system under the influence of rotation. The ratio of forcing frequency to the inertial frequency of rotation plays an important role in the excitation of different wave types (Kelvin or Poincaré waves) which has direct implications on both horizontal and vertical modal structure of the dominant wave response. We note that the amount of dissipation rate increases with the rate of rotation for superinertial forcing frequencies, which is related to the excitation of Poincaré waves. Mixing is not following the same trend, partially because the increase of the rate of rotation decreases the amount of near-boundary mixing imposed directly by forcing, and partially due to the laboratory scales with significantly stronger stratification that inhibits vertical mixing compared to real scales.

The generalization of our results has significant implications for lakes subject to diurnal wind forcing. The size of the lake imposes the vertical modal structure of the dominant wave response, where smaller favor the occurrence of higher vertical mode waves due to their short fundamental periods compared to diurnal ones. The angle of the sloped boundaries of the lake regulates the main location of mixing near the boundary, where for gentle slopes, mixing is excited by internal waves and located at the height of metalimnion. For steep slopes, vigorous mixing in the near-surface layer and in the upper metalimnion is excited directly by the forced surface flow. The effects of Earth's rotation on the basin response

strongly depend on the size of the lake and its latitude. For lakes above 30° latitude diurnal forcing has superinertial frequency, which favors the excitement of Poincaré type waves and increases the amount of turbulent dissipation and mixing in the metalimnion.

We note that, due to laboratory scales of our simulations, we cannot give an estimate on the time scales of mixing processes and feedbacks to wave field for real scales, which is something that should be further investigated in the future. We further note that the stratification setup in the numerical experiments considers hypolimnion with uniform density, while in nature, this layer is always weakly stratified. A stratified hypolimnion allows the development of shear-induced mixing and internal waves, which we do not consider in our simulations. In the rotational cases, the shape of the domain plays an important role in the development and modal structure of the internal waves, which we do not investigate in our present work, which might be of interest for future investigations.

Outlook: The work presented in this thesis can be further extended by describing the time scales needed for periodic forcing to mix the density field enough to change the wave response in terms of parameters that can be extended to real scales. The effects that may arise from weakly stratified hypolimnion can be further explored. Regarding the cases with rotation, the influence of the domain shape on the modal structure of internal waves, turbulence and mixing should be further explored.

Acknowledgments

We acknowledge the CINECA award under the ISCRA initiative, for the availability of high performance computing resources and support. The simulations were carried out under the IsC69_TICB and IsC80_IWRF projects.

Bibliography

Aghsaee, P., Boegman, L., and Lamb, K. G. (2010). Breaking of shoaling internal solitary waves. Journal of Fluid Mechanics, 659:289–317.

Antenucci, J. (2009). Currents in stratified water bodies 3: Effects of rotation. In Likens, G. E., editor, Encyclopedia of Inland Waters, pages 559–567. Academic Press, Oxford.

Antenucci, J. P. and Imberger, J. (2001). Energetics of long internal gravity waves in large lakes. Limnology and Oceanography, 46(7):1760–1773.

Antenucci, J. P. and Imberger, J. (2003). The seasonal evolution of wind/internal wave resonance in Lake Kinneret. Limnology and Oceanography, 48(5):2055–2061.

Antenucci, J. P., Imberger, J., and Saggio, A. (2000). Seasonal evolution of the basin-scale internal wave field in a large stratified lake. Limnology and Oceanography, 45(7):1621–1638.

Arthur, R. S. and Fringer, O. B. (2014). The dynamics of breaking internal solitary waves on slopes. Journal of Fluid Mechanics, 761:360–398.

Arthur, R. S. and Fringer, O. B. (2016). Transport by breaking internal gravity waves on slopes. Journal of Fluid Mechanics, 789:93–126.

Aucan, J., Merrifield, M. A., Luther, D. S., and Flament, P. (2006). Tidal mixing events on the deep flanks of Kaena Ridge, Hawaii. Journal of Physical Oceanography, 36(6):1202–1219.

Boegman, L. (2009). Currents in stratified water bodies 2: Internal waves. In Likens, G. E., editor, Encyclopedia of Inland Waters, pages 539–558. Academic Press, Oxford.

Boegman, L., Imberger, J., Ivey, G. N., and Antenucci, J. P. (2003). High-frequency internal waves in large stratified lakes. Limnology and Oceanography, 48(2):895–919.

Boegman, L., Ivey, G., and Imberger, J. (2005a). The degeneration of internal waves in lakes with sloping topography. Limnology and Oceanography, 50(5):1620–1637.

Boegman, L., Ivey, G., and Imberger, J. (2005b). The energetics of large-scale internal wave degeneration in lakes. Journal of Fluid Mechanics, 531:159–180.

Boegman, L. and Ivey, G. N. (2007). Experiments on internal wave resonance in periodically forced lakes. In 5th international symposium on environmental hydraulics, Tempe.

Boegman, L. and Ivey, G. N. (2009). Flow separation and resuspension beneath shoaling nonlinear internal waves. Journal of Geophysical Research: Oceans, 114(C2).

Boegman, L. and Ivey, G. N. (2012). The dynamics of internal wave resonance in periodically forced narrow basins. Journal of Geophysical Research: Oceans, 117(C11).

Bouffard, D. and Boegman, L. (2013). A diapycnal diffusivity model for stratified environmental flows. Dynamics of Atmospheres and Oceans, 61:14–34.

Bouffard, D., Boegman, L., and Rao, Y. R. (2012). Poincaré wave–induced mixing in a large lake. Limnology and Oceanography, 57(4):1201–1216.

Bouffard, D. and Wüest, A. (2018). Mixing in stratified lakes and reservoirs. In Mixing and dispersion in flows Dominated by Rotation and Buoyancy, pages 61–88. Springer.

Caulfield, C. (2021). Layering, instabilities, and mixing in turbulent stratified flows. Annual Review of Fluid Mechanics, 53(1):113–145.

Chen, G., Xiong, Q., Morris, P. J., Paterson, E. G., Sergeev, A., and Wang, Y. (2014). OpenFOAM for computational fluid dynamics. Notices of the AMS, 61(4):354–363.

Choi, J., Troy, C. D., Hsieh, T.-C., Hawley, N., and McCormick, M. J. (2012). A year of internal Poincaré waves in southern Lake Michigan. Journal of Geophysical Research: Oceans, 117(C7).

Cintolesi, C., Petronio, A., and Armenio, V. (2015). Large eddy simulation of turbulent buoyant flow in a confined cavity with conjugate heat transfer. Physics of Fluids, 27(9):095109.

Cooker, M., Weidman, P., and Bale, D. (1997). Reflection of a high-amplitude solitary wave at a vertical wall. Journal of Fluid Mechanics, 342:141–158.

Crank, J. and Nicolson, P. (1947). A practical method for numerical evaluation of solutions of partial differential equations of the heat-conduction type. In Mathematical Proceedings of the Cambridge Philosophical Society, volume 43, pages 50–67. Cambridge University Press.

Csanady, G. (1967). Large-scale motion in the Great Lakes. Journal of Geophysical Research, 72(16):4151–4162.

Csanady, G. (1982). On the structure of transient upwelling events. Journal of Physical Oceanography, 12(1):84–96.

de la Fuente, A., Shimizu, K., Imberger, J., and Nino, Y. (2008). The evolution of internal waves in a rotating, stratified, circular basin and the influence of weakly nonlinear and nonhydrostatic accelerations. Limnology and Oceanography, 53(6):2738–2748.

de la Fuente, A., Shimizu, K., Niño, Y., and Imberger, J. (2010). Nonlinear and weakly nonhydrostatic inviscid evolution of internal gravitational basin-scale waves in a large, deep lake: Lake Constance. Journal of Geophysical Research: Oceans, 115(C12).

Early, J. J., Lelong, M. P., and Smith, K. S. (2020). Fast and accurate computation of vertical modes. Journal of Advances in Modeling Earth Systems, 12(2):e2019MS001939.

Farmer, D. M. (1978). Observations of long nonlinear internal waves in a lake. Journal of Physical Oceanography, 8(1):63–73.

Farrow, D. E. and Stevens, C. L. (2003). Numerical modelling of a surface-stress driven density-stratified fluid. Journal of Engineering Mathematics, 47(1):1–16.

Fricker, P. D. and Nepf, H. M. (2000). Bathymetry, stratification, and internal seiche structure. Journal of Geophysical Research: Oceans, 105(C6):14237–14251.

Garrett, C. and Kunze, E. (2007). Internal tide generation in the deep ocean. Annu. Rev. Fluid Mech., 39:57–87.

Gayen, B. and Sarkar, S. (2010). Turbulence during the generation of internal tide on a critical slope. Physical Review Letters, 104(21):218502.

Gayen, B. and Sarkar, S. (2011). Direct and large-eddy simulations of internal tide generation at a near-critical slope. Journal of Fluid Mechanics, 681:48.

Gerkema, T. and Zimmerman, J. (1995). Generation of nonlinear internal tides and solitary waves. Journal of Physical Oceanography, 25(6):1081–1094.

Gill, A. E. (1982). Atmosphere. Ocean dynamics, 30:662.

Gómez-Giraldo, A., Imberger, J., and Antenucci, J. P. (2006). Spatial structure of the dominant basin-scale internal waves in Lake Kinneret. Limnology and Oceanography, 51(1):229–246.

Goudsmit, G.-H., Burchard, H., Peeters, F., and Wüest, A. (2002). Application of $k-\epsilon$ turbulence models to enclosed basins: The role of internal seiches. Journal of Geophysical Research: Oceans, 107(C12):23–1–23–13.

Greenspan, H. and Howard, L. (1963). On a time-dependent motion of a rotating fluid. Journal of Fluid Mechanics, 17(3):385–404.

Grimshaw, R., Pelinovsky, E., Talipova, T., and Kurkina, O. (2010). Internal solitary waves: propagation, deformation and disintegration. Nonlinear Processes in Geophysics, 17(6):633–649.

Grimshaw, R. H., Ostrovsky, L., Shrira, V., and Stepanyants, Y. A. (1998). Long nonlinear surface and internal gravity waves in a rotating ocean. Surveys in Geophysics, 19(4):289–338.

Helfrich, K. R. (1992). Internal solitary wave breaking and run-up on a uniform slope. Journal of Fluid Mechanics, 243:133–154.

Helfrich, K. R. (2007). Decay and return of internal solitary waves with rotation. Physics of Fluids, 19(2):026601.

Horn, D., Imberger, J., and Ivey, G. (2001). The degeneration of large-scale interfacial gravity waves in lakes. Journal of Fluid Mechanics, 434:181–207.

Horn, W., Mortimer, C. H., and Schwab, D. J. (1986). Wind-induced internal seiches in Lake Zurich observed and modeled 1. Limnology and Oceanography, 31(6):1232–1254.

Imberger, J. and Hamblin, P. F. (1982). Dynamics of lakes, reservoirs, and cooling ponds. Annual Review of Fluid Mechanics, 14(1):153–187.

Issa, R. I., Gosman, A., and Watkins, A. (1986). The computation of compressible and incompressible recirculating flows by a non-iterative implicit scheme. Journal of Computational Physics, 62(1):66–82.

Jasak, H. (1996). Error analysis and estimation for the finite volume method with applications to fluid flows.

Koop, C. G. and Butler, G. (1981). An investigation of internal solitary waves in a two-fluid system. Journal of Fluid Mechanics, 112:225–251.

La Rocca, M., Sciortino, G., Adduce, C., and Boniforti, M. (2005). Experimental and theoretical investigation on the sloshing of a two-liquid system with free surface. Physics of Fluids, 17(6):062101.

Lamb, H. (1932). Hydrodynamics. 6th Edition. Cambridge University Press.

LaZerte, B. D. (1980). The dominating higher order vertical modes of the internal seiche in a small lake. Limnology and Oceanography, 25(5):846–854.

Lewis, W. (2009). Ecological zonation in lakes. In Likens, G. E., editor, Encyclopedia of Inland Waters, pages 416–422. Academic Press, Oxford.

Lienhard, J. H. and Atta, V. (1990). The decay of turbulence in thermally stratified flow. Journal of Fluid Mechanics, 210:57–112.

Likens, G. E. (2010). Lake ecosystem ecology: A global perspective. Academic Press.

Linden, P. and Van Heijst, G. (1984). Two-layer spin-up and frontogenesis. Journal of Fluid Mechanics, 143:69–94.

Linden, P. F. (2018). Turbulence and mixing in flows dominated by buoyancy. In Mixing and Dispersion in Flows Dominated by Rotation and Buoyancy, pages 25–60. Springer.

Liu, F. (2016). A thorough description of how wall functions are implemented in openfoam. Proceedings of CFD with OpenSource Software, pages 1–33.

Liu, H.-T. (1995). Energetics of grid turbulence in a stably stratified fluid. Journal of Fluid Mechanics, 296:127–157.

Lorke, A. (2007). Boundary mixing in the thermocline of a large lake. Journal of Geophysical Research: Oceans, 112(C9).

Lorke, A., Peeters, F., and Wüest, A. (2005). Shear-induced convective mixing in bottom boundary layers on slopes. Limnology and Oceanography, 50(5):1612–1619.

Lorke, A., Umlauf, L., Jonas, T., and Wüest, A. (2002). Dynamics of turbulence in low-speed oscillating bottom-boundary layers of stratified basins. Environmental Fluid Mechanics, 2(4):291–313.

MacIntyre, S., Clark, J. F., Jellison, R., and Fram, J. P. (2009). Turbulent mixing induced by nonlinear internal waves in Mono Lake, California. Limnology and Oceanography, 54(6):2255–2272.

MacIntyre, S., Flynn, K. M., Jellison, R., and Romero, J. R. (1999). Boundary mixing and nutrient fluxes in Mono Lake, California. Limnology and Oceanography, 44(3):512–529.

Magni, D., Chinaglia, N., Maffotti, A., Borasi, L., Lefebvre, P., Zanella, D., Brancelj, A., Mori, N., Pagon, P., and Urbanc-Berčič, O. (2008). Alpine Lakes: A Common Approach to the Characterization of Lakes and Their Catchmet Area.

Marković, S. and Armenio, V. (2021). Laboratory-scale investigation of a periodically forced stratified basin with inclined end-walls.

Meneveau, C., Lund, T. S., and Cabot, W. H. (1996). A lagrangian dynamic subgrid-scale model of turbulence. Journal of Fluid Mechanics, 319:353–385.

Michallet, H. and Ivey, G. (1999). Experiments on mixing due to internal solitary waves breaking on uniform slopes. Journal of Geophysical Research: Oceans, 104(C6):13467–13477.

Monismith, S. (1986). An experimental study of the upwelling response of stratified reservoirs to surface shear stress. Journal of Fluid Mechanics, 171:407–439.

Monismith, S. (1987). Modal response of reservoirs to wind stress. Journal of Hydraulic Engineering, 113(10):1290–1304.

Monismith, S. G. (1985). Wind-forced motions in stratified lakes and their effect on mixed-layer shear. Limnology and Oceanography, 30(4):771–783.

Mortimer, C. (1953). The resonant response of stratified lakes to wind. Aquatic Sciences, 15(1):94–151.

Münnich, M. (1996). The influence of bottom topography on internal seiches in stratified media. Dynamics of Atmospheres and Oceans, 23(1-4):257–266.

Münnich, M., Wüest, A., and Imboden, D. M. (1992). Observations of the second vertical mode of the internal seiche in an alpine lake. Limnology and Oceanography, 37(8):1705–1719.

Nakayama, K., Sato, T., Shimizu, K., and Boegman, L. (2019). Classification of internal solitary wave breaking over a slope. Physical Review Fluids, 4(1):014801.

Osborn, T. R. and Cox, C. S. (1972). Oceanic fine structure. Geophysical & Astrophysical Fluid Dynamics, 3(1):321–345.

Pedlosky, J. et al. (1987). Geophysical Fluid Dynamics. Springer-Verlag New York Inc.

Peltier, W. and Caulfield, C. (2003). Mixing efficiency in stratified shear flows. Annual review of fluid mechanics, 35(1):135–167.

Rao, D. (1977). Free internal oscillations in a narrow, rotating rectangular basin. Mar. Sci. Directorate, Dept. Fish. Environ, pages 391–398.

Rao, D. B. (1966). Free gravitational oscillations in rotating rectangular basins. Journal of Fluid Mechanics, 25(3):523–555.

Rao, D. B., Schwab, D. J., and Mortimer, C. (1976). Surface normal modes of Lake Michigan: Calculations compared with spectra of observed water level fluctuations. Journal of Physical Oceanography, 6(4):575–588.

Robertson, E., Choudhury, V., Bhushan, S., and Walters, D. K. (2015). Validation of OpenFOAM numerical methods and turbulence models for incompressible bluff body flows. Computers & Fluids, 123:122–145.

Roget, E., Salvadé, G., and Zamboni, F. (1997). Internal seiche climatology in a small lake where transversal and second vertical modes are usually observed. Limnology and Oceanography, 42(4):663–673.

Rojas, P., Ulloa, H. N., and Niño, Y. (2018). Evolution and decay of gravity wavefields in weak-rotating environments: a laboratory study. Environmental Fluid Mechanics, 18(6):1509–1531.

Rozas, C., de la Fuente, A., Ulloa, H., Davies, P., and Niño, Y. (2014). Quantifying the effect of wind on internal wave resonance in Lake Villarrica, Chile. Environmental Fluid Mechanics, 14(4):849–871.

Saggio, A. and Imberger, J. (2001). Mixing and turbulent fluxes in the metalimnion of a stratified lake. Limnology and Oceanography, 46(2):392–409.

Salon, S., Armenio, V., and Crise, A. (2007). A numerical investigation of the stokes boundary layer in the turbulent regime. Journal of Fluid Mechanics, 570:253–296.

Sarkar, S. and Scotti, A. (2017). From topographic internal gravity waves to turbulence. Annual Review of Fluid Mechanics, 49:195–220.

Sato, M., Klymak, J., Kunze, E., Dewey, R., and Dower, J. (2014). Turbulence and internal waves in patricia bay, saanich inlet, british columbia. Continental Shelf Research, 85:153–167.

Schwab, D. J. (1977). Internal free oscillations in Lake Ontario 1. Limnology and Oceanography, 22(4):700–708.

Shih, L. H., Koseff, J. R., Ivey, G. N., and Ferziger, J. H. (2005). Parameterization of turbulent fluxes and scales using homogeneous sheared stably stratified turbulence simulations. Journal of Fluid Mechanics, 525:193–214.

Shintani, T., de la Fuente, A., de la Fuente, A., Niño, Y., and Imberger, J. (2010). Generalizations of the Wedderburn number: Parameterizing upwelling in stratified lakes. Limnology and Oceanography, 55(3):1377–1389.

Smagorinsky, J. (1963). General circulation experiments with the primitive equations: I. The basic experiment. Monthly Weather Review, 91(3):99–164.

Spalart, P. R. (1997). Comments on the feasibility of LES for wings, and on a hybrid RANS/LES approach. In Proceedings of first AFOSR international conference on DNS/LES. Greyden Press.

Spigel, R. H. and Imberger, J. (1980). The classification of mixed-layer dynamics of lakes of small to medium size. Journal of Physical Oceanography, 10(7):1104–1121.

Stevens, C. and Imberger, J. (1996). The initial response of a stratified lake to a surface shear stress. Journal of Fluid Mechanics, 312:39–66.

Stocker, R. and Imberger, J. (2003). Energy partitioning and horizontal dispersion in a stratified rotating lake. Journal of Physical oceanography, 33(3):512–529.

Tang, C., Patel, V., and Landweber, L. (1990). Viscous effects on propagation and reflection of solitary waves in shallow channels. Journal of Computational Physics, 88(1):86–113.

Thompson, R. and Imberger, J. (1980). Response of a numerical model of a stratified lake to wind stress. In Proc. Second Int. Symp. Stratified Flows, IAHR, 1980.

Thorpe, S. (1971). Asymmetry of the internal seiche in Loch Ness. Nature, 231(5301):306–308.

Thorpe, S. (1974). Near-resonant forcing in a shallow two-layer fluid: a model for the internal surge in Loch Ness? Journal of Fluid Mechanics, 63(3):509–527.

Thorpe, S. (1998). Some dynamical effects of internal waves and the sloping sides of lakes. Coastal and Estuarine Studies, pages 441–460.

Ulloa, H. N., Constantinescu, G., Chang, K., Horna-Munoz, D., Hames, O., and Wüest, A. (2020). Horizontal transport under wind-induced resonance in stratified waterbodies. Physical Review Fluids, 5(5):054503.

Ulloa, H. N., Constantinescu, G., Chang, K., Horna-Munoz, D., Steiner, O. S., Bouffard, D., and Wüest, A. (2019). Hydrodynamics of a periodically wind-forced small and narrow stratified basin: A large-eddy simulation experiment. Environmental Fluid Mechanics, 19(3):667–698.

Ulloa, H. N., de la Fuente, A., and Niño, Y. (2014). An experimental study of the free evolution of rotating, nonlinear internal gravity waves in a two-layer stratified fluid. Journal of Fluid Mechanics, 742:308.

Ulloa, H. N., Winters, K. B., de la Fuente, A., and Niño, Y. (2015). Degeneration of internal Kelvin waves in a continuous two-layer stratification. Journal of Fluid Mechanics, 777:68.

Valerio, G., Pilotti, M., Marti, C. L., and Imberger, J. r. (2012). The structure of basin-scale internal waves in a stratified lake in response to lake bathymetry and wind spatial and temporal distribution: Lake Iseo, Italy. Limnology and Oceanography, 57(3):772–786.

Valipour, R., Bouffard, D., Boegman, L., and Rao, Y. R. (2015). Near-inertial waves in Lake Erie. Limnology and Oceanography, 60(5):1522–1535.

van Heijst, G. J. F., Davies, P. A., and Davis, R. (1990). Spin-up in a rectangular container. Physics of Fluids A: Fluid Dynamics, 2(2):150–159.

Van Leer, B. (1974). Towards the ultimate conservative difference scheme. ii. monotonicity and conservation combined in a second-order scheme. Journal of Computational Physics, 14(4):361–370.

Vidal, J., Rueda, F. J., and Casamitjana, X. (2007). The seasonal evolution of high vertical-mode internal waves in a deep reservoir. Limnology and Oceanography, 52(6):2656–2667.

Villermaux, E. (2019). Mixing versus stirring. Annual Review of Fluid Mechanics, 51:245–273.

Vincent, W. (2009). Effects of climate change on lakes. In Likens, G. E., editor, Encyclopedia of Inland Waters, pages 55–60. Academic Press, Oxford.

Vlasenko, V. and Hutter, K. (2002). Transformation and disintegration of strongly nonlinear internal waves by topography in stratified lakes. In Annales Geophysicae, volume 20, pages 2087–2103. Copernicus GmbH.

Wain, D. J., Kohn, M. S., Scanlon, J. A., and Rehmann, C. R. (2013). Internal wave-driven transport of fluid away from the boundary of a lake. Limnology and Oceanography, 58(2):429–442.

Wain, D. J. and Rehmann, C. R. (2010). Transport by an intrusion generated by boundary mixing in a lake. Water Resources Research, 46(8).

Wake, G., Ivey, G., Imberger, J., and McDonald, N. (2005). The temporal evolution of a geostrophic flow in a rotating stratified basin. Dynamics of Atmospheres and Oceans, 39(3-4):189–210.

Wake, G. W., Hopfinger, E. J., and Ivey, G. N. (2007). Experimental study on resonantly forced interfacial waves in a stratified circular cylindrical basin. Journal of Fluid Mechanics, 582:203–222.

Wake, G. W., Ivey, G. N., Imberger, J., McDonald, N. R., and Stocker, R. (2004). Baroclinic geostrophic adjustment in a rotating circular basin. Journal of Fluid Mechanics, 515:63–86.

Weller, H. G., Tabor, G., Jasak, H., and Fureby, C. (1998). A tensorial approach to computational continuum mechanics using object-oriented techniques. Computers in Physics, 12(6):620–631.

Wiegand, R. C. and Chamberlain, V. (1987). Internal waves of the second vertical mode in a stratified lake. Limnology and Oceanography, 32(1):29–42.

Winters, K. B., Lombard, P. N., Riley, J. J., and D'Asaro, E. A. (1995). Available potential energy and mixing in density-stratified fluids. Journal of Fluid Mechanics, 289:115–128.

Wüest, A. and Lorke, A. (2003). Small-scale hydrodynamics in lakes. Annual Review of Fluid Mechanics, 35(1):373–412.